

Pore-Scale Modelling of Electrochemically Reactive Flow

Artem Lavrentev

Thesis Submitted in Fulfillment of the Requirement for
Master of Science

Department of Mechanical Engineering

Lakehead University

Supervised by Dr. Ali Tarokh

To My Family

Abstract

Electrochemistry, a field revolving around charge transport, is omnipresent in our every-day life. It is found in batteries, water treatment, medicine, and food processing, to name a few. Water dissolves more substances than any other liquid and is consequently easily polluted. Self-evidently, drinking water quality is crucial to our health. Water disinfection refers to any process that removes pathogens from drinking water. Electrochemical treatments are one of the processes used for water disinfection and are advantageous wherewith required chemicals are formed in situ, while needing less and in some cases no other additional chemicals. Porous electrodes are becoming increasingly prevalent in electrochemical systems due to enhanced features such as reaction kinetics and mass transport. The arising complexity of the electrochemical processes at the pore-scale, involving multicomponent reactive flow, poses numerous challenges to the currently available experimental methods and the macro-continuum mathematical models. This work is aimed at the development of pore-scale numerical model using the Lattice Boltzmann Method and focuses on anodic oxidation under the aqueous condition. Historically, iodine has been used as a disinfectant for wounds as well as water. Excess consumption however can have adverse health effects such as thyroid disease. Using potassium iodide for water disinfection allows for iodine to be produced via anodic oxidation and then consumed through cathodic reduction. The relationship between concentrations, flow rates and potentials are investigated in a flow-through porous electrode. Based on the dilute solution theory, with the assumption of excess supporting electrolyte and electroneutrality, the current is described by Ohm's law while migration is assumed to be negligible. Butler-Volmer kinetics are employed at the solid-liquid interface. The consumption of iodide and production of iodine are described via a reaction source/ sink added to the concentration

probability distribution function, respectively. The model is initially tested in one dimension and is shown to agree with the finite element results. It is then extended to two-dimensional porous geometry which is randomly generated following Gaussian distribution and separated into active and inactive nodes for interfacial reactions. The results showed that decreasing Re from 5 to 0.1 resulted in a 300% iodine production increase, while decreasing porosity from 0.9 to 0.7 yielded only 15% increase. The effects of decreasing porosity on iodine production may, however, be hindered by the structure of the solid matrix. The results indicate that the flow regime has a far greater effect than porosity changes in the $0.1 \leq Re \leq 5$ and $0.7 \leq \lambda \leq 0.9$ ranges.

Acknowledgement

I would like to thank my supervisor Dr. Ali Tarokh for his continuous guidance, insight, patience, and motivation throughout this work. His relentless pursuit of excellence has profoundly changed my approach to science, as well as to life.

I also would like to extend my gratitude to my thesis committee members, Dr. Wilson Wang and Dr. Siamak Elyasi, for their invaluable feedback on this work.

Lastly, I have to thank my family. Without their never-ending support and encouragement this work would not have been possible. They have given me an opportunity to explore and for that I am forever grateful.

Contents

Abstract	i
Acknowledgement	iii
Contents	iv
List of Figures	vii
List of Tables	x
Nomenclature	xi
1 Introduction	1
1.1 Motivation	1
1.2 Objective	7
1.3 Scope	8
1.4 Literature Review	9
2 Applicable Electrochemical Theory	11
2.1 Introduction	11
2.2 Kinetics and Thermodynamics	14
2.3 Transport	25
2.4 Current Distribution	27
2.5 Summary	28
3 Lattice Boltzmann Method Fundamentals	29
3.1 Introduction	29
3.2 Discretized Boltzmann Equation and the BGK Approximation	31

3.3	Lattice Structure	34
3.4	Collision and Streaming	36
3.5	Multi-Scale Expansion for Fluid Dynamics	38
3.6	Boundary Conditions (BC).....	41
3.6.1	No-slip Wall BC	42
3.6.2	Zero-Gradient BC	43
3.6.3	Velocity BC	43
3.6.4	Constant BC	45
3.6.5	Corner Nodes	46
4	Model Development.....	47
4.1	Introduction	47
4.2	Mathematical Model	48
4.3	Dimensional Analysis of the Continuity Equation.....	50
4.4	The Pseudo-Porous Model	55
4.5	The Physical Porous Geometry Model.....	57
4.6	Summary	61
5	Code Validation and Benchmark Solutions.....	62
5.1	Introduction	62
5.2	Heat Conduction in a Rectangular Plate	63
5.3	Fully Developed Flow, Advection in a Channel	67
5.4	Flow Around an Obstacle and Heat Transfer in a Channel.....	69
5.5	Advection and Diffusion in a Channel with Species Transport.....	74

5.6	Summary	75
6	Results and Discussion	76
6.1	Introduction	76
6.2	Pseudo-Porous Anode	79
6.3	Single Cell Reactor.....	85
6.4	Effect of Reynolds Number on Iodide/Iodine Concentration	90
6.5	Effect of Porosity on Iodide/Iodine Concentration	98
6.6	Summary	105
7	Conclusion and Future Work	106
7.1	Conclusion.....	106
7.2	Future Work	108
	References.....	109
	Appendix A.....	136

List of Figures

Figure 1: General Configuration of an Electrochemical Cell	13
Figure 2: Lattice Models: (a) $D1Q3$ (b) $D2Q9$	34
Figure 3: Collision Step	36
Figure 4: Streaming Step	36
Figure 5: Unknown Distribution Functions	42
Figure 6: Bounce-Back Method.....	42
Figure 7: Corner Treatment	46
Figure 8: Physical, Dimensionless and Lattice Scale Relationship	50
Figure 9: Porous Region (a) Total (b) Active-Red and Inactive-Cyan.....	58
Figure 10: Active Boundary Nodes Configuration.....	59
Figure 11: North Boundary Distribution Functions.....	60
Figure 12: Heat Conduction Fin Geometry Using $D2Q9$ lattice model, the temperature distribution can be determined as follows,	63
Figure 13: Constant Temperature Boundary.....	64
Figure 14: LBM Algorithm.....	65
Figure 15: Fin Dimensionless Temperature Contour.....	66
Figure 16: Fin Vertical Dimensionless Temperature Profile.....	66
Figure 17: Fully Developed Flow, Advection in a Channel	67
Figure 18: Radial Velocity Profile Along Different Sections of the Channel	68
Figure 19: Fully Developed Flow, Advection in a Channel LBM Results vs Analytical	68

Figure 20: Flow around Obstacle in a channel Domain	69
Figure 23: Flow Around an Obstacle in a Channel with Heat Transfer	69
Figure 21: Flow Around an Obstacle Velocity Magnitude Contour, $y/H=0.625$, a) $Re=50$, b) $Re=100$, c) $Re=150$,d) $Re=200$	71
Figure 22: Flow Around an Obstacle Velocity Magnitude Contour, $y/H=0.375$, a) $Re=50$, b) $Re=100$, c) $Re=150$,d) $Re=200$	71
Figure 24: Temperature Contour, $y/H=0.625$, a) $Re=50$, b) $Re=100$, c) $Re=150$,d) $Re=200$	72
Figure 25: Temperature Contour, $y/H=0.375$, a) $Re=50$, b) $Re=100$, c) $Re=150$,d) $Re=200$	73
Figure 26: Species Concentration Advection and Diffusion in a Channel	74
Figure 27: LBM Species Flux at the Bottom Surface vs Analytical Solution[104]	75
Figure 28: Phase Potential Distribution Results Imposed from the Pseudo_porous Model (a) Solid, (b) Electrolyte	78
Figure 29: Domain Schematic of a One-dimensional Porous Anode	79
Figure 30: Iodide Concentration LBM	81
Figure 31: Iodine Concentration LBM	81
Figure 32: Iodine Concentration LBM vs FEM (scaled)	82
Figure 33: Solid Potential LBM vs FEM	83
Figure 34: Electrolyte Potential LBM vs FEM	83
Figure 35: Pseudo Porous Anode Solid and Electrolyte Current Density LBM vs FEM	84
Figure 36: Schematic Representation of a Disinfection Cell with Flow-Through Porous Electrodes	85
Figure 37: Single Cell Reactor Iodide Concentration LBM vs FEM	87
Figure 38: Single Cell Reactor Iodine Concentration LBM vs FEM	88

Figure 39: Single Cell Reactor Solid Potential	89
Figure 40: Single Cell Reactor Electrolyte Potential	89
Figure 41: Physical Porous Structure in a Channel	90
Figure 42: Velocity Contours with Re= (a) 0.1, (b) 0.5, (c) 1, (d) 5	92
Figure 43 Average Velocity in the Porous Region with Varying Re	93
Figure 44: Iodide Concentration Contours with Re= (a) 0.1, (b) 0.5, (c) 1, (d) 5	94
Figure 45: Average Iodide Concentration in the Porous Region with Varying Re	95
Figure 46: Iodine Concentration Contour with Re= (a) 0.1, (b) 0.5, (c) 1, (d) 5	96
Figure 47: Average Iodine Concentration with Varying Re.....	97
Figure 48: Velocity Contours with Velocity Contours with (a) $\lambda=0.9$, (b) $\lambda=0.8$, (c) $\lambda=0.7$	98
Figure 49: Flow Streamlines with (a) $\lambda=0.9$, (b) $\lambda=0.8$, (c) $\lambda=0.7$	99
Figure 50: Average Velocity with Varying Porosity	100
Figure 51: Iodide Concentration Contours with (a) $\lambda=0.9$, (b) $\lambda=0.8$, (c) $\lambda=0.7$	101
Figure 52: Average Iodide Concentration with Varying Porosity	102
Figure 53: Iodine Concentration Contours with (a) $\lambda=0.9$, (b) $\lambda=0.8$, (c) $\lambda=0.7$	103
Figure 54: Average Iodine Concentration in the Porous Region with Varying Porosity	104

List of Tables

Table 1: Simulation Parameters for the Pseudo and Physical Models..... 80

Table 2: Physical Porous Geometry LBM Simulation Parameters with Varying Reynolds Numbers 91

Nomenclature

Symbol	Meaning (units)
a	Specific surface area of porous electrode ($\text{m}^2 \text{m}^{-3}$)
Bi	Biot number
C	Concentration (mol m^{-3})
c_i	Lattice speed
c_s	Lattice speed of sound
D	Diffusion coefficient ($\text{m}^2 \text{s}^{-1}$)
Da	Damkholer number
E	Energy (J)
E°	Equilibrium electrode potential under standard conditions vs. reference electrode (V)
E_{eq}	Equilibrium electrode potential vs. reference electrode (V)
F	Faraday constant (C mol^{-1})
G	Gravity (m s^{-2})
f, g, h	Equilibrium distribution function
H	Height
h	Thermal conductivity ($\text{W m}^{-2} \text{K}^{-1}$),
i	Current density (A m^{-2})
i_0	Exchange Current density of reactions (A m^{-2})
i_{lim}	Limiting Current density of reactions (A m^{-2})
i_n	Net Current Density (A m^{-2})
Kn	Knudsen number

Symbol	Meaning (units)
k_f	Forward Rate
k_b	Backward Rate
L	Length
m	Mass
mol	Amount of substance
n	Number of electrons
N	Flux of species ($\text{mol m}^{-2} \text{s}^{-1}$)
Pe	Peccelet number
Pr	Prandtl number
q	Internal heat source
R	Reaction rate ($\text{mol m}^{-3} \text{s}^{-1}$)
Re	Reynolds number
r	Universal gas constant ($\text{J mol}^{-1} \text{K}^{-1}$)
Sc	Schmidt number
s	Stoichiometric coefficient
s''	Force scaling factor
T	Temperature (K)
t	Time (s)
V_{cell}	Cell Voltage (V)
V_a	Anode feeder Voltage (V)
V_c	Cathode outlet Voltage (V)
v	Normal velocity (m s^{-1})
u	Linear electrolyte velocity (m s^{-1})
z_i	Charge on species

Symbol	Meaning (units)
α	Charge Transfer Coefficient
β	Symmetry Factor
Γ	Collision integral
γ	Deviatoric fluid stresses
ε	Smallness parameter
ζ	Thermal Diffusivity ($\text{m}^2 \text{s}^{-1}$)
η	Overpotential (V)
θ	Dimensionless temperature
ϑ	Error scale
κ	Convective coefficient ($\text{W m}^{-1} \text{K}^{-1}$),
λ	Porosity
μ	Mobility ($\text{m}^2 \text{V}^{-1} \text{s}^{-1}$)
ν	Kinematic viscosity ($\text{m}^2 \text{s}^{-1}$)
Π	Tensor
ρ	Density (kg m^{-3})
ζ	Tortuosity
σ_s	Solid phase conductivity (S m^{-1})
σ_L	Liquid phase conductivity (S m^{-1})
τ	Relaxation time
φ_s	Solid phase potential (V)
φ_L	Liquid phase potential (V)
Ω	Collision operator
ω	Collision frequency

Subscript	Meaning
<i>ave</i>	Average
<i>b</i>	Backward
<i>c</i>	Collision time
<i>eq</i>	Equilibrium
<i>eff</i>	Effective
<i>f</i>	Forward
<i>i</i>	<i>i</i> – th reacting species
<i>in</i>	Inlet
<i>LS</i>	Lattice scale
<i>max</i>	Maximum
<i>O</i>	Oxidized species
<i>PS</i>	Physical scale
<i>R</i>	Reduced species
<i>ref</i>	Reference

Superscript	Meaning
<i>b</i>	Bulk
°	Standard conditions
*	Arbitrary conditions

Chapter 1

Introduction

1.1 Motivation

Water and energy, in the present state of the world, are irrevocably intertwined. Their relationship can be viewed as analogous to symbiosis. Symbiotic relationships are classified into three categories: mutualism, commensalism, and parasitism. Mutualism, where both reap benefits from the relation to the other and commensalism, where one benefits and other is unaffected, are certainly the most attractive from the conservation, sustainability, and self-sufficiency point of view. To be labeled as either, the significant amount of water required to generate and use energy, would need to be returned to its original state, while energy required for water provision fully recovered or there was a way to generate electricity while treating water [1]. Unfortunately, because of natural constraints that arise and are associated with the phenomena pertaining to the use of energy and water resources, to the best of the authors knowledge, none of those are currently possible on the required scale. Thus, the only relationship classification that can be assigned is parasitic, where for one to benefit the other must be harmed or with water and energy association, depleted.

From a historical perspective the ubiquity of water in human existence is not a novel concept by any means, certainly a requirement for life. It has depended on for agriculture, transportation, hygiene and recreation since antiquity, however societal transformations due to advancements

such as the steam engine, science, mass production, and digital technology have radically changed our being. Over the past century water consumption has increased by a factor of 6 [2]. In 2015, per day, the U.S alone consumed 503 billion liters of water for thermoelectric power, 446 billion litres for irrigation and 147 billion litres for potable water, totalling 1218 billion litres [3]. By 2050 global water demand from manufacturing is projected to increase 400%, 140 % from thermal power generation and 130% from household use, for 55% increase [4] . Presently, 1.42 billion people live in areas with high or extremely high water vulnerability, 450 million of those are children. By 2030, 700 million people could be displaced because of extreme water scarcity[5].

Fresh water constitutes for ~3% of worlds water resources, of which only 0.3% is found in lakes and rivers while the rest is confined in the ice caps and underground aquifers, some are unreachable with the technologies or not economically viable [6]. The other 97% of water resides primarily in the oceans, containing salt it is unsuitable for many applications. Groundwater supplies have been reported to be diminished by a rate of extraction at 1-2% per year globally while an estimated 21 of the world's 37 largest aquifers identified as severely over-exploited [7] .

As the world continues to progress towards increased use of clean energy technologies, focusing on lowering anthropogenic emissions, its coincidence with decreased water demand is not explicit. Some energy technologies such as solar photovoltaics and wind do not require heat to make electricity and therefore have little to no water dependency while renewable energy sources, such as concentrated solar power and geothermal, use heat to drive a steam cycle require water for cooling. Depending on the cooling technology, water withdrawals and consumption can be equivalent to conventional power plants and in some instances doubled with integrating carbon capture and storage equipment [8]. Another example of progress, energy and water consumption is the ever increasing dependence on internet services, where the information communication

technology (ICT) sector is expected to grow from reported 18.4 to 29.3 billion devices by 2030 [9]. The millions of servers housed in massive data centres all require power and cooling where in some instances, 57% utilize potable water. The analysis of energy and water consumption of the ICT sector is still infant and uncertain; however, it highlights the importance of insight on the footprint of emerging technologies none the less.

All processes involved in water distribution, collection and treatment depend on energy. Seawater desalination and wastewater treatment are the most energy-intensive processes in the water sector. It was estimated that roughly 120 million tonnes of oil equivalent (Mtoe) of energy was used worldwide in the water sector in 2014. About 60% of that energy was consumed as electricity, corresponding to a global demand of 4% of total electricity consumption, which was equivalent to the total electricity consumption of Russia. Of the electricity consumed, the largest amount was used for the extraction of groundwater and surface water (around 40%), followed by wastewater treatment (including collection) with 25%. In developed countries, the largest share of water-related electricity consumption (42%) was used for wastewater treatment.

It was estimated that wastewater treatment consumes ~ 200 TWh or 1% of global energy consumption. Some of the factors influencing energy consumption are the treatment level, contamination level and energy efficiency of the process used. Insufficient treatment poses significant human and environmental health risks. Extensive treatment and increased water demand correspond to appreciable energy requirement.

Potable water treatment process typically involves the use of mechanical screens and sedimentation to remove effluents, followed by passage through filters to a storage tank where it gets disinfected after which it is pressurized. Some common disinfection techniques include, ozone, ultra-violet irradiation (UVI), chlorination and chloramination [10]. While a very effective

disinfectant, ozone breaks down rapidly and is unsuitable for distribution systems [11]. UVI is largely used with other processes as its main targets are bacteria and other pathogens [12]. Having gained popularity since the 1990's, studies on the effect of UVI on bacterial communities, however, remain scarce. UVI's advantage is in the absence of potentially harmful by-products, a common issue with chemical disinfection processes. Chlorination and its sibling chloramination, have been most widely used, but since the discovery that chlorine use can cause the formation of halogenated hydrocarbons identified a need for alternatives [13]. One of those alternatives are Advanced Oxidation Processes (AOPs) which in the most catholic sense, deal with oxidation methods involving aqueous solutions wherein the target pollutant is destroyed because of the intermediary production of highly reactive species that are indiscriminatory to their target [14][15]. The myriad of organics and inorganics that today's waste and filtration systems are exposed to requires targeted processes, involving various reactions. Some instances exist where the intermediary products remain after treatment and may be even more toxic than the initial compounds. A subset of AOP, Electrochemical Advanced Oxidation Processes (EAOPs), which can be broadly described as the local formation of oxidants by-way-of reduction/oxidation (redox) reactions at the electrode surface [16], is attractive in addressing that issue because it relies on electron transfer between the contaminant and the anode during oxidation, and similarly for heterogeneous radical production [17]–[21].

The major advantage is in lieu of the electron being a clean reagent. Other types of EAOP include photo-electrocatalysis, electro-Fenton, photoelectron-Fenton and sonoelectrolysis and can be applied to effluents with chemical oxygen demand (COD) between 0.1-100 g L⁻¹.

One of the strong oxidizing agents is periodate which is generated by iodate oxidation and can be regenerated back to iodate through reduction, during the water disinfection process [22][23].

Disinfectant concentration is of special interest since excess amounts of strong oxidizing agents such as iodine can cause considerable health risks such as thyroid disease [24]. Electrochemical disinfection with 0.1 to 1mM iodate has been reported to be very effective in *E.coli* removal [25] and the consumption risk associated with that concentration range addressed in [26]. Consequentially, a need for evaluation of concentrations in the ppm (10^{-6}) range is presented.

For the water disinfection process involving anodic oxidation and cathodic reduction, reactors using porous electrodes are preferred over conventional electrolytic reactors because of their high surface area. Larger surface area allows low current densities at the electrode/electrolyte interface, while maintaining high reaction rates compared to planar electrode reactors [27]. Depending on the flow structure, porous electrodes can be classified as: flow-by and flow-through [28]. The flow-through reactors, wherein the electrolyte flows directly through the pores, yield higher reaction rates, and are considered more advantageous. Another reactor distinction is its polarity [29]. Bipolar systems are characterized by the electric current and the cell voltage fed to the terminal electrodes on the opposite sides of the reactor. Meanwhile, monopolar reactors, have electrodes that are connected to the current rectifier in a parallel circuit.

The arising complexity of the electrochemical processes at the pore-scale, involving multicomponent reactive flow, poses many challenges to the currently available analytical methods. Because of the ‘black-box’ nature of flow-through porous electrodes, applied potential, electrical potential against a reference electrode, flow behaviour, electrode material requirement, chemical and electrochemical kinetics, pressure and compression variation effects are just some of the examples exhibiting experimental challenges. For instance, the reference electrode ideally needs to be as close as possible to the point of interest. However, its incorporation into a porous electrode is almost unfeasible since it would change the flow, amount of material used and

potentially total current, to name a few. Tracing dyes can be used for pore and throat flow investigation but require sensitive and consequently expensive technology. Computational modelling provides an alternative efficient tool for experimental shortcomings. Continuum based mathematical models using finite element and finite volume analysis are common approaches in numerical simulations but are unable to resolve the pore-scale dynamics. This limitation presents a need to develop a numerical model that can explore electrochemically reactive flow of a dilute solution, specifically aqueous potassium iodide, in a flow-through porous electrode at the pore-scale.

1.2 Objective

This work develops a model via the Lattice Boltzmann Method (LBM) with a focus on newly developed redox surface kinetics . The goal is to build a model capable of numerically investigating electrochemically reactive flow within porous media, the pseudo-porous and the physical structure. Pseudo-porous refers to the modelling of porous media by applying effective parameter corrections to account for porosity, as will be seen in Chapter 4. The model extension to include the porous structure is followed. The interfacial kinetics are consistent under both conditions and are based on the generic elementary surface reaction, as seen in equation 1, which can be used for any similar reactions. For this research iodide/iodine redox couple is used based on the previously mentioned need for electrochemical studies involving Iodine species in the ppm range.



One of the biggest challenges to modelling redox surface reactions is the absence of a dimensionless number suitable for the outlined problem. Damkohler number (Da), a dimensionless number relating reaction rate to transport rate, is unsuitable for this problem because of the spatial rate variation within flow-through porous electrodes. Thus, in-house dimensional analysis is required, seen in Chapter 4, to establish a relationship between the fluid dynamics and the electrochemical phenomena within porous media. Then use the derived relationship, to numerically study surface reactions. The developed model is to be used to study the electrochemical behaviour of a cell using the pseudo-porous condition and investigate the effect of Reynolds number and porosity on the concentrations of iodine and iodide with the mimicked physical geometry.

1.3 Scope

The structure of the following chapters is as follows,

- Chapter 2 provides basic principles of electrochemistry, specifically reaction kinetics, transport, and current relation.
- Chapter 3 overviews the Lattice Boltzmann Method.
- Chapter 4 outlines the method of this work and discusses model development
- Chapter 5 tests the developed code on several problems .
- Chapter 6 discusses the results
- Chapter 7 presents the conclusion and future work

1.4 Literature Review

Inherent to virtually every electrochemical reactor is the reaction kinetics and transport of charge and mass. However, the mechanisms describing operation varies depending on the application and phenomena considered. Inclusion of the electric double layer (EDL), existing in the nano range and microchannel flow introduce scale variations that exponentially increase computational cost of numerical solvers. Thus, scales and respective mechanisms are isolated with several assumptions. For instance, generally the EDL theory is assumed to have negligible effects on the macro description. One of the continuum approaches to modeling flow-through porous electrodes, involving dilute solutions, relies on the methodology developed by Newman [30], where a set of one-dimensional equations are used to describe the macroscopic behaviour of a single reaction because of the volumetric averaging within the porous electrode, of the surface and pore solution flux densities, the material balance is analogous to that of homogeneous chemical reactions. The Newman model has been employed with hydrodynamic considerations in redox flow batteries, investigating the relationship between mass transfer coefficients, flow field and electrolyte velocity [31]. Typically, variation of the reaction driving force, the electrode-electrolyte potential difference, arises due to the porous electrode ohmic losses along the electrode depth [32]. The positional force shift results in the non uniform reaction rate distribution. Despite the advantages arising from the large interior surface area of porous electrodes, properties such as the ohmic resistance of the electrolyte and mass transfer limitations can restrict the effectiveness of the reactor [33]. Other models have been developed, focusing on Tafel controlled kinetics and the effect of the geometric parameters on the reactor effectiveness [34], gas evolution and pore electrolyte resistivity [35], transport processes under limiting conditions [36][37][38] investigating metal ion removal from electrolytes and water streams , metal electrodeposition [39], and electrode

structural changes undergoing anodic dissolution because of electrochemical reaction [40] Experimental work has been aimed at utilization of porous anodes as reactive electrochemical membranes for water treatment [41], degradation of wastewater containing glyphosate [42] and iodine electrochemical oxidation in a non-porous reactor [43].

Chapter 2

Applicable Electrochemical Theory

Electrochemistry is a vast field enveloping an array of physical, chemical, and biological disciplines. Defining its bounds within modern science would be anecdotal, therefore only a brief of contextual highlights is provided

2.1 Introduction

The applicability of electrochemistry can be found in processes such as separations (electrodialysis for desalination), pollution control (metal recovery), corrosion (metal oxidation), electroanalytical chemistry (coulometry, potentiometry, voltammetry and mechanistic studies of redox reactions), electrosynthesis, energy storage and conversion. Electrosynthesis can be broadly generalized as utilization of electrical energy for electrochemical synthesis of chemical compounds in solution, such as radical ion formation through anodic and cathodic reactions leading to subsequent reactions and generating a required product. An example of such process is Electrochemical Advanced Oxidation Process (EAOP) used in water disinfection. Energy storage and conversion systems such as lithium-ion, vanadium redox flow batteries and fuel cells are just some of the recent electrochemical systems being used to meet the ever-increasing energy demand while embracing the critical need for clean technology. The outlined processes, although they certainly do not fall under the category of “one glove fits all”, are all based on the fundamental principles of electrochemistry which are outlined in a variety of texts [44]–[48]. The electrochemical theory

covered in this work deals only with case and process specific phenomena, thus several omissions are present such as the electric double layer theory (EDL). The reader may also refer to [49], for a condensed outline of electrochemical terminology.

At the core of electrochemistry lies the interface between an electronic conductor and ionic conductor where reduction-oxidation (redox) reaction occurs. The ionic conductor is responsible for transport of charge between the chemical species and the electronic conductor. Some texts refer to the interfacial reaction site as the electrode while others to the electronic conductor, implying the existence of the reaction site, the latter is used henceforth. The electrode is typically a metal or a semiconducting material where the charge carriers are electrons and electrode where oxidation occurs is referred to as the anode while reduction site cathode. However, this does not mean that interfacial sites are restricted to one type of redox, both oxidation and reduction can occur at the anode or cathode as will be seen in the next section. The anode is also designated as the more positive electrode. The ionic conductor, referred to as the electrolyte, can be a solution or solid state and the charge carriers are ions. In this work the electrolyte is assumed to be an aqueous solution. The movement of charge in the electrode and electrolyte is called current which is related to species concentration by Faraday's Law. Reactions that occur at the electrode are classified as heterogeneous and ones occurring in the bulk as homogeneous. The subsequent methodology formulation is based primarily on heterogeneous reactions; however, some cross contamination will be involved. The dilute solution theory is employed for the electrochemical phenomena within the electrolyte. Figure 1 exemplifies a generic system that the following discussion will be referenced to.

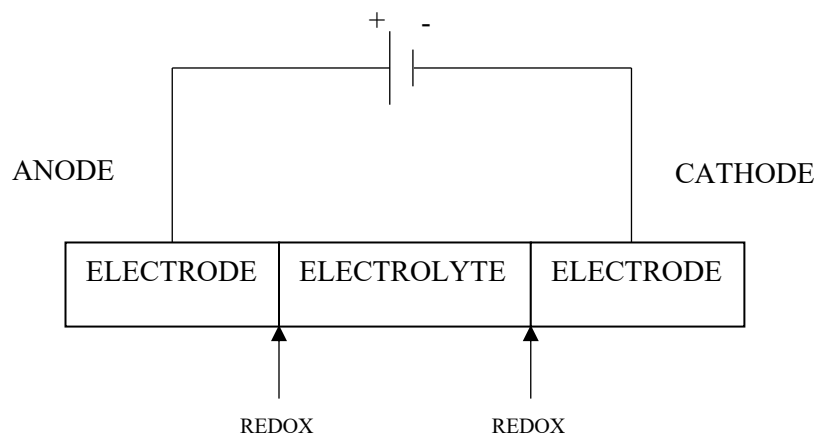


Figure 1: General Configuration of an Electrochemical Cell

2.2 Kinetics and Thermodynamics

The kinetics of a one-step, unimolecular, one-electron process refers to the rate of reaction or how fast the transfer of one electron is occurring. Any kinetic description corresponding to any dynamic process must satisfy the thermodynamic form in the equilibrium limit [45]. For a general one-step, one-electron redox reaction,



The term (k_f) (forward reaction rate constant) can be found in literature corresponding to (k_c) , cathodic rate constant, and similarly (k_b) the backward reaction rate constant, to (k_a) the anodic reaction rate constant. The equilibrium limit is given by the Nernst equation,

$$(\phi_s - \phi_l)_{eq} = E_{eq} = E^\circ + \frac{rT}{nF} \ln \left(\frac{C_O^b}{C_R^b} \right) \quad (2.2)$$

and any kinetic formulation must satisfy this condition. In equation (2.2), (n) is the number of electrons, (F) is the Faraday constant, (r) is the universal gas constant and (T) is the temperature. The outlined relationship is derived from the standard Gibbs free energy change (ΔG_{rxn}°) , which determines whether the reaction is spontaneous $(\Delta G_{rxn}^\circ < 0)$ or non-spontaneous $(\Delta G_{rxn}^\circ > 0)$,

$$\Delta G_{rxn}^\circ = (\Delta G_R^\circ - \Delta G_O^\circ) \quad (2.3)$$

Where (ΔG_R°) and (ΔG_O°) are the standard free energies of the reduced species and oxidized species, respectively. Gibbs free energy change can be related to the standard electrode potential (E°) using the Faraday's constant,

$$\Delta G_{rxn}^\circ = nFE^\circ \quad (2.4)$$

It should be noted that,

$$E^\circ + \frac{rT}{nF} \ln \left(\frac{C_O^b}{C_R^b} \right) = E^\circ - \frac{rT}{nF} \ln \left(\frac{C_R^b}{C_O^b} \right) \quad (2.5)$$

. Equation (2.2) describes a situation under non-standard conditions, for instance, the concentrations (O) and (R) are not 1 molar (M). For the following formulation it is however assumed that $E_{eq} = E^\circ$.

Under the condition that the interfacial dynamics are the only constraint in the system, such that the delivery of reactants to the electrode surface is not considered, the current and overpotential are related by the Tafel equation,

$$\eta = \pm a \log \left(\frac{i_n}{i_0} \right) \quad (2.6)$$

where (η) is the overpotential, (a) is the Tafel slope, (i_n) is the net current density and (i_0) is the exchange current density. Considering the forward and backward pathways of the reaction (2.1) the rate of reduction (R_R) is related to the rate constant in the forward direction (k_f) and surface concentration of the oxidized species form (C_O^s) such that,

$$R_R = k_f C_O^s = \frac{i_c}{nFA} \quad (2.7)$$

where (i_c) is the cathodic current, and (A) is the cross-sectional area. Similarly, the rate of oxidation (R_O) is related to the backward rate constant (k_b) and the surface concentration of the reduced species form (C_R^s) by,

$$R_O = k_b C_R^s = \frac{i_a}{nFA} \quad (2.8)$$

where (i_a) is the anodic current. The net reaction rate (R_n) is then:

$$R_n = R_R - R_O = k_f C_O^s - k_b C_R^s = \frac{i_n}{nFA} \quad (2.9)$$

where (i_n) is the net current resulting from the anodic and cathodic current contributions. It should be noted that generally current is expressed as current density (A/m^2) and cross-sectional area can be omitted. Equation (2.9) can be rearranged to give,

$$i_n = i_c - i_a = nF[k_f C_O^s - k_b C_R^s] \quad (2.10)$$

Up to this point the formulation was based on the equilibrium condition where $E_{eq} = E^\circ$, meaning that $C_O^b = C_R^b = 1$ M. Let a further assumption be that $k_f C_O^s = k_b C_R^s$, making $k_f = k_b$. Thus, only under the outlined conditions the backward and forward rate constants can be expressed as:

$$k_f = k^\circ \exp(-\beta f(E - E^\circ)) \quad (2.11)$$

$$k_b = k^\circ \exp((1 - \beta)f(E - E^\circ)) \quad (2.12)$$

where β is the symmetry factor, k° is the standard rate constant and $f = F/rT$ with the assumption that $n = 1$. Substitution of (2.11) and (2.12) into (2.10) provides:

$$i_n = Fk^\circ [C_O^s \exp(-\beta f(E - E^\circ)) - C_R^s \exp((1 - \beta)f(E - E^\circ))] \quad (2.13)$$

Equation (2.13) can be seen in a different form, in which case the formulation differs by $R_{net} = R_O - R_R$, and $i_n = i_a - i_c$. Defining overpotential as:

$$\eta = E - E^\circ \quad (2.14)$$

$$i_n = Fk^\circ [C_R^s \exp((1 - \beta)f\eta) - C_O^s \exp(-\beta f\eta)] \quad (2.15)$$

The overpotential (2.14) refers to the standard free energy change of activation or the energy required to overcome the activation barrier and initiate the reaction. Other overpotentials are concentration and ohmic which will become evident in the forthcoming description. Throughout this work equation (2.15) and formulation leading to it is employed.

Under equilibrium condition $i_{net} = 0$ and equation (2.15) becomes:

$$Fk^\circ C_R^s \exp((1 - \beta)f\eta) = Fk^\circ C_O^s \exp(-\beta f\eta) \quad (2.16)$$

Furthermore, the implication of zero net current is that the surface concentrations of (O) and (R) are equal to that in the bulk meaning $C_O^b = C_R^b = C_O^s = C_R^s = 1 \text{ M}$.

Therefore,

$$\exp(f\eta) = \exp(f(E - E^\circ)) = \frac{C_O^b}{C_R^b} \quad (2.17)$$

Which can be rearranged to give equation (1.2),

$$E = E_{eq} = E^\circ + f \ln \left(\frac{C_O^b}{C_R^b} \right) \quad (2.18)$$

since $C_O^b = C_R^b = 1 \text{ M}$,

$$E = E_{eq} = E^\circ \quad (2.19)$$

and the equilibrium limit condition is satisfied. It is then apparent that for any kinetic description to be valid, regardless of its kinetic parameter variability, it should always come out as the Nernst equation at equilibrium. While there is an absence of net current at equilibrium, a parameter called the exchange current density (i_0) is established and is equivalent to the absolute magnitude of (i_c) and (i_a), note $i_c = -i_a$ or vice versa depending on notation used, at equilibrium. It follows that from (2.16),

$$i_0 = Fk^\circ C_O^b \exp(-\beta f\eta) \quad (2.20)$$

Raising (2.17) to the power $-\beta$,

$$\exp(-\beta f\eta) = \left(\frac{C_O^b}{C_R^b}\right)^{-\beta} \quad (2.21)$$

Substituting (2.21) into (2.20),

$$i_0 = Fk^\circ C_R^{b\beta} C_O^{b(1-\beta)} \quad (2.22)$$

Considering a special case where the bulk product and reactant concentrations are equal such that $C_O^b = C_R^b = C$,

$$i_0 = Fk^\circ C \quad (2.23)$$

Equation (2.20) provides a relationship between the exchange current density and the standard rate constant such that in combination with (2.15) yields,

$$i_n = i_0 \left[\frac{C_R^s}{C_R^b} \exp((1-\beta)f\eta) - \frac{C_O^s}{C_O^b} \exp(-\beta f\eta) \right] \quad (2.24)$$

and in the case where kinetics are not limited by concentration variation between the surface and bulk (see next section mass transport) also seen with the prior assumption of standard conditions

$$C_O^b = C_R^b = C_O^s = C_R^s = 1 \text{ M},$$

$$i_n = i_0 [\exp((1 - \beta)f\eta) - \exp(-\beta f\eta)] \quad (2.25)$$

Equations (2.24) and (2.25) serve as the backbone of electrode kinetics theory. It should be noted that although in the above formulation was based on standard conditions (standard concentration), it is no different under non-standard conditions, barring that the same assumptions are employed.

Where the supposition that $k_f C_O^s = k_b C_R^s$ cannot be made, such that $k_f \neq k_b$ and cannot be related to the standard rate constant k_0 , meaning equations (2.11) and (2.12) are no longer valid. Under such conditions,

$$k_f = k'_f \exp(-\beta f(E - E^0)) \quad (2.26)$$

$$k_b = k'_b \exp((1 - \beta)f(E - E^0)) \quad (2.27)$$

which are given in [48] [45]. The coefficients (k'_f) and (k'_b) and reference reaction constants. In [45] the relationship comes in quasi-reversible and irreversible multistep process, while [48] deals more with activation energy, intrinsic characteristic of a material, double layer, and quantum treatment all of which are outside this work. Substitution of (2.26) and (2.27) into (1.26) results in,

$$i_n = F [k_f C_R^s \exp((1 - \beta)f\eta) - k_b C_O^s \exp(-\beta f\eta)] \quad (2.28)$$

or in reaction rate form,

$$R = \frac{i_n}{F} = [k_f C_R^s \exp((1 - \beta)f\eta) - k_b C_O^s \exp(-\beta f\eta)] \quad (2.29)$$

Taking (2.29) and identifying that at some value of potential (E) the forward and backward reaction rates are at equilibrium (E_{eq}) [31][50],

$$k_f C_R^s \exp((1 - \beta)fE_{eq}) = k_b C_O^s \exp(-\beta fE_{eq}) \quad (2.30)$$

and solving for E_{eq} ,

$$E_{eq} = f \ln \left(\frac{k_b C_O^s}{k_f C_R^s} \right) \quad (2.31)$$

Then any deviation from E_{eq} results in overpotential, which is based on local concentrations, such that,

$$\eta = E - E_{eq} \quad (2.32)$$

Substituting (2.31) and (2.32) into (2.30) results in,

$$R = \frac{i_{net}}{F} = \left[k_f C_R^s \exp \left((1 - \beta)f\eta + (1 - \beta) \ln \left(\frac{k_b C_O^s}{k_f C_R^s} \right) \right) - k_b C_O^s \exp \left(-\beta f\eta - (1 - \beta) \ln \left(\frac{k_b C_O^s}{k_f C_R^s} \right) \right) \right] \quad (2.33)$$

from which,

$$i_0 = F k_f^{(\beta)} k_b^{(1-\beta)} C_R^{s(\beta)} C_O^{s(1-\beta)} \quad (2.34)$$

and using (2.34) with (2.33) to get,

$$i_n = i_0 [\exp((1 - \beta)f\eta) - \exp(-\beta f\eta)] \quad (2.35)$$

A seemingly identical equation to (2.25) yet not by the definition of the exchange current density, compare (2.22) and (2.34). The equilibrium potential can also be defined based on some known quantity, for instance inlet concentrations of two redox species in a reactor ($E_{eq,in}$), where,

$$k_f C_R^{in} \exp\left((1 - \beta)fE_{eq,in}\right) = k_b C_O^{in} \exp(-\beta fE_{eq,in}) \quad (2.36)$$

and,

$$E_{eq,in} = f \ln\left(\frac{k_b C_O^{in}}{k_f C_R^{in}}\right) \quad (2.37)$$

then,

$$\eta_{in} = E - E_{eq,in} \quad (2.38)$$

Substituting (2.37) and (2.38) into (2.30) result in,

$$i_n = i_0 \left[\frac{C_R^s}{C_R^{in}} \exp((1 - \beta)f\eta_{in}) - \frac{C_O^s}{C_O^{in}} \exp(-\beta f\eta_{in}) \right] \quad (2.39)$$

where,

$$i_0 = F k_f^{(\beta)} k_b^{(1-\beta)} C_R^{in(\beta)} C_O^{in(1-\beta)} \quad (2.40)$$

Furthermore, the overpotentials (2.32) and (2.38) are related such that,

$$\eta_{in} - \eta = f \ln\left(\frac{C_O^s / C_O^{in}}{C_R^s / C_R^{in}}\right) \quad (2.41)$$

The overpotential difference (2.41) is the concentration overpotential based on the equilibrium potential defined in (2.37). The concentration overpotential (2.41) can be used in a different manner to provide an “empirical” rather than “analytical” description of kinetics with respect to anodic and cathodic currents [51]. Beginning with,

$$\begin{aligned} i_n &= i_a + i_c \\ &= i_a g_a \exp(-\alpha_a f(E - E^*)) + i_c g_c \exp(-\alpha_c f(E - E^*)) \end{aligned} \quad (2.42)$$

Where (α_a) and (α_c) are the anodic and cathodic charge transfer coefficients corresponding to $(1 - \beta)$ and (β) , respectively, while (E^*) is potential arbitrary chosen with respect to a reference electrode. The utility of the charge transfer coefficient, as well as relation to symmetry factor (β) can be found in [52]. Meanwhile (g_a) and (g_c) are concentration ratios with respect to the reference concentration. Assuming $g_a = g_c = 1$, as well as $i_{net} = 0$ such that $E = E_{eq,ref}$ yields,

$$\begin{aligned} i_a \exp(-\alpha_a f(E_{eq,ref} - E^*)) &= i_c \exp(-\alpha_c f(E_{eq,ref} - E^*)) \\ &\equiv i_{0,ref} \end{aligned} \quad (2.43)$$

Where $(i_{0,ref})$ is the exchange current density with respect to reference conditions. Substituting (2.43) into (2.42),

$$\begin{aligned} i_n &= i_{0,ref} g_a \exp(-\alpha_a f(E_{eq,ref} - E^*)) \exp(-\alpha_a f(E - E^*)) \\ &\quad - i_{0,ref} g_c \exp(\alpha_c f(E_{eq,ref} - E^*)) \exp(-\alpha_c f(E - E^*)) \\ &= i_{0,ref} \left(g_a \exp(\alpha_a f(E - E_{eq,ref})) \right. \\ &\quad \left. - g_c \exp(-\alpha_c f(E - E_{eq,ref})) \right) \end{aligned} \quad (2.44)$$

Defining reference overpotential,

$$\eta_{ref} = (E - E_{eq,ref}) \quad (2.45)$$

$$i_n = i_{0,ref} \left(g_a \exp(\alpha_{af} \eta_{ref}) - g_c \exp(-\alpha_{cf} \eta_{ref}) \right) \quad (2.46)$$

Recognizing that equation (2.46) must satisfy the Nernst equation when $i_{net} = 0$,

$$\begin{aligned} i_{0,ref} g_a \exp(\alpha_{af} \eta_{eq,ref}) &= i_{0,ref} g_c \exp(-\alpha_{cf} \eta_{eq,ref}) \\ &\equiv i_0 \end{aligned} \quad (2.47)$$

where,

$$\eta_{eq,ref} = E_{eq} - E_{eq,ref} \quad (2.48)$$

Then substituting (2.47) into (2.46),

$$i_n = i_0 \left(\exp(\alpha_{af} (\eta_{ref} - \eta_{eq,ref})) - \exp(-\alpha_{cf} (\eta_{ref} - \eta_{eq,ref})) \right) \quad (2.39)$$

such that,

$$\eta_{ref} - \eta_{eq,ref} = E - E_{eq} \quad (2.50)$$

finally,

$$i_n = i_0 \left(\exp(\alpha_{af} \eta) - \exp(-\alpha_{cf} \eta) \right) \quad (2.51)$$

Equations (2.24), (2.25), (2.35), (2.39), (2.44) and (2.51) are all be called the Butler-Volmer equation, just different forms, and although they share the same name and serve the same purpose, their application is case specific. While it can certainly be acceptable to define the exchange current density, for instance, at some value derived from the Tafel plot, simply choosing to use it in any

form of Butler-Volmer equation without careful consideration of its applicability to a particular problem, may do nothing other than provide erroneous results.

2.3 Transport

The previous section dealt with electrode kinetics or interfacial reactions, what happens to ions after they leave the surface and the mechanisms of their transport in the electrolyte are required to describe the electrochemical phenomena pertaining to dilute solution theory. The dilute solution theory assumes that fluid flow is unaffected by species concentration. Ion transport in the electrolyte is often termed mass transfer and its formulation begins with the material derivative [53], yielding

$$\partial_t C + \nabla \cdot \mathbf{N} = R \quad (2.52)$$

where ($\partial_t C_i$) is accumulation, \mathbf{N} is the net flux density, (∇) is the flux divergence, and (R) is production due to homogeneous reaction. The species net flux density is given by the Nernst-Planck equation,

$$\mathbf{N}_i = z_i \mu_i F C_i \nabla \phi - D_i \nabla C_i + C_i \mathbf{u} \quad (2.53)$$

Where (z_i) is the valence, (μ_i) is mobility, (F) is the Faraday's constant, (C_i) is the species concentration, (ϕ) is the potential, (D_i) is the species diffusion coefficient and (\mathbf{u}) is the velocity vector. The right-hand terms from left to right correspond to the three modes of transport: migration, diffusion, and convection, respectively. Migration refers to the ion movement in an electric field, diffusion due to concentration gradient and convection due to the fluid bulk movement. Substitution of (2.53) into (2.52) yields,

$$\partial_t C_i + \nabla \cdot (z_i \mu_i F C_i \nabla \phi - D_i \nabla C_i + C_i \mathbf{u}) = R_i \quad (2.54)$$

In the presence of excess supporting electrolyte the migration term can be neglected [31] resulting in,

$$\partial_t C_i + \nabla \cdot (-D_i \nabla C_i + C_i \mathbf{u}) = R_i \quad (2.55)$$

then,

$$\partial_t C_i - D_i \nabla^2 C_i + \nabla \cdot (C_i \mathbf{u}) = R_i \quad (2.56)$$

$$\partial_t C_i - D_i \nabla^2 C_i + (\mathbf{u} \cdot \nabla C_i) + (C_i \nabla \cdot \mathbf{u}) = R_i \quad (2.57)$$

Due to incompressibility,

$$C_i \nabla \cdot \mathbf{u} = 0 \quad (2.58)$$

therefore,

$$\partial_t C_i - D_i \nabla^2 C_i + \mathbf{u} \cdot \nabla C_i = R_i \quad (2.59)$$

And if a system under consideration is at steady state ($\partial_t C_i = 0$),

$$-D_i \nabla^2 C_i + \mathbf{u} \cdot \nabla C_i = R_i \quad (2.60)$$

2.4 Current Distribution

Since the movement of ions is the source of current flow in the electrolyte, the current density can be related to species flux,

$$\mathbf{i} = F \sum_i (z_i \mathbf{N}_i) \quad (2.61)$$

Inserting (2.53) into (2.61) and expanding,

$$\mathbf{i} = -F^2 \nabla \phi \sum_i (z_i^2 \mu_i C_i) - F \sum_i (z_i D_i \nabla C_i) + F \mathbf{u} \sum_i (z_i C_i) \quad (2.62)$$

With the assumption of electroneutrality,

$$\sum_i (z_i C_i) = 0 \quad (2.63)$$

And in the absence of concentration variation in the solution (2.62) reduces to,

$$\mathbf{i} = -F^2 \nabla \phi \sum_i (z_i^2 \mu_i C_i) \quad (2.64)$$

Then defining conductivity,

$$\sigma = F^2 \sum_i (z_i^2 \mu_i C_i) \quad (2.65)$$

Equation (2.62) reduces to the Ohm's law expression:

$$\mathbf{i} = -\sigma \nabla \phi \quad (2.66)$$

2.5 Summary

This chapter focused on outlining the method based on some basic principles of electrochemistry applicable to this work. The extensive derivation of kinetics and thermodynamics was presented to elucidate and surmise the many ways a surface reaction of a redox couple can be looked at, depending on the type of BV kinetics used. The number of variables and their inclusion or absence there of, as outlined in Section 2.2, becomes extremely important in dissecting the results. Sections 2.3 and 2.4 described ionic transport in the bulk of the liquid and corresponding current following Ohm's law, respectively.

Chapter 3

Lattice Boltzmann Method Fundamentals

3.1 Introduction

Conventionally, transport of heat, mass and momentum is modeled using the continuum or discrete method. The continuum approach focuses on bulk transport of a quantity within a controlled space, requiring solution of Navier-Stokes (NS) equations which are non-linear partial differential equations (PDE). The non-linear nature of the NS equations poses many computational difficulties and requires conversion to a set of linear algebraic equation. Conversion into algebraic form can be done using finite discretization schemes such as finite volume, finite difference, and finite element. Finite volume and element are the most common numerical methods used in the ever increasingly sophisticated commercial software ANSYS Fluent and COMSOL, respectively. Domain discretization into grids, volumes, or elements, leads to macroscopic quantity (concentration, temperature, pressure etc.) evaluation of particles as a continuous entity.

On the opposite side of modeling transport phenomena is Molecular Dynamics (MD). As opposed to the continuum approach MD focuses on the microscale where individual intra-particle interaction and forces are of interest. This method is based on solving the ordinary differential momentum equation of Newton's second law and relates microscopic properties such as particle kinetic energy and particle boundary interaction to fundamental macroscopic material properties.

The aforementioned methods, wherein the number of particles present within a system is of exponential magnitude, can be limited by system size and computational cost, meanwhile for cases involving multi-phase or multi-component flows where interfaces are thermodynamically dominated because of molecular interactions, resolution of state equations can become problematic when solving the NS equations. Another approach that can address complex systems is the Lattice Boltzmann Method (LBM) [54]–[58]. LBM aims to connect the macro and micro scales by considering a population of particles, the meso-scale, rather than individual units, or a continuous system. The relatively straightforward coding requirement, enhanced boundary treatment and localized sub-domain extraction due to parallel architecture of LBM have attracted many researchers to adopt and augment this method in various fields [59]–[66]. The sections in this chapter are aimed at describing what the method is and its functionality. Its application to the problem is found in Chapters 5 and 6.

3.2 Discretized Boltzmann Equation and the BGK Approximation

Based on the kinetic theory of gases and evolving from the Lattice Gas Automata, LBM relies on the discretized form of the Boltzmann equation. The statistical system description (3.1), assuming absence of body forces or sources and sinks, revolves around populations of particles represented by the continuous distribution function f and the changes in the populations due to particle collisions, given by the collision integral $\Gamma(f, f)$ [57] [67] [68].

$$\partial_t f + \mathbf{u} \partial_x f = \Gamma(f, f) \quad (3.1)$$

The integration, of $\Gamma(f, f)$ for two particle collisions is satisfied by five collision invariants proportional to mass, momentum, and energy (see Appendix A). The notion that an isolated system, given enough time, should reach equilibrium was shown by Boltzmann using the H -theorem. The H function, according to the theorem, can never increase with time,

$$\partial_t H \leq 0 \quad (3.2)$$

therefore, any distribution function satisfying the Boltzmann equation satisfies equation (3.2). In the case of equality in (3.2) one solution to (3.1) is when f is the Maxwell-Boltzmann distribution function given as,

$$f^{eq}(\mathbf{x}, \mathbf{v}, t) = n \left(\frac{m}{2 \pi k_B T} \right)^{3/2} \exp \left(-\frac{m}{2 k_B T} (\mathbf{v} - \mathbf{u})^2 \right) \quad (3.3)$$

where the mean velocity \mathbf{u} is,

$$\mathbf{u} = \frac{1}{n} \int \mathbf{v} \mathbf{v} f(\mathbf{x}, \mathbf{v}, t) d^3 \mathbf{v} \quad (3.4)$$

wherewith, due to the local coordinate nature of (3.3), $f^{eq}(\mathbf{x}, \mathbf{v}, t)$ is only spatially dependant.

Operating in velocity and coordinate space, the distribution function $f(\mathbf{x}, \mathbf{u}, t)$ provides an account of the probability of finding particles at position vector \mathbf{x} , having a velocity vector \mathbf{u} , and at time t .

t. The collision integral related to systems involving fluid flows tends to be complicated, thus approximations are made. While there are several approximations, one of the most common collision operators used was proposed by Bhatnagar-Gross-Krook (BGK). The BGK operator Ω (3.5) approximates the changes in the distribution function $f(\mathbf{x}, \mathbf{u}, t)$ to be proportional to its deviation from the Maxwell-Boltzmann distribution function $f^{eq}(\mathbf{x}, \mathbf{u}, t)$ and introduces collision frequency ω .

$$\Omega^{\text{BGK}} = \omega(f^{eq} - f) \quad (3.6)$$

The distribution function is discretized by restricting the velocity space to a finite set of velocities c_i , yielding the space and time dependent discrete-velocity distribution function $f_i(x, t)$. Thus, the discrete Boltzmann equation with the BGK approximation yields,

$$\partial_t f_i + u_i \nabla f_i = -\frac{1}{\tau} (f_i - f_i^{eq}) \quad (3.7)$$

where the relaxation time constant $\tau = 1/\omega$ and should fall within $0.5 \leq \tau \leq 2$. Dimensional analysis considering the time between particle collisions t_c , reference density ρ_{ref} , reference speed u_{ref} and characteristic length scale L results in the following non-dimensional parameters:

$$c_i = \frac{u_i}{u_{ref}} \quad \tilde{\nabla} = L \nabla \quad \tilde{t} = \frac{t_c u_{ref}}{L} \quad \tilde{\tau} = \frac{\tau}{t_c} \quad \tilde{f}_i = \frac{f_i}{\rho_{ref}} \quad (3.8)$$

substitution of which into (2.7) results in,

$$\tilde{\partial}_t \tilde{f}_i + c_i \tilde{\nabla} \tilde{f}_i = -\frac{L}{\tilde{\tau} t_c u_{ref}} (\tilde{f}_i - \tilde{f}_i^{eq}) \quad (3.9)$$

where $\frac{t_c u_{ref}}{L}$ is the Knudsen (Kn) number, which describes the ratio of the mean free path to characteristic length as well as the collision and flow time. It should be noted that the Boltzmann

equation is applicable to most flow regimes as it is valid for $Kn < 100$ [69] while NS is only for $Kn < 0.1$ [70]. Discretizing (3.9) with respect to space and time [71],

$$\begin{aligned}
 & \frac{\tilde{f}_i(\tilde{\mathbf{x}}, \tilde{t} + \Delta\tilde{t}) - f_i(\tilde{\mathbf{x}}, \tilde{t})}{\Delta\tilde{t}} + c_{ix} \frac{\tilde{f}_i(\tilde{\mathbf{x}} + \Delta\tilde{x}, \tilde{t} + \Delta\tilde{t}) - \tilde{f}_i(\tilde{\mathbf{x}}, \tilde{t} + \Delta\tilde{t})}{\Delta\tilde{x}} \\
 & + c_{iy} \frac{\tilde{f}_i(\tilde{\mathbf{x}} + \Delta\tilde{y}, \tilde{t} + \Delta\tilde{t}) - \tilde{f}_i(\tilde{\mathbf{x}}, \tilde{t} + \Delta\tilde{t})}{\Delta\tilde{y}} \\
 & + c_{iz} \frac{\tilde{f}_i(\tilde{\mathbf{x}} + \Delta\tilde{z}, \tilde{t} + \Delta\tilde{t}) - \tilde{f}_i(\tilde{\mathbf{x}}, \tilde{t} + \Delta\tilde{t})}{\Delta\tilde{z}} \\
 & = -\frac{1}{\tilde{\tau}Kn} (\tilde{f}_i - \tilde{f}_i^{eq})
 \end{aligned} \tag{3.10}$$

and defining lattice velocity $\mathbf{c}_i = \Delta\tilde{\mathbf{x}} / \Delta\tilde{t}$, with $\Delta\tilde{t} = \Delta t U/L$,

$$\begin{aligned}
 & \frac{\tilde{f}_i(\tilde{\mathbf{x}}, \tilde{t} + \Delta\tilde{t}) - f_i(\tilde{\mathbf{x}}, \tilde{t})}{\Delta\tilde{t}} + \frac{\tilde{f}_i(\tilde{\mathbf{x}} + \mathbf{c}_i \Delta\tilde{t}, \tilde{t} + \Delta\tilde{t}) - \tilde{f}_i(\tilde{\mathbf{x}}, \tilde{t} + \Delta\tilde{t})}{\Delta\tilde{t}} \\
 & = -\frac{1}{\tilde{\tau}Kn} (\tilde{f}_i - \tilde{f}_i^{eq})
 \end{aligned} \tag{3.11}$$

which simplifies to,

$$\frac{\tilde{f}_i(\tilde{\mathbf{x}} + \mathbf{c}_i \Delta\tilde{t}, \tilde{t} + \Delta\tilde{t}) - \tilde{f}_i(\tilde{\mathbf{x}}, \tilde{t})}{\Delta\tilde{t}} = -\frac{1}{\tilde{\tau}Kn} (\tilde{f}_i - \tilde{f}_i^{eq}) \tag{3.12}$$

yielding the discretized lattice Boltzmann equation (LBE), the backbone of LBM (note the dimensionless identifier is dropped henceforth):

$$f_i(\mathbf{x} + \mathbf{c}_i dt, t + dt) - f_i(\mathbf{x}, t) = -\frac{1}{\tau} (f_i - f_i^{eq}) \tag{3.13}$$

3.3 Lattice Structure

Analogous to the domain discretization schemes used in solving NS equations for fluid flow, LBM velocity domain is divided into lattice sites. Lattice models depend on the space dimension n and the number of required velocities m , which can be also thought of as directions of information transfer, at each lattice site and are identified as $D_n Q_m$ (Figure 2). Some common lattice structures are $D_1 Q_3$, referring to one dimensional space with three discrete velocities, and following the same description $D_2 Q_9$ and $D_3 Q_{19}$. In the subsequent discussion this work will mainly refer to $D_2 Q_9$. Although $D_1 Q_3$ is also used, its derivation is excluded, as the procedure is the same for all lattice models.

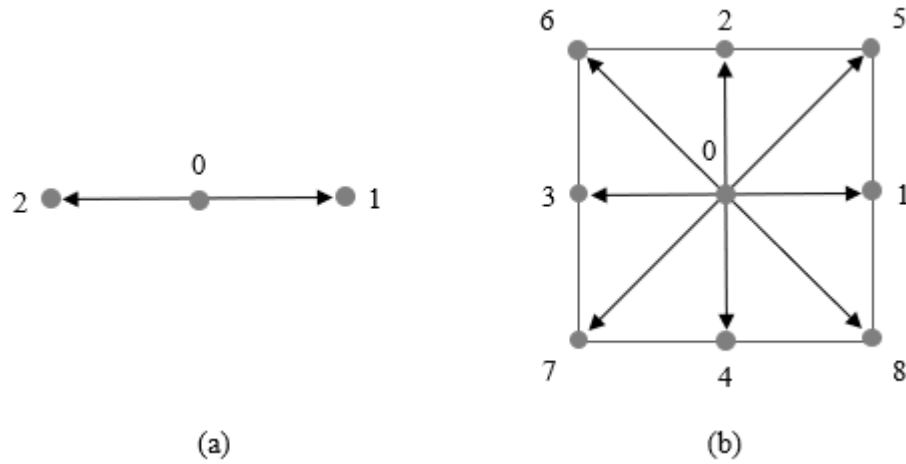


Figure 2: Lattice Models: (a) $D_1 Q_3$ (b) $D_2 Q_9$

The discrete unit velocities c_i , for D_2Q_9 , are given by the following,

$$\begin{aligned}
 c_0 &= (0,0) \\
 c_i &= c \left[\cos\left(\frac{(i-1)\pi}{2}\right), \sin\left(\frac{(i-1)\pi}{2}\right) \right] \quad i = 1,2,3,4 \\
 c_i &= \sqrt{2}c \left[\cos\left(\frac{(2i-1)\pi}{4}\right), \sin\left(\frac{(2i-1)\pi}{4}\right) \right] \quad i = 5,6,7,8
 \end{aligned} \tag{3.14}$$

resulting in,

$$\begin{aligned}
 c_1 &= (1,0) & c_2 &= (0,1) & c_3 &= (-1,0) & c_4 &= (0,-1) \\
 c_5 &= (1,1) & c_6 &= (-1,1) & c_7 &= (-1,-1) & c_8 &= (1,-1)
 \end{aligned} \tag{3.15}$$

The equilibrium distribution function is determined as,

$$f_i^{eq} = w_i \rho \left\{ 1 + \frac{(c_i \cdot \mathbf{u})}{c_s^2} + \frac{1}{2} \frac{(c_i \cdot \mathbf{u})^2}{c_s^4} - \frac{1}{2} \frac{\mathbf{u}^2}{c_s^2} \right\} \tag{3.16}$$

where ρ and \mathbf{u} are macroscopic density and velocity vector, respectively. The lattice velocity of sound is $c_s = c/\sqrt{3}$ and w_i is the weighting factor, which dictates the amount of information passed along each lattice link and is assigned as follows,

$$\begin{aligned}
 w_i &= \frac{4}{9} & i &= 0 \\
 w_i &= \frac{1}{9} & i &= 1,2,3,4 \\
 w_i &= \frac{1}{36} & i &= 5,6,7,8
 \end{aligned} \tag{3.17}$$

For D_1Q_3 the corresponding values are,

$$\begin{aligned}
 w_i &= \frac{4}{6} & i &= 0 \\
 w_i &= \frac{1}{6} & i &= 1,2
 \end{aligned} \tag{3.18}$$

3.4 Collision and Streaming

Any LBM algorithm relies on two main computation stages, local collision and streaming as shown in Figures 3 and 4, respectively. The collision step involves calculation of the equilibrium distribution function followed by the collision operator. The post collision value of the distribution function is updated, and the change is communicated to the neighbouring lattice sites/nodes within the domain via the streaming step. The local dependence of the distribution function highlights the parallel environment of LBM.

Collision:

$$f_i(x, t)^{new} = f_i(x, t)^{old} + \frac{1}{\tau} (f_i(x, t) - f_i^{eq}(x, t)) \quad (3.19)$$

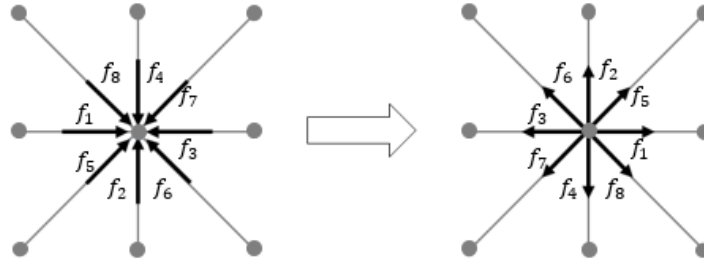


Figure 3: Collision Step

Streaming:

$$f_i(x + c_i dt, t + dt) = f_i(x, t)^{new} \quad (3.20)$$

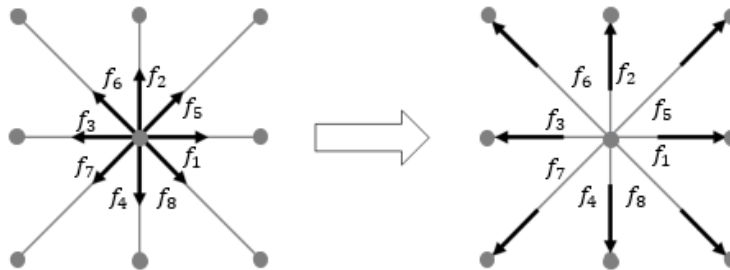


Figure 4: Streaming Step

Once the discrete populations are known, the density and velocity are solved for by the summation of all discrete lattice velocities, resulting in the following conservation equations (ρ is conventionally used in explanations pertaining to fluids),

$$\rho = \sum_i f_i \quad (3.21)$$

$$\mathbf{u} = \frac{1}{\rho} \sum_i \mathbf{c}_i f_i \quad (3.22)$$

$$\mathbf{\Pi} = \sum_i \mathbf{q}_i f_i \quad (3.23)$$

3.5 Multi-Scale Expansion for Fluid Dynamics

Hitherto, the transition between the PDE's of NS and the LBE of LBM has not been clarified. The commonly applied conservation of mass [72],

$$\partial_t \rho + \nabla \cdot (\rho \mathbf{u}) = 0 \quad (3.24)$$

which, depending on the nature of evaluation, is also referred to as continuity and species conservation, momentum,

$$\partial_t \rho + \nabla \cdot (\rho \mathbf{u} \mathbf{u} + \rho \mathbf{I} - \boldsymbol{\gamma}) = \rho \mathbf{G} \quad (3.25)$$

and energy,

$$\partial_t E + \nabla \cdot ((\rho E + \rho) \mathbf{u} - \kappa \nabla T - (\mathbf{u} \cdot \boldsymbol{\gamma})^T) = \rho(q + \mathbf{G} \cdot \mathbf{u}) \quad (3.26)$$

are a requirement to be fulfilled regardless of their form. Elaborating on (3.21 and 3.22) the LBM conservation of mass,

$$\rho = \sum_i f_i = \sum_i f_i^{eq} = \sum_i f_i^{(0)} \quad (3.27)$$

$$\sum_i f_i^{(1)} = 0 = \sum_i r \Omega_i^{(1)} \quad (3.28)$$

$$\sum_i f_i^{(2)} = 0 = \sum_i \Omega_i^{(2)} \quad (3.29)$$

and momentum,

$$(\rho \mathbf{u}) = \sum_i \mathbf{c}_i f_i = \sum_i \mathbf{c}_i f_i^{eq} = \sum_i \mathbf{c}_i f_i^{(0)} \quad (3.30)$$

$$\sum_i f_i^{(1)} = 0 = \sum_i \Omega_i^{(1)} \quad (3.31)$$

$$\sum_i \mathbf{c}_i f_i^{(1)} = 0 = \sum_i \mathbf{c}_i \Omega_i^{(1)} \quad (3.32)$$

$$\sum_i \mathbf{c}_i f_i^{(2)} = 0 = \sum_i \mathbf{c}_i \Omega_i^{(2)} \quad (3.33)$$

where the superscripts refer to the moment order, are mathematically analyzed spatially and temporally via the Chapman-Enskog expansion [73]. Where with the assumption that ε is small, expanding f_i around the local equilibrium $f_i^{(eq)}$,

$$f_i = f_i^{(eq)} + \varepsilon f_i^{(1)} + \varepsilon^2 f_i^{(2)} + \mathcal{O}(\varepsilon^3) \quad (3.34)$$

similarly,

$$\Omega_i = \varepsilon \Omega_i^{(1)} + \varepsilon^2 \Omega_i^{(2)} + \mathcal{O}(\varepsilon^3) \quad (3.35)$$

$$\partial_t = \varepsilon \partial_t^{(1)} + \varepsilon^2 \partial_t^{(2)} + \mathcal{O}(\varepsilon^3) \quad (3.36)$$

$$\nabla = \varepsilon \nabla^{(1)} + \varepsilon^2 \nabla^{(2)} + \mathcal{O}(\varepsilon^3) \quad (3.37)$$

and the Taylor expansion of which recovers the PDE's of NS. Since the expansion of the distribution function is typically truncated to the second order, LBM is said to be second order accurate. The moment order requirement is dependent on the scale of $\mathcal{O}(\varepsilon, \varepsilon^2, \varepsilon^3, \dots)$. In the case of advection-diffusion with a force term the collision operator becomes [72]

$$\Omega = -\frac{1}{\tau} (f_i - f_i^{eq}) + w_i \mathbf{c}_i \cdot \mathbf{F} \quad (3.38)$$

having the requirement of $\mathcal{O}(\varepsilon)$. The force term is added to the collision operator in the presence of body forces, sources, and sinks. Using the Chapman-Enskog expansion continuity becomes,

$$\begin{aligned} \partial_t \rho + \varepsilon \nabla^{(1)} \cdot (\rho \mathbf{u})^{(0)} \\ = \varepsilon \nabla^{(1)} \cdot \left((\rho \mathbf{u})^{(1)} + \frac{1}{2} \partial_t^{(1)} (\rho \mathbf{u})^{(0)} + \frac{1}{2} \nabla^{(1)} \Pi^{(0)} + \frac{1}{2} c_s^2 \nabla^{(1)} \rho \right)_1 \end{aligned} \quad (3.39)$$

the Taylor expansion of the collision operator yielding,

$$\begin{aligned} f_i^{(1)} &= w_i \tau \left(\partial_t^{(1)} + \nabla \cdot \mathbf{c}_i \right) \left[\rho \left(1 + \frac{1}{c_s^2} \mathbf{c}_i \cdot \mathbf{u} \right) \right] + \tau w_i \mathbf{c}_i \cdot (\rho \mathbf{u}) \\ &= \frac{\tau}{c} \mathbf{Q} : \nabla (\rho \mathbf{u}) - \tau w_i \mathbf{c}_i \nabla \rho - \frac{\tau}{c_s^2} w_i \partial_t^{(1)} \mathbf{c}_i (\rho \mathbf{u}) + \tau w_i \mathbf{c}_i (\rho \mathbf{u}) \end{aligned} \quad (3.40)$$

Then after some manipulation recovering the PDE,

$$\partial_t \rho + \nabla \cdot (\rho \mathbf{u}) = D \nabla^2 \rho + \frac{D}{c_s^2} \partial_t \nabla \cdot (\rho \mathbf{u}) - \tau c_s^2 \nabla \cdot (\rho \mathbf{u}) \quad (3.41)$$

where the diffusivity constant D is,

$$D = c_s^2 \left(\tau - \frac{1}{2} \right) \quad (3.42)$$

Equation (3.41) is then seen to recover the $\mathcal{O}(\varepsilon^2)$ scale. The last two terms of (3.41) are treated as the force term and the momentum error term arising from the derivation, respectively. The error term can be adjusted as it is a free parameter, and has also been elaborated on its inclusion in [74].

A recent review on various force terms can be found in [75].

3.6 Boundary Conditions (BC)

Any system simulation using any numerical method requires a controlled environment, be it any dimension, any control volume, element etc. The isolated domain, regardless of the phenomena investigated must have something that is known, to serve as a guide, such as the lighthouse identifies the shore for sailing ships, for without it the water cars would have no way of knowing of the existing danger and likely meet their demise. Analogous, is the purpose of boundary conditions, imposing a condition, an identification of a constant or known occurrence (independent variable). Various types of LBM boundary conditions (inlet, wall, etc.) have been proposed [76]–[79] and generally, since they are all based on the distribution function, their implementation is less strenuous compared to other conventional numerical methods. The straightforwardness of the LBM BC's makes this method particularly suitable for flows involving complex geometries such as porous media. The distribution functions are all that is required to recover the macroscopic properties in question, however as highlighted in Figure 5, some are unknown. For example, after streaming the west node has three unknowns, f_1 , f_5 and f_8 due to the lack of preceding information. Therefore, in applying any BC, determination of the unknown distribution functions requires knowledge of the macroscopic properties at the respective boundaries. In the following, only the BC's pertinent to this work are presented.

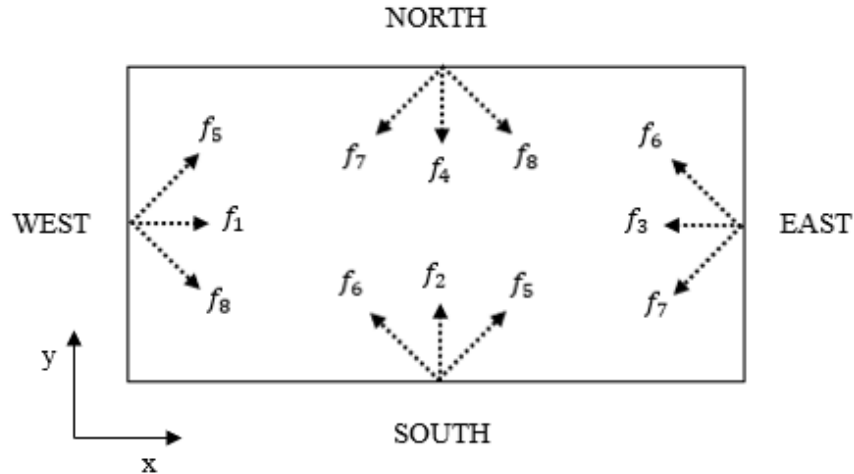


Figure 5: Unknown Distribution Functions

3.6.1 No-slip Wall BC

The no-slip wall BC, a stationary condition assigned to the north wall, requires f_4 , f_7 and f_8 . These unknowns can be solved using the bounce-back scheme, which is premised on the elastic behavior of particles colliding with a solid object and resulting in their deflection. As seen in Figure 6, with the bounce-back method the unknown distribution functions can be found by their opposites.

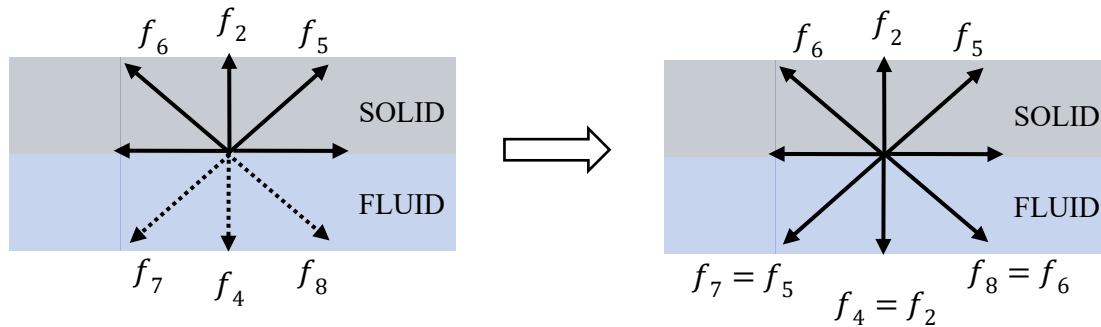


Figure 6: Bounce-Back Method

3.6.2 Zero-Gradient BC

In some situations, the flux is known (Newmann boundary) rather than some macroscopic value (Dirichlet boundary). Furthermore, in cases such as considering fully developed flow at the channel outlet (Figure 5, east), where the axial velocity gradient negligible, the zero-gradient BC can be imposed,

$$\partial_x u = 0 \quad (3.43)$$

Using finite differencing to discretize (2.43) yields,

$$u_x = u_{x-1} \quad (3.44)$$

where x is the boundary location. Considering zero-gradient BC at the east boundary (Figure 5), the unknown distribution functions can be found as,

$$\begin{aligned} f_3(x) &= f_3(x - 1) \\ f_6(x) &= f_6(x - 1) \\ f_7(x) &= f_7(x - 1) \end{aligned} \quad (3.45)$$

3.6.3 Velocity BC

The velocity boundary, or velocity inlet BC if referring to (Figure 5, west), is applied when the magnitude of normal (u) and tangential (v) components are known while density (ρ) is not. Thus, there are four unknowns, f_1, f_5, f_8 and ρ requiring four equations. Three equations can be extracted from the macroscopic boundary properties (3.21 and 3.22),

$$\begin{aligned} \rho &= f_0 + f_1 + f_2 + f_3 + f_4 + f_5 + f_6 + f_7 + f_8 \\ \rho u &= f_1 + f_5 + f_8 - f_3 - f_6 - f_7 \end{aligned} \quad (3.46)$$

$$\rho v = f_2 + f_5 + f_6 - f_4 - f_7 - f_8$$

The fourth equation was proposed by [80] which relates the non-equilibrium parts of the opposite distribution functions such that,

$$f_\alpha^{neq} = f_\beta^{neq} \quad (3.47)$$

and when applied to the west boundary results in,

$$f_3 - f_3^{eq} = f_1 - f_1^{eq} \quad (3.48)$$

$$\begin{aligned} f_3 - w_3 \rho \left\{ 1 + \frac{\mathbf{c}_3 \cdot \mathbf{u}}{c_s^2} + \frac{1}{2} \frac{(c_3 \cdot u)^2}{c_s^4} - \frac{1}{2} \frac{u^2 + v^2}{c_s^2} \right\} \\ = f_1 - w_1 \rho \left\{ 1 + \frac{\mathbf{c}_1 \cdot \mathbf{u}}{c_s^2} + \frac{1}{2} \frac{(c_1 \cdot u)^2}{c_s^4} - \frac{1}{2} \frac{u^2 + v^2}{c_s^2} \right\} \end{aligned} \quad (3.49)$$

$$\begin{aligned} f_3 - \frac{1}{9} \rho \left\{ 1 + \frac{(-u)}{c_s^2} + \frac{1}{2} \frac{(-u)^2}{c_s^4} - \frac{1}{2} \frac{u^2 + v^2}{c_s^2} \right\} \\ = f_1 - \frac{1}{9} \rho \left\{ 1 + \frac{(u)}{c_s^2} + \frac{1}{2} \frac{(u)^2}{c_s^4} - \frac{1}{2} \frac{u^2 + v^2}{c_s^2} \right\} \end{aligned} \quad (3.50)$$

$$f_3 - \frac{1}{9} \rho \left\{ \frac{(-u)}{c_s^2} \right\} = f_1 - \frac{1}{9} \rho \left\{ 1 + \frac{(u)}{c_s^2} \right\} \quad (3.51)$$

Assuming uniform velocity $\mathbf{u} = (u, 0)$ at the boundary and substitution of the equilibrium distribution function components into (3.49) leads to,

$$f_1 = f_3 + \frac{2}{3} \rho u \quad (3.52)$$

Once f_1 is calculated and after simplifying the remaining unknowns can be found with,

$$\rho = \frac{f_0 + f_2 + f_4 + 2(f_3 + f_6 + f_7)}{1 - u} \quad (3.53)$$

$$f_5 = f_7 - \frac{1}{2}(f_2 - f_4) + \frac{1}{6} \rho u \quad (3.54)$$

$$f_8 = f_6 + \frac{1}{2}(f_2 - f_4) + \frac{1}{6} \rho u \quad (3.55)$$

The outlined method requires that the entrance velocity be known and was assumed uniform. If the channel velocity profile is parabolic, it can be defined as [81] ,

$$u = \frac{-4 u_m}{H^2} y^2 + \frac{4 u_m}{H} y \quad (3.56)$$

where u_m is the maximum velocity and H is the channel height.

3.6.4 Constant BC

In instances where the macroscopic property such as temperature or concentration is known to be constant, for example West (Figure 5), the unknowns can be found as follows [82],

$$f_1 = T_w(w_1 + w_3) - f_3 \quad (3.57)$$

$$f_5 = T_w(w_5 + w_7) - f_7 \quad (3.58)$$

$$f_8 = T_w(w_8 + w_6) - f_6 \quad (3.59)$$

Furthermore, if advection is involved [83],

$$f_1 + f_5 + f_8 = \frac{1}{6} T' (1 + 3u + 3u^2) \quad (3.60)$$

where T' is treated as an auxiliary parameter. From conservation (equation 3.21)

$$T' = \frac{6}{(1 + 3u + 3u^2)} (T - (f_0 + f_2 + f_3 + f_4 + f_6 + f_7)) \quad (3.61)$$

and substitution of T' into the equilibrium distribution function allows the determination of the unknowns.

3.6.5 Corner Nodes

Special treatment is required for the corner nodes since even after applying boundary conditions some distribution functions remain unknown. As seen in Figure 7, looking at the N-W corner for example, finding f_5 with the bounce-back scheme is not possible since f_7 is not known. Such cases can be solved by letting,

$$\begin{aligned} f_1 &= f_3 \\ f_8 &= f_6 \end{aligned} \tag{3.62}$$

and using equation (3.21) while recognizing that,

$$f_5 = f_7 \tag{3.63}$$

the other unknowns can be found by,

$$f_5 = 0.5(\rho - (f_0 + f_1 + f_2 + f_3 + f_4 + f_6 + f_8)) \tag{3.64}$$

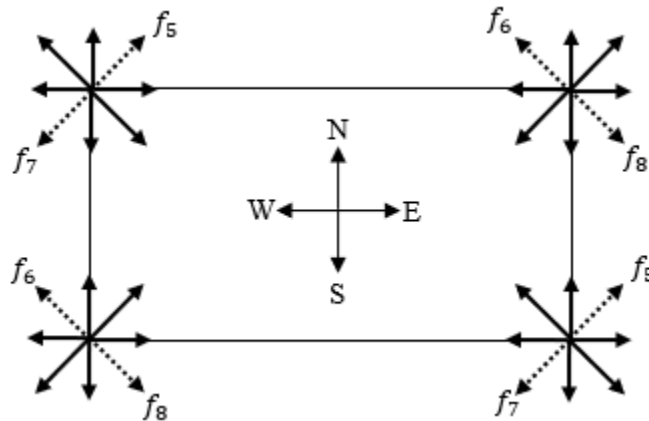


Figure 7: Corner Treatment

Chapter 4

Model Development

4.1 Introduction

The focus of this chapter is to develop a mathematic model, followed by the dimensional analysis and scale conversion to lattice units, required to simulate redox surface reactions. The dimensional analysis establishes the relationship between the fluid dynamics and the electrochemical phenomena within flow-through porous electrodes. The derived relationship is then used to develop a new pseudo-porous LBM algorithm which can simulate the unknown potentials and concentrations simultaneously via the addition of a reaction source/sink to the distribution function. Subsequently, the algorithm is augmented to mimic a physical two-dimensional porous structure. The interfacial species consumption and production is modelled through enhanced concentration boundary conditions as opposed to reaction sources/sinks used with the pseudo-porous condition.

4.2 Mathematical Model for Electrochemical Reaction in a Flow-Through Porous Electrode

Insulation effects and porous electrode structural changes are neglected while due to low concentration of reacting species. Considering the low concentration of reacting species present in the system, the conductivity of the electrolyte is assumed constant based on the data provided in literature for drinking water. Ion and electron transport is defined by Ohm's law according to,

$$i_s = -\sigma_s \frac{d\phi_s}{dx} \quad (4.1)$$

$$i_l = -\sigma_l \frac{d\phi_l}{dx} \quad (4.2)$$

The conductivities for both solid (σ_s) and liquid phases (σ_l) are assumed position independent. Within the porous electrode, current density change in the electrolyte (i_l) is dependent on current density (i_n) crossing the electrode/electrolyte interface by reaction [30],

$$\frac{di_l}{dx} = a i_n \quad (4.3)$$

Charge balance is also required, which is defined by the following equation,

$$\frac{di_s}{dx} + \frac{di_l}{dx} = 0 \quad (4.4)$$

Differentiating equations (4.1) and (4.2) and substituting from (4.3) and (4.4) yield the partial differential equations relating the potential distribution and the reaction current density in the solid and liquid phases of the porous electrode, according to equations (4.5) and (4.6) respectively,

$$\frac{d^2\phi_s}{dx^2} = -\frac{a i_n}{\sigma_s} \quad (4.5)$$

$$\frac{d^2\varphi_l}{dx^2} = -\frac{a i_n}{\sigma_l} \quad (4.6)$$

It should be noted that equations (4.3),(4.5) and (4.6) utilize specific surface area a for the pseudo-porous condition, which is dropped for the physical porous geometry. The kinetics of the redox reaction are described by the Butler-Volmer equation,

$$i_n = i_o \left[\frac{c_R}{c^\circ} \exp(\alpha_a f \eta_{in}) - \frac{c_O}{c^\circ} \exp(-\alpha_c f \eta_{in}) \right] \quad (4.7)$$

The overpotential, η , is calculated by,

$$\eta = \varphi_s - \varphi_l - E_{eq} \quad (4.8)$$

The steady state mass balance yields the relationship between the species concentration and the reaction rate,

$$\nabla \cdot N_i = R \quad (4.9)$$

In a dilute electrolyte flowing through a porous electrode, the flux of mobile ionic species is dominated by diffusion and convection,

$$N_i = -D_i \frac{dC_i}{dx} + vC_i \quad (4.10)$$

For the pseudo-porous model, the effective concentration diffusivity is calculated according to the Millington and Quirck model [84],

$$D_{i(eff)} = \frac{\lambda_p}{\zeta_i} D_i \quad (4.11)$$

where tortuosity ζ is related to porosity λ as,

$$\zeta_i = \lambda_p^{-1/3} \quad (4.12)$$

The effective liquid phase conductivity in the porous electrode was estimated by the Bruggeman equation [85],

$$\sigma_l = \sigma_{l,0} \times \lambda_l^{1.5} \quad (4.13)$$

where ε is the fraction of volume occupied by the liquid phase in the porous electrode

4.3 Dimensional Analysis of the Continuity Equation

A common method to model fluid phenomena is with the use of dimensionless numbers which, in essence, provide information as to ‘what’ and ‘how’. From the dimensional analysis of the NS continuity equation [86], one of those is the Reynolds number (Re),

$$Re = \frac{L u}{\nu} \quad (4.14)$$

where L is the characteristic length, u is the velocity and ν is the kinematic viscosity. Other dimensionless numbers include Prandtl (Pr), Schmidt (Sc), Peclet (Pe) and Damkohler (Da). Dimensionless numbers are anchors that provide a pathway for modeling various phenomena using different scales. As seen in Figure 8, systems with different scales are connected via the same dimensionless number and therefore should yield the same results [87]. The lattice scale N is number of lattices required.

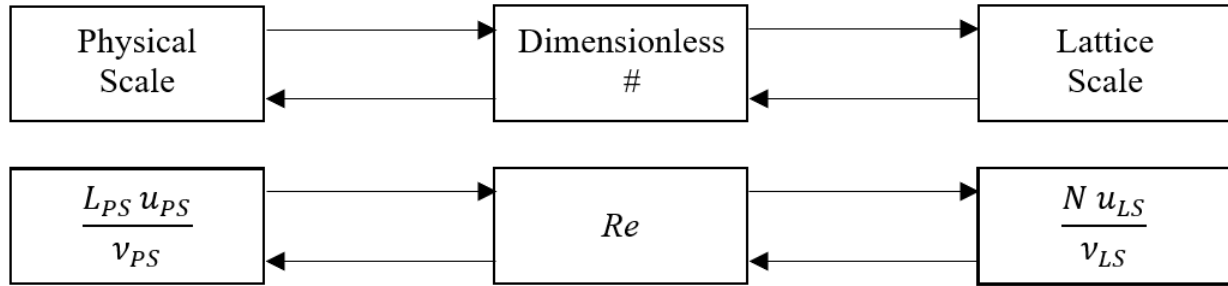


Figure 8: Physical, Dimensionless and Lattice Scale Relationship

As previously mentioned, there is no dimensionless number suitable for the particular electrochemical problem. The forthcoming dimensional analysis for the developed pseudo-porous mathematical model in the previous section largely follows Brushett *et al.* [31]. The continuity

equation with reaction rate as species source/sink, presented in previous section, is dimensionally analyzed as follows.

$$\frac{\partial C}{\partial t} + \nabla \cdot \mathbf{N} = R \quad (4.15)$$

$$u\nabla C - D\nabla^2 C = \frac{sa i_n}{nF} \quad (4.16)$$

where s is the stoichiometric coefficient, a is the specific surface area, n is the number of electrons and F is the Faraday's constant. Multiplying both sides by L^2/C_0 ,

$$u\nabla C \frac{L^2}{C_0} - D\nabla^2 C \frac{L^2}{C_0} = \frac{sa i_n L^2}{nF C_0} \quad (4.17)$$

followed by division by uL ,

$$\tilde{\nabla} \tilde{C} - \frac{D}{uL} \tilde{\nabla}^2 \tilde{C} = \frac{saLi_n}{unFC_0} \quad (4.18)$$

then relating $f(\varphi) = i_n/i_o$ where,

$$f(\varphi) = \frac{i_n}{i_o} = \frac{\left[\frac{C_R}{C^\circ} \exp(\alpha_a f \eta_{in}) - \frac{C_O}{C^\circ} \exp(-\alpha_c f \eta_{in}) \right]}{1 + \frac{i_o}{i_{lim}} \left[\frac{C_R}{C^\circ} \exp(\alpha_a f \eta_{in}) + \frac{C_O}{C^\circ} \exp(\alpha_c f \eta_{in}) \right]} \quad (4.19)$$

and inserting (4.18) into (4.17) gives,

$$\tilde{\nabla} \tilde{C} - \frac{D}{uL} \tilde{\nabla}^2 \tilde{C} = \frac{saLi_o}{unFC_0} f(\varphi) \quad (4.20)$$

The dimensionless reducing and oxidizing agent concentrations are normalized by standard concentration,

$$\tilde{C}_R = \frac{C_R}{C^\circ} \quad (4.19)$$

$$\tilde{C}_O = \frac{C_O}{C^\circ} \quad (4.20)$$

Defining the ratio of the exchange and limiting currents,

$$\theta = \frac{i_o}{i_{lim}} \quad (4.21)$$

while the dimensionless potential is normalized by $F/rT, V^{-1}$

$$\tilde{\varphi} = \frac{F\varphi}{rT} \quad (4.22)$$

giving the following relationship for dimensionless overpotential,

$$\tilde{\eta} = \tilde{\varphi}_s - \tilde{\varphi}_l - \tilde{\varphi}_{eq} \quad (4.23)$$

The dimensionless form of equation (4.18) is then

$$f(\tilde{\varphi}) = \frac{i_n}{i_o} = \frac{[\tilde{C}_R \exp(\alpha_a \tilde{\eta}) - \tilde{C}_O \exp(-\alpha_c \tilde{\eta})]}{1 + \theta [\tilde{C}_R \exp(\alpha_a \tilde{\eta}) + \tilde{C}_O \exp(\alpha_c \tilde{\eta})]} \quad (4.24)$$

Recognizing that,

$$\frac{1}{Pe} = \frac{D}{uL} \quad (4.25)$$

where Pe is the Peclet number relating the dominance of advection and diffusion. Letting,

$$\tilde{R} = \frac{saLi_o}{unFC_o} \quad (4.26)$$

yields the dimensionless continuity equation,

$$\tilde{\nabla} \tilde{C} - \frac{1}{Pe} \tilde{\nabla}^2 \tilde{C} = \tilde{R} f(\tilde{\varphi}) \quad (4.27)$$

where \tilde{R} is a constant and should be normalized given the range of evaluation. For example,

varying C_o between 0.01 and 0.02, \tilde{R} would correspond to 1 and 0.5, respectively. Similarly, the

overpotential is related to current as,

$$\frac{\partial^2 \tilde{\varphi}}{\partial \tilde{x}^2} = \tilde{K} f(\tilde{\varphi}) \quad (4.28)$$

where constant \tilde{K} is,

$$\tilde{K} = \frac{FaL^2i_o}{\sigma_{eff}rT} \quad (4.29)$$

In some cases, the quantity advected and/or diffused is a scalar such as temperature and concentration, seen in Chapter 5. If the flow is reactionless, the species conservation follows equation 2.57, similarly for temperature. The methodology for scale conversion, in the absence of a dimensionless number, is formulated around selecting dimensionless reference parameters and base dimensions as outlined in [86] [88]. All systems can be represented by 8 basic units and their combinations [89]–[91]. For example, using $\tilde{\rho} = \tilde{u} = 1$, the physical and lattice scale reference mass and time can be found as,

$$m_{o(PS)} = \frac{\rho}{\tilde{\rho}} x_{0(PS)}^3 \quad (4.30)$$

where,

$$\tilde{\rho} = \rho_{(LS)} \frac{x_{0(LS)}^3}{m_{o(LS)}} \quad (4.31)$$

and

$$t_{o(PS)} = \frac{\tilde{u}}{u} x_{o(PS)} \quad (4.32)$$

where,

$$\tilde{u} = u_{(LS)} \frac{t_{o(LS)}}{x_{o(LS)}} \quad (4.33)$$

Similarly, instead of density (kg/m^3) and mass (kg), concentration (mol/m^3) and amount of substance (mol) can be used. Species transport follows the following LBM algorithm,

If the porous structure is mimicked, as seen in Chapter 6, the surface reactions are resolved via boundary conditions rather than the pore Reynolds number is used where,

$$Re_p = \frac{d_p u_{max}}{\nu} \quad (4.34)$$

and the equivalent spherical diameter of the particle is [92],

$$d_p = \frac{6}{a} \quad (4.35)$$

where the specific surface (a) is assumed to be based on uniform spheres. The physical scale species concentration diffusivity is related to lattice scale by ,

$$\left(\frac{D\Delta t}{\Delta x} \right)_{PS} = \left(\frac{D\Delta t}{\Delta x} \right)_{LS} \quad (4.36)$$

Generally, given that the Re value is known, with lattice kinematic viscosity given by (3.10) where τ is a free parameter. The lattice velocity must be less than 0.17 in the incompressible limit due to the condition that the Mach number should be less than 0.3 [56] . Therefore, there is a choice in selecting the lattice scale kinematic viscosity, velocity, and the number of lattices, barring that the outlined conditions are met.

4.4 The Pseudo-Porous Model

If the velocity is assumed to be constant and not vary temporally, as is the case with this model, evaluating the flow field is unnecessary. It should be noted that this work deals only with steady state conditions. The following LBM model is based on the pseudo-porous approach using effective concentration diffusivity, porosity, and medium conductivity (Millington and Quirk (eq 4.11), Bruggeman (eq 4.13) corrections). Concentration for each species is calculated by,

$$g_{N,i}(x + c_i dt, t + dt) - g_{N,i}(x, t) = -\frac{1}{\tau_g} (g_{N,i} - g_{N,i}^{eq}) + F_{C,N} \quad (4.37)$$

where the equilibrium distribution function for one dimension is ,

$$g_{N,i}^{eq} = w_i C_{N,i} \left\{ 1 + \frac{(c_i \cdot \mathbf{u})}{c_s^2} \right\} \quad (4.38)$$

and for two-dimensional case

$$g_{N,i}^{eq} = w_i C_{N,i} \left\{ 1 + \frac{(c_i \cdot \mathbf{u})}{c_s^2} + \frac{1}{2} \frac{(c_i \cdot \mathbf{u})^2}{c_s^4} - \frac{1}{2} \frac{\mathbf{u}^2}{c_s^2} \right\} \quad (4.39)$$

Note, that each species has its own distribution and equilibrium function (i.e. $g_{N,i}$ and $g_{N,i}^{eq}$) where N is the N-th species. Three-dimensional modelling is outside of the scope of this research and is thus omitted.

The concentration sink/source for one dimension

$$F_{C,N} = \left(1 - \frac{1}{2 \tau_g} \right) w_i \left(\frac{c_i - \mathbf{u}}{c_s^2} \right) R_{lbm,N} f(\varphi)_{lbm} \quad (4.40)$$

and for, and for two-dimensional case

$$F_{C,N} = \left(1 - \frac{1}{2 \tau_g} \right) w_i \left(\frac{c_i - \mathbf{u}}{c_s^2} + \frac{c_i \cdot \mathbf{u}}{c_s^4} c_i \right) R_{lbm,N} f(\varphi)_{lbm} \quad (4.41)$$

The concentration relaxation time constant τ_g , is determined from lattice diffusivity,

$$D_{lbm,N} = \frac{2\tau_g - 1}{6} \quad (4.42)$$

Solid and liquid potential are solved for individually with,

$$h_{s,l_i}(x + c_i dt, t + dt) - h_{s,l_i}(x, t) = -\frac{1}{\tau_h} (h_{s,l_i} - h_{s,l_i}^{eq}) + F_{\varphi_{s,l}} \quad (4.43)$$

and the potential equilibrium distribution function for both lattice models defined as,

$$h_{s,l_i}^{eq} = w_i \varphi_{s,l} \quad (4.44)$$

while the potential source/sink for one dimension

$$F_{\varphi_{s,l}} = \left(1 - \frac{1}{2\tau_h}\right) w_i \left(\frac{\mathbf{c}_i - \mathbf{u}}{c_s^2}\right) K_{lbm_{s,l}} \quad (4.45)$$

and for and for two-dimensional case,

$$F_{\varphi_{s,l}} = \left(1 - \frac{1}{2\tau_h}\right) w_i \left(\frac{\mathbf{c}_i - \mathbf{u}}{c_s^2} + \frac{\mathbf{c}_i \cdot \mathbf{u}}{c_s^4} \mathbf{c}_i\right) K_{lbm_{s,l}} \quad (4.46)$$

The potential relaxation time constant τ_h , is related to lattice conductivity of each phase,

$$\sigma_{lbm_{s,l}} = \frac{2\tau_h - 1}{6} \quad (4.47)$$

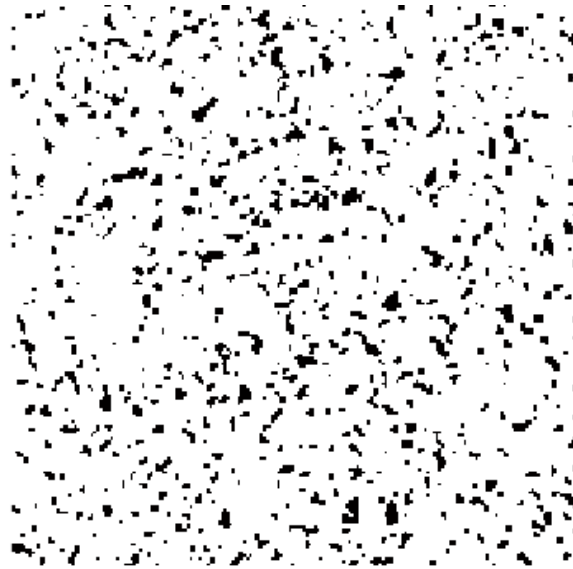
4.5 The Physical Porous Geometry Model

The previous section dealt with the pseudo-porous model involving the continuum approach and LBM where transport and interfacial reactions within porous media were based on spatial averages and parameter corrections. The following aims to mimic a two-dimensional porous anode and investigate the pore-scale process involving surface kinetics under the aqueous condition and dilute solution.

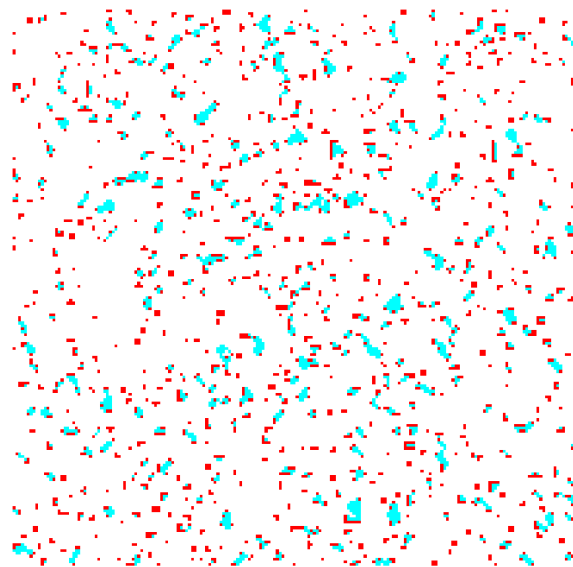
The attractiveness of LBM in its application toward pore-scale modelling involving transport phenomena and reactive flows is highlighted by a variety of published material [93]–[97]. Investigating systems involving porous media is a complicated endeavour as the problems involve various scales, processes, hydrological variations, and morphological dependencies. The ability of LBM to describe nonequilibrium dynamics makes it particularly fitting for situations concerning surface reactions and complex boundaries. A number of methodologies have been developed for heterogeneous reactions such as augmented bounce back scheme [98], varying solid and liquid resistances [99], and treatment of interfaces as part of bulk dynamics with flux correction during collision [100]. As will be seen in the this section, the LBM model builds upon the previously developed by utilizing a randomly distributed homogeneous matrix where surface reactions are included via boundary conditions, The effect of the Reynolds number and porosity are investigated.

The porous region, shown in Figure 12a, is broken down into active and non-active boundaries as shown in Figure 12b. The active boundaries are imposed based on the node configurations shown in Figure 13, meanwhile the non-active boundaries are treated with the bounce-back scheme. The active node configurations were selected such that only three distribution functions are unknown

and have the same mathematical relationship for species concentration as given by equation 4.51. The porous region is generated randomly having Gaussian distribution.

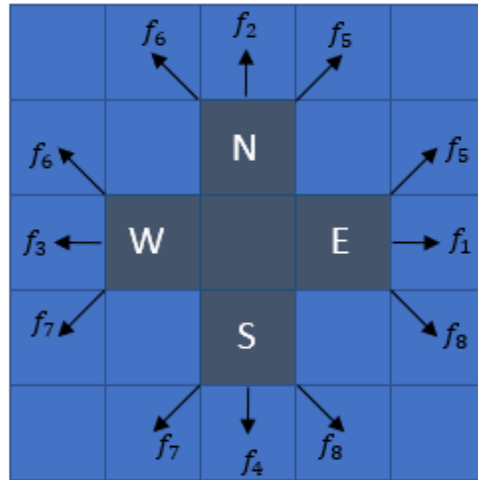


(a)



(b)

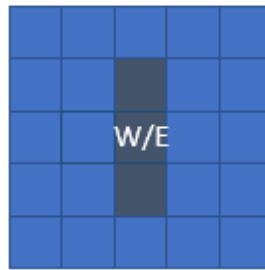
Figure 9: Porous Region (a) Total (b) Active-Red and Inactive-Cyan



(a)



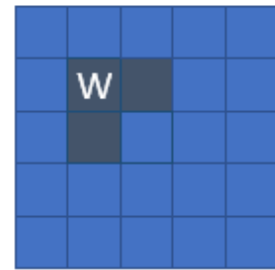
(b)



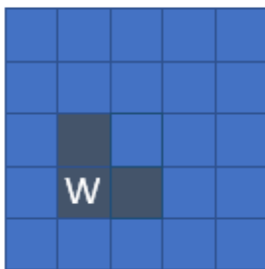
(c)



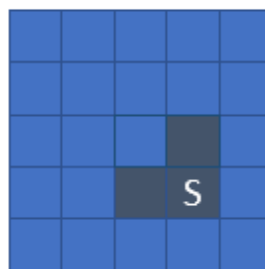
(d)



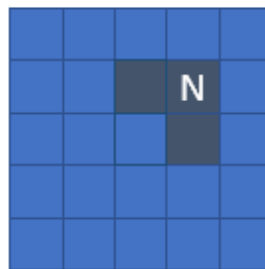
(e)



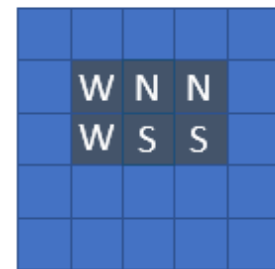
(f)



(g)



(h)



(i)

Figure 10: Active Boundary Nodes Configuration

The collision operator used for concentration is [101]

$$g_{N,i}(x + c_i dt, t + dt) - g_{N,i}(x, t) = -\frac{1}{(\tau_{g,i} + 0.5)}(g_{N,i} - g_{N,i}^{eq}) \quad (4.48)$$

The 0.5 comes from the discretization procedure. The surface reaction is now modeled using the nonequilibrium portion of the distribution function for the boundary [93]. Taking the North boundary for example as seen in Figure 11,

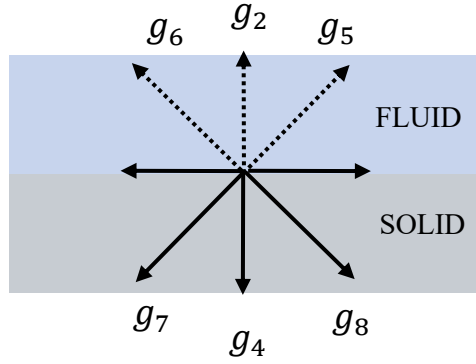


Figure 11: North Boundary Distribution Functions

Since

$$g_2 + g_4 = g_2^{eq} + g_2^{neq} + g_4^{eq} + g_4^{neq} = g_2^{eq} + g_4^{eq} \quad (4.49)$$

the unknown distribution functions can be found by,

$$\begin{aligned} g_2 &= g_2^{eq} + g_4^{eq} - g_4 \\ g_5 &= g_5^{eq} + g_7^{eq} - g_7 \\ g_6 &= g_6^{eq} + g_8^{eq} - g_8 \end{aligned} \quad (4.50)$$

and the species concentration as,

$$C_i = 6(g_4 + g_7 + g_8) - 3\left(1 + \frac{1}{2\tau_g}\right)R_{lbm,i} f(\varphi)_{lbm} \quad (4.51)$$

where,

$$R_{lbm,i} = \frac{si_0}{nF} \quad (4.52)$$

and,

$$f(\varphi)_{lbm} = \frac{i_n}{i_o} = \frac{\left[\frac{C_R}{C^\circ} \exp(\alpha_a f \eta_{in}) - \frac{C_O}{C^\circ} \exp(-\alpha_c f \eta_{in}) \right]}{1 + \frac{i_o}{i_{lim}} \left[\frac{C_R}{C^\circ} \exp(\alpha_a f \eta_{in}) + \frac{C_O}{C^\circ} \exp(\alpha_c f \eta_{in}) \right]} \quad (4.53)$$

4.6 Summary

The mathematical model for electrochemically reactive flow was developed in this chapter. The dimensional analysis of the continuity equation was performed. Utilizing the derived dimensionless parameters, the relationship of the surface kinetics between the physical and the lattice scales was established. The LBM algorithm for the pseudo and physical flow-through porous electrodes was developed.

Chapter 5

Code Validation and Benchmark Solutions

5.1 Introduction

The following sections are focused on utilizing applicable LBM problems for code validation, identification of the variety of components and their relevance, as well as transition to electrochemistry in the developed pseudo and physical porosity models. As discussed in section 2.3, advection and diffusion are the ion transport modes considered in this research. In order to validate the developed code for the models each mode was solved separately through the following examples of heat conduction in a rectangular plate for diffusion and fully developed flow channel advection. Ultimately, the objective is to model a dilute solution flowing through a porous medium while undergoing electrochemical changes via redox surface reactions. With a focus on porosity, an obstacle is added to the advection in a channel problem seen in section 5.3. Addition of an obstacle provides a pathway to mimicking the physical porous structure as it is nothing other than a zone with many obstacles and channels, see section 5.2. For the purpose of ion advection, heat transfer is added in section 5.4, wherewith the addition of a separate probability distribution function for temperature is analogous to species transport, as seen in section 5.5.

5.2 Heat Conduction in a Rectangular Plate

Steady state 2-D heat diffusion in a rectangular fin is investigated in this section. The fin ($k=10\text{W m}^{-1}\text{K}^{-1}$), presented in Figure 12, has length $L = 8\text{ mm}$ and width $w = 4\text{ mm}$ with $T_w = 45^\circ\text{C}$, $T_\infty = 25^\circ\text{C}$ and $h = 600\text{W m}^{-2}\text{K}^{-1}$.

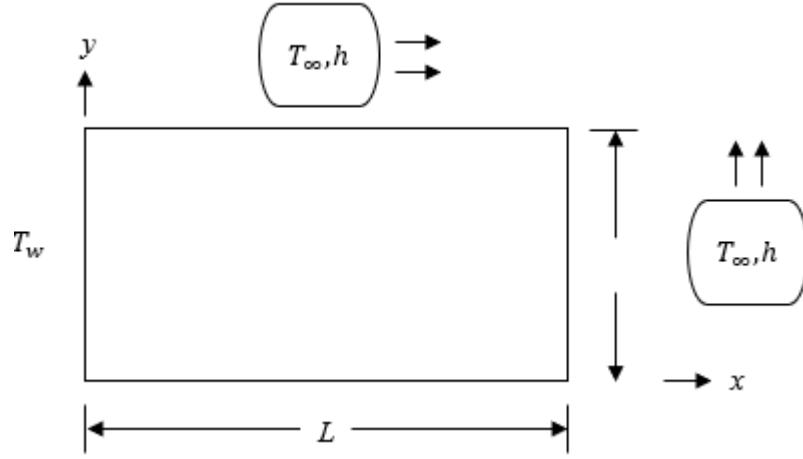


Figure 12: Heat Conduction Fin Geometry Using D_2Q_9 lattice model, the temperature distribution can be determined as follows,

$$f_i(x, y) = f_i(x, y)[1 - \omega] + \omega f_i^{eq}(x, y) \quad (5.1)$$

where the relationship between lattice thermal diffusivity and the relaxation parameter is,

$$\alpha = \frac{2\tau - 1}{6} \quad (5.2)$$

The equilibrium distribution function f_i^{eq} for thermal diffusion is,

$$f_i^{eq} = w_i \theta(x, y) \quad (5.3)$$

and the temperature is evaluated as,

$$\theta(x, y) = \sum_{i=0}^8 f_i(x, y) \quad (5.4)$$

where θ is the non-dimensional temperature and is calculated as follows,

$$\theta = \frac{T - T_{\infty}}{T_w - T_{\infty}} \quad (5.5)$$

The temperature on the west boundary is constant, with unknown distribution functions are f_5 , f_1 and f_8 , Figure 13, and can be found as previously mentioned constant BC,

$$f_i = T_w(w_i + w_{i+2}) - f_{i+2} \quad (5.6)$$

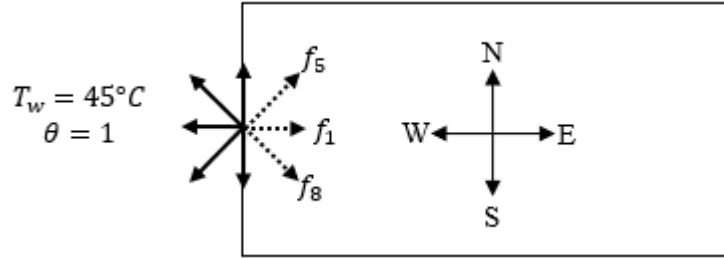


Figure 13: Constant Temperature Boundary

The other three sides of the domain, involving convective heat transfer where,

$$-k \partial_y T = -k \partial_x T = h(T - T_{\infty}) \quad (5.7)$$

having non-dimensional form,

$$\partial_y \theta = \partial_x \theta = Bi \quad (5.8)$$

Where Bi is the Biot number, which is a dimensionless number that relates the convective heat transfer coefficient h and the thermal conductivity of the body k , such that,

$$Bi = \frac{h\Delta y}{k} \quad (5.9)$$

The functionality of LBM, following a generic algorithm as shown in Figure 14,

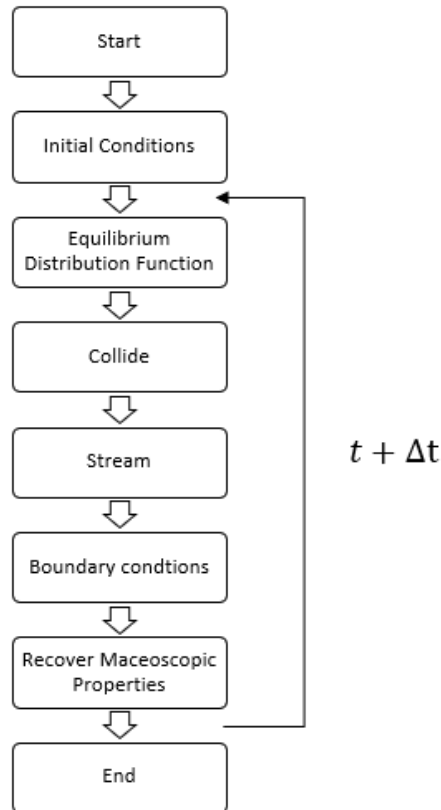


Figure 14: LBM Algorithm

Based on the outlined conditions, fin heat diffusion is shown in Figures 15 and 16. Diffusion transport is shown with the vertical temperature profile, seen in Figure 16, gets increasingly narrow, while temperature decreases downstream of the fin.

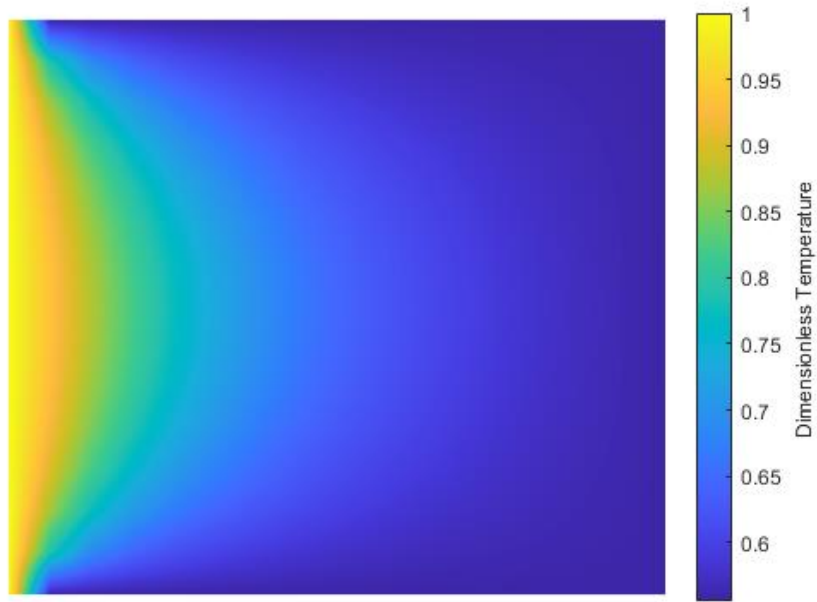


Figure 15: Fin Dimensionless Temperature Contour

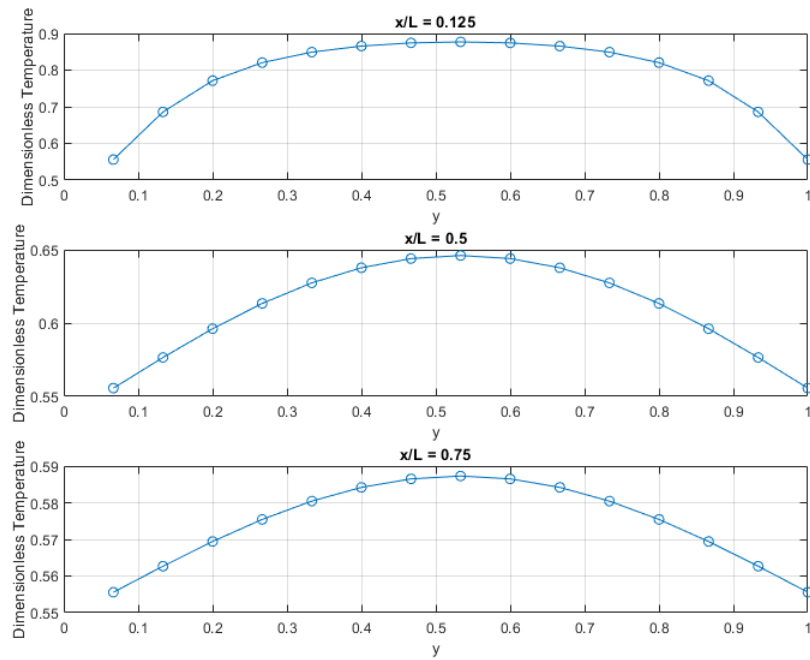


Figure 16: Fin Vertical Dimensionless Temperature Profile

5.3 Fully Developed Flow, Advection in a Channel

Advection in a channel under fully developed (Poiseuille) laminar flow regime with uniform inlet velocity, shown in Figure 17, is simulated.

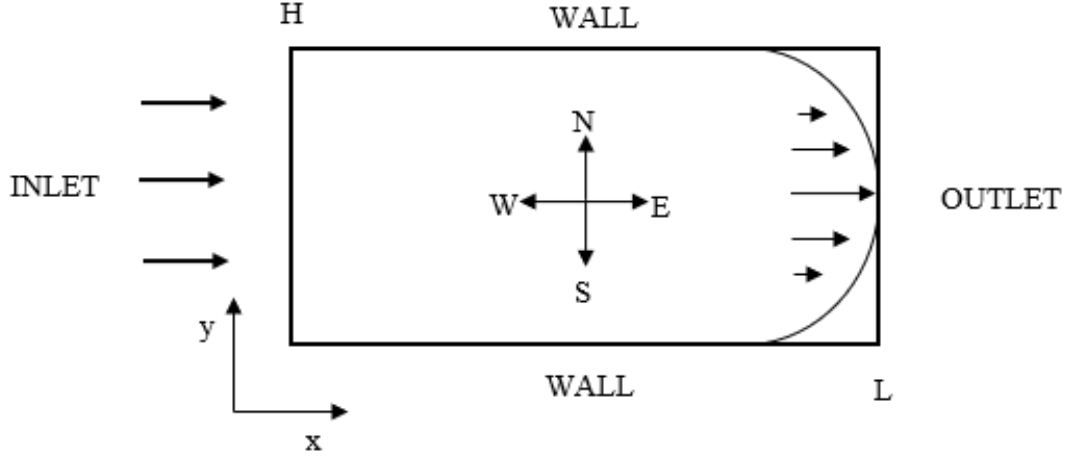


Figure 17: Fully Developed Flow, Advection in a Channel

With density and viscosity $\rho_{ls} = 1, \nu_{ls} = 0.05$, respectively. Where lattice viscosity is given as,

$$\nu = \frac{2\tau - 1}{6} \quad (5.10)$$

The velocity inlet (W) with $u_{ls} = 0.1$, bounce back (N,S) and zero-gradient (E) BC's are applied.

The flow development throughout the channel can be seen in Figure 18, where u/u_{ave} is the ratio of dimensionless velocity and the cross section of the fully developed flow,

$$u_{ave} = \frac{2}{3} u_{max} \quad (5.11)$$

and u_{max} is taken to be the maximum velocity at the channel outlet. The dimensionless cross-sectional position Y/H , is the position Y normalized by the channel height H .

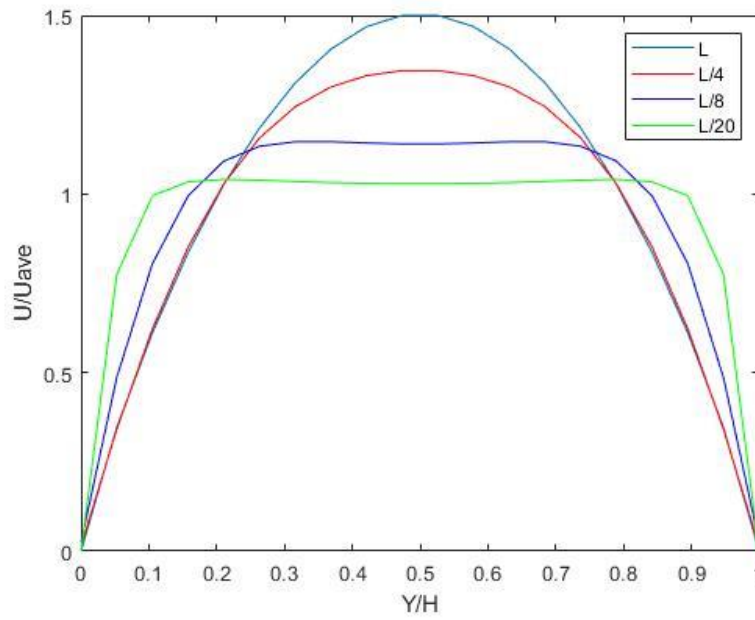


Figure 18: Radial Velocity Profile Along Different Sections of the Channel

The fully developed region is shown to agree with the analytical solution in Figure 19 [55].

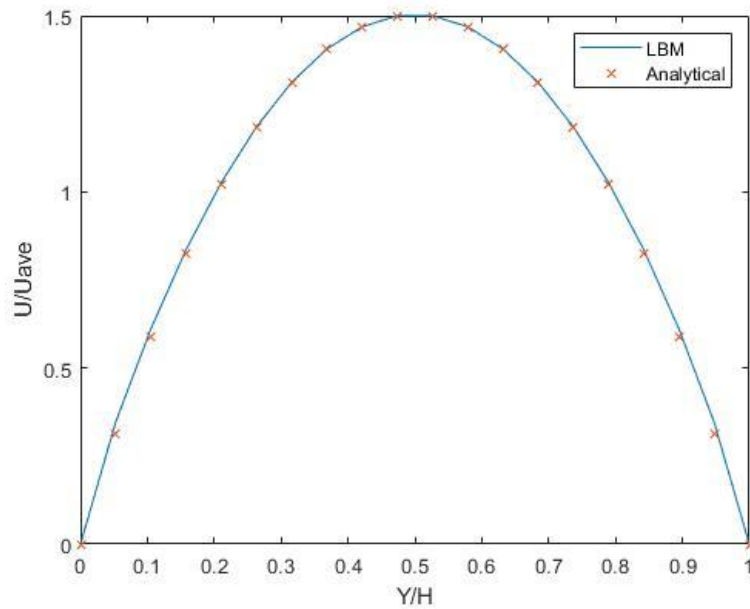


Figure 19: Fully Developed Flow, Advection in a Channel LBM Results vs Analytical

5.4 Effect of an Obstacle on Heat Transfer in a Channel

The flow around an obstacle with heat transfer, Figures 20 and 21, was selected for code validation involving the physical porous geometry given in Chapter 4. The structure, as seen in section 4.5 Figure 9a, is a combination of channels and obstacles.

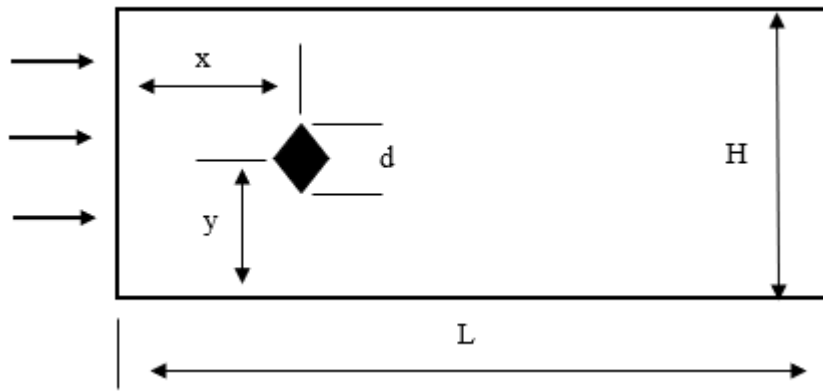


Figure 20: Flow around Obstacle in a channel Domain

The addition of another distribution functions is illustrated with an addition of temperature advection, as seen in Figure 23.

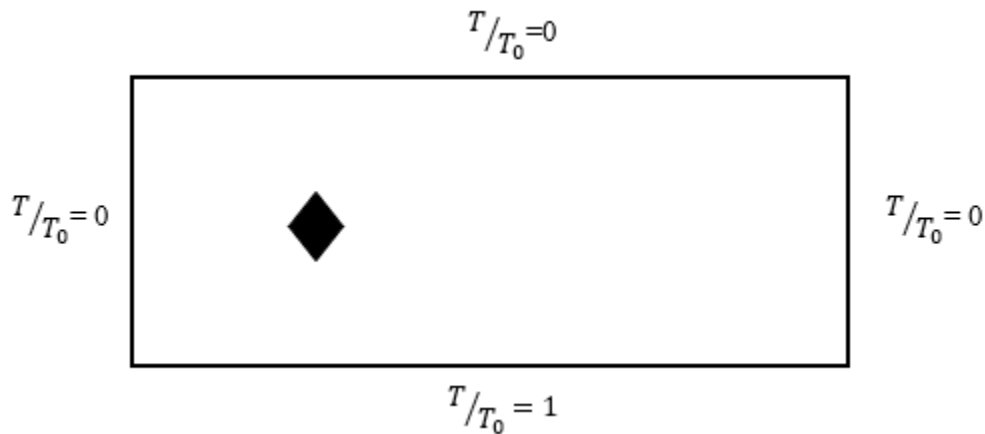


Figure 21: Flow Around an Obstacle in a Channel with Heat Transfer

The temperature equilibrium distribution function is,

$$g_i^{eq} = w_i T \left\{ 1 + \frac{(c_i \cdot \mathbf{u})}{c_s^2} + \frac{1}{2} \frac{(c_i \cdot \mathbf{u})^2}{c_s^4} - \frac{1}{2} \frac{\mathbf{u}^2}{c_s^2} \right\} \quad (5.13)$$

The $Pr=0.71$ where,

$$Pr = \frac{\nu}{\xi} \quad (5.14)$$

with thermal diffusivity ξ being,

$$\xi = \frac{2\tau_g - 1}{6} \quad (5.15)$$

Thus, given Pr and lattice kinematic viscosity, lattice thermal diffusivity and τ_g can be determined accordingly. Constant advection BC is applied to all sides.

Simulations are performed based on $Re=50,100, 150, 200$ characteristic blockage ratios $H/d = 4$, $x/H = 2$, and $y/H = 0.375, 0.625$. The bounce back BC is used for obstacle walls. Lattice scale velocity is set to 0.1, then viscosity is calculated from the Reynolds number and τ from viscosity according to (3.10). The velocity profiles due to varying Re and obstacle location can be seen in Figures 21 and 22, respectively. With the increase of Re the obstacle effect on the flow becomes increasingly appreciable. Furthermore, the obstacle location with $y/H = 0.375$ and 0.625 is seen to have symmetric velocity profiles.

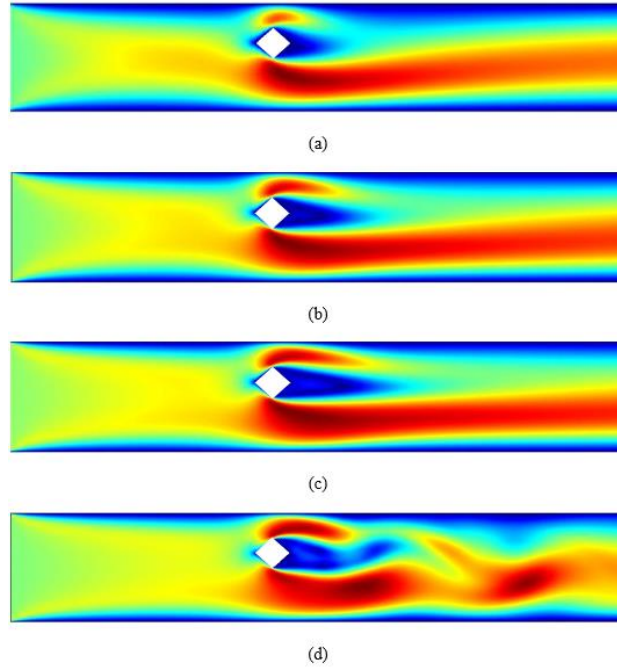


Figure 22: Flow Around an Obstacle Velocity Magnitude Contour, $y/H=0.625$, a) $Re=50$, b) $Re=100$, c) $Re=150$, d) $Re=200$

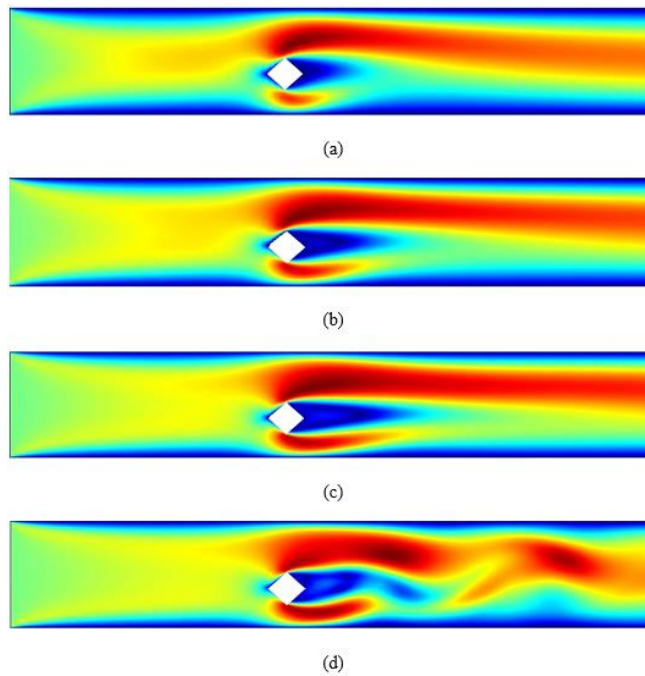


Figure 23: Flow Around an Obstacle Velocity Magnitude Contour, $y/H=0.375$, a) $Re=50$, b) $Re=100$, c) $Re=150$, d) $Re=200$

As seen in Figures 24 and 25, the effect of Re on the temperature profile, when the obstacle is closer the hotter wall, has a greater effect on the heat distribution as opposed to when the obstacle is further away.

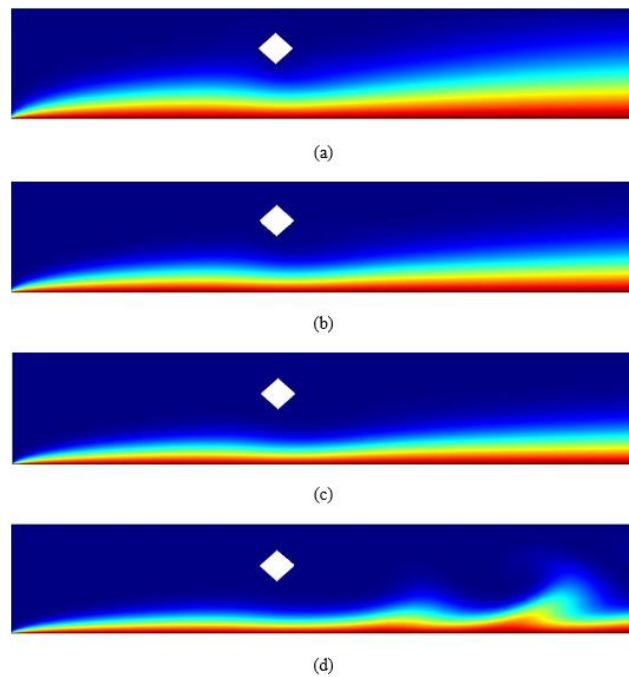


Figure 24: Temperature Contour, $y/H=0.625$, a) $Re=50$, b) $Re=100$, c) $Re=150$, d) $Re=200$

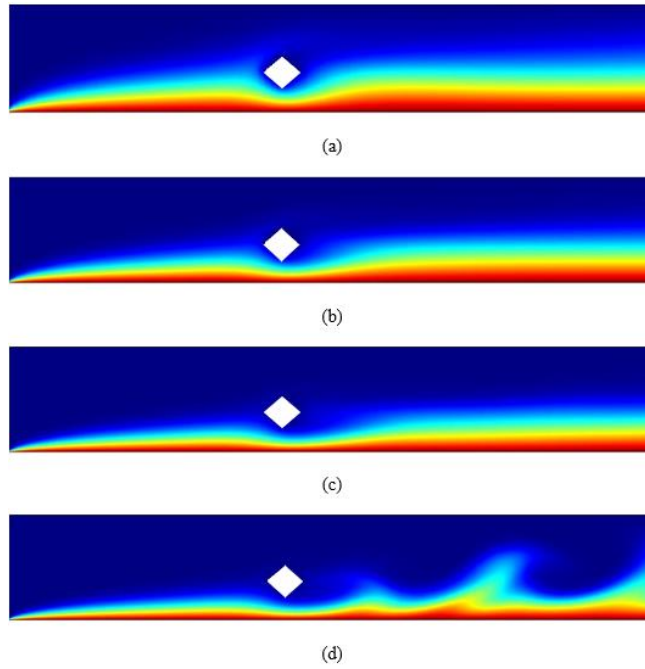


Figure 25: Temperature Contour, $y/H=0.375$, a) $Re=50$, b) $Re=100$, c) $Re=150$, d) $Re=200$

5.5 Advection and Diffusion in a Channel with Species Transport

In this section, an advection diffusion problem involving species transport, which has an analytical -Leveque solution, is solved using the developed code [102] [103]. The domain, with entrance velocity having a parabolic profile, is shown in Figure 26 below.

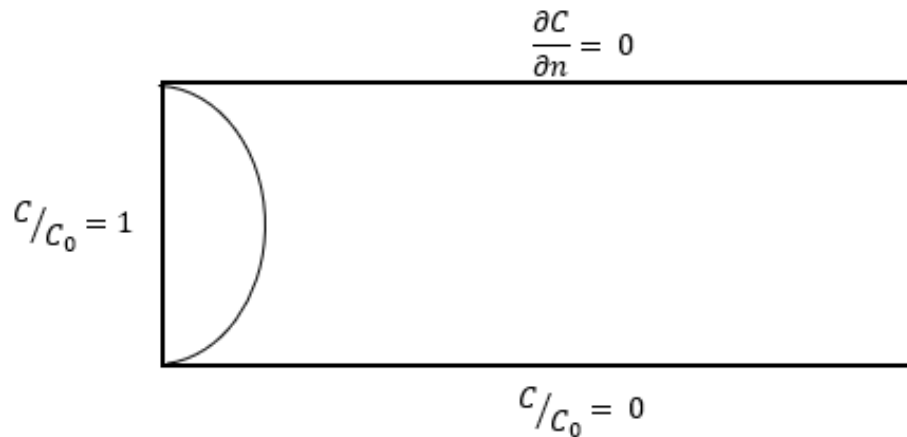


Figure 26: Species Concentration Advection and Diffusion in a Channel

The simulation results for species flux across the bottom surface show good agreement with the analytical solution as seen in Figure 27. The species flux is seen to be the highest at the inlet with a rapid decrease followed by an eventual plateau.

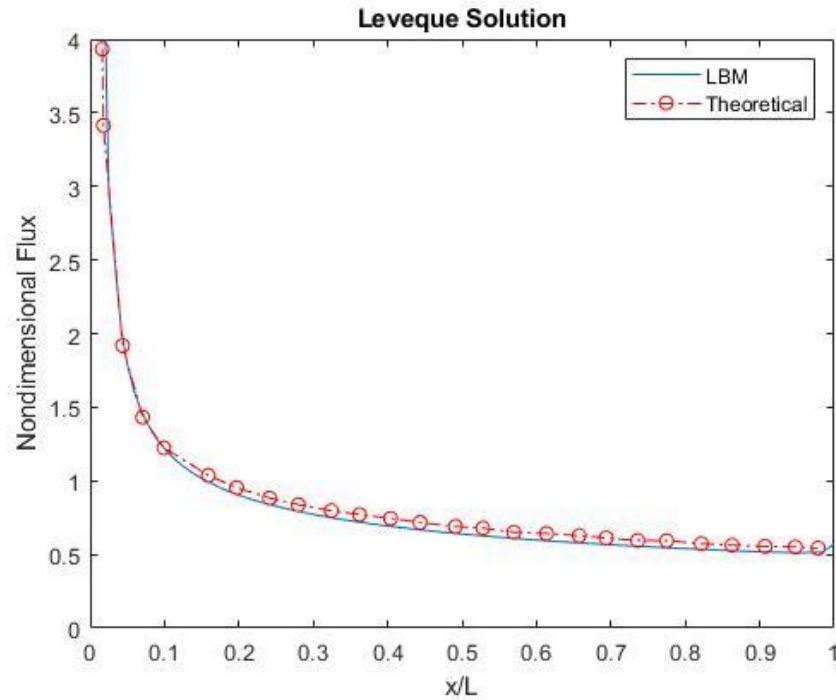


Figure 27: LBM Species Flux at the Bottom Surface vs Analytical Solution[104]

5.6 Summary

A set of problems were solved in this chapter. Section 5.2 outlined the rudimentary LBM algorithm implementation through a scalar thermal diffusion example. Section 5.3 involved the addition of fluid flow in a simple channel followed by obstacle inclusion in section 5.4. Fluid flow around the obstacle was used for code validation with the purpose of transition to flow within a porous structure. Furthermore, temperature addition served as a gateway to using multiple probability distribution functions leading to species transport shown in section 5.5. The aforementioned processes served as the building blocks for the study of surface reactions as discussed in the next chapter.

Chapter 6

Results and Discussion

6.1 Introduction

The sections in this chapter discuss the numerical investigation, using the pseudo approach, of a one-dimensional anode and the single cell reactor, outlined in Chapter 4. The relationship between current, potential and the concentrations of the iodide/iodine couple was studied. Following, a set of two-dimensional simulations, in a physical flow-through porous anode, were performed with $0.1 \leq Re \leq 5$ and porosity $\lambda = 0.9$. Low Reynolds values were selected instead of the residence time being one of the key components in attaining favorable reaction kinetics and current densities [105]. Reynolds values exceeding 10 were not investigated since they would require inertial-effects consideration, which is outside of the scope of this work [106]. As previously alluded to, the increased surface area is an attractive feature of the porous electrode as it allows for more reactions sites but can be hindered by slow reaction kinetics. The reaction kinetics are influenced by several processes such as mass transfer, surface adhesion, double layer capacitance, pressure, crystallization, and flow, particularly in electrochemical systems aimed at water treatment. Besides an applied potential necessary to drive a redox couple such as Iodide/Iodine, in the required direction, the flow regime needs to be considered since reduced contact time with the surface can limit the treatment systems performance. While several additional factors can be of influence,

based on the developed model, the forthcoming sections aims to investigate the relationship between flow and the surface kinetics of iodine in the ppm range.

One of the other factors that can influence the reaction process is the surface treatment and can be achieved with varying methods, such as heat and electrochemical treatment. Electrochemical treatment, where a potential is applied across the electrode, has been reported to result in a 256 % current density improvement in a carbon felt electrode [105]. The applied potential led to the formation of micro-cavities on the felt surface. By creating more voids, the application of the potential has made the carbon felt more porous. The second set of simulations was directed at exploring the effect of varying porosity on iodide oxidation in a flow-through porous electrode. The commercially available carbon felt electrodes vary in porosity but can typically be found in the 0.9 range [107]. With $Re=1$, the porosity is varied with $\lambda= 0.8$ and 0.7 .

Determining the solid and liquid phase potential distribution, within a porous electrode, is a very challenging endeavour. Experimentally, having the same applied potential can yield varying potentials (electric potential) against the reference electrode, depending on the electrode size and flow conditions, to name a few. For the purpose of this study, the electric potential distributions of the solid and liquid phase were imposed, using the results obtained with the pseudo-porous approach, having only axial variation as seen in Figure 28. Utilizing two-dimensional porous geometry with five probability distribution functions corresponding to flow, concentration of two species, solid and liquid potentials increase the computational cost considerably compared to the pseudo-porous model and is outside of the scope of this work.

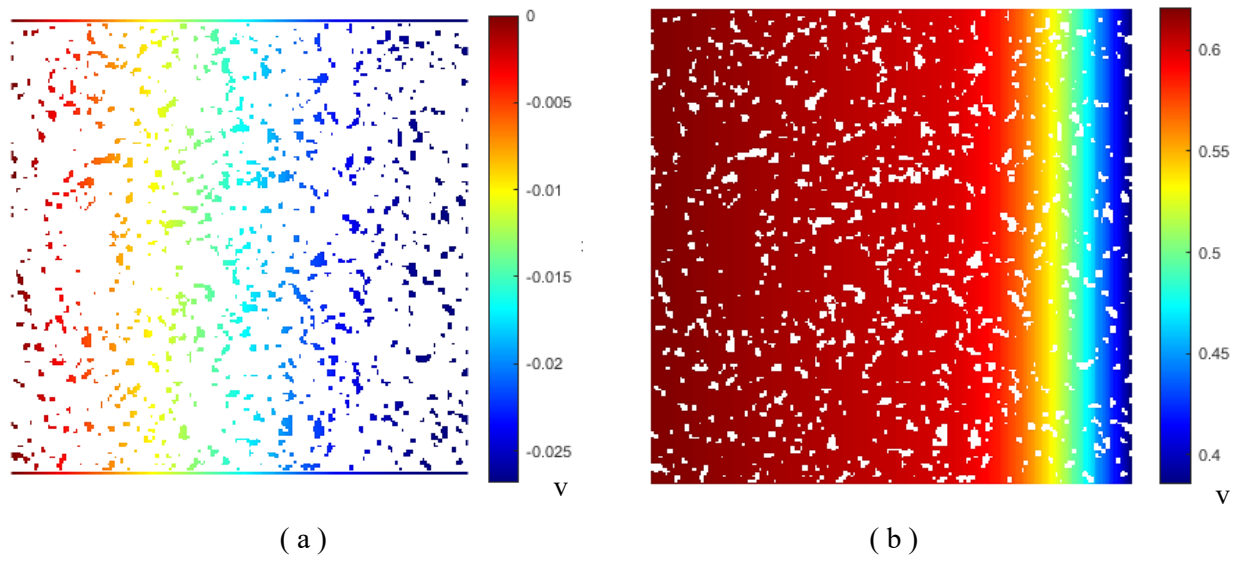


Figure 28: Phase Potential Distribution Results Imposed from the Pseudo Porous Model (a) Solid, (b) Electrolyte

6.2 Pseudo-Porous Anode

The one-dimensional model of iodide oxidation, using $D_1 Q_3$, was first tested on only the anode as shown in Figure 29. The simulation parameters are given in Table 1. The reaction kinetics were assumed to be concentration independent (Butler-Volmer, equation (2.25)), with constant equilibrium potential.

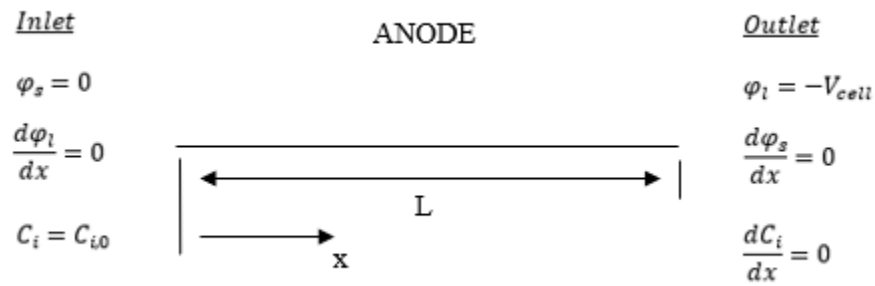


Figure 29: Domain Schematic of a One-dimensional Porous Anode

Table 1: Simulation Parameters for the Pseudo and Physical Models

Parameter	Value (units)	Reference
D_{I^-}	1.8e-09 (m ² s ⁻¹)	[108]
D_{I_2}	1.4e-09 (m ² s ⁻¹)	[109]
σ_l	1e-03 (S m ⁻¹)	[110]
σ_s	10 (S m ⁻¹)	[111]
σ_{SEP}	1e-05 (S m ⁻¹)	[112]
L	0.03 (m)	
u	0.005 (m s ⁻¹)	
$C_{I^-,0}$	0.01 (mol m ⁻³)	
$C_{I_2,0}$	0 (mol m ⁻³)	
E_{eq}	-0.621 (V)	
i_0	0.0057 (A m ⁻²)	
α_a, α_c	0.5	
i_{lim}	0.7(C_{I^-}) (A m ⁻²)	
V_{cell}	-0.38 (V)	
τ_{I,I^-}	0.52	
$\tau_{s,l}$	0.6	
$\tau_{l,SEP}$	0.53	

The results obtained with the developed LBM model (Figure 30-35) are in excellent agreement with FEM. Figures 30 and 31 show results in concentration units (cu) while Figures 32 exemplifies the corresponding physical values. The iodide concentration is seen to decrease rapidly near the end of the anode corresponding to iodine production. This can be attributed to the exponential relationship between concentration and overpotential as seen in the BV equation.

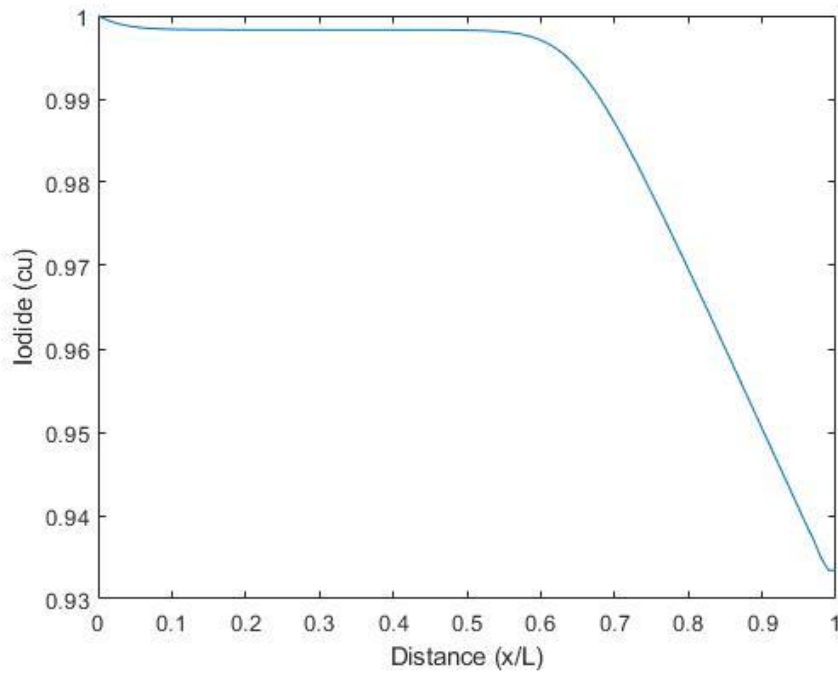


Figure 30: Iodide Concentration LBM

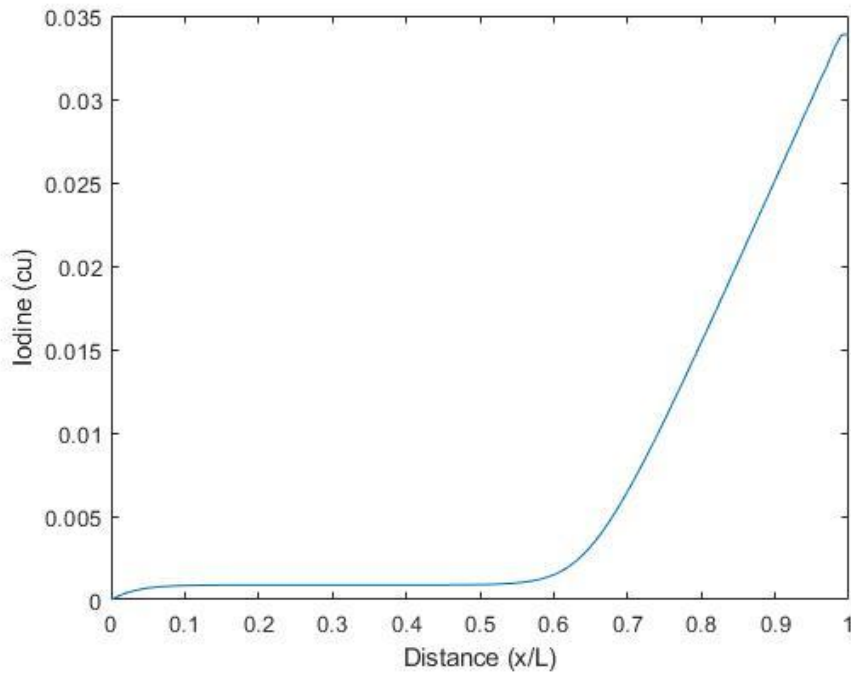


Figure 31: Iodine Concentration LBM

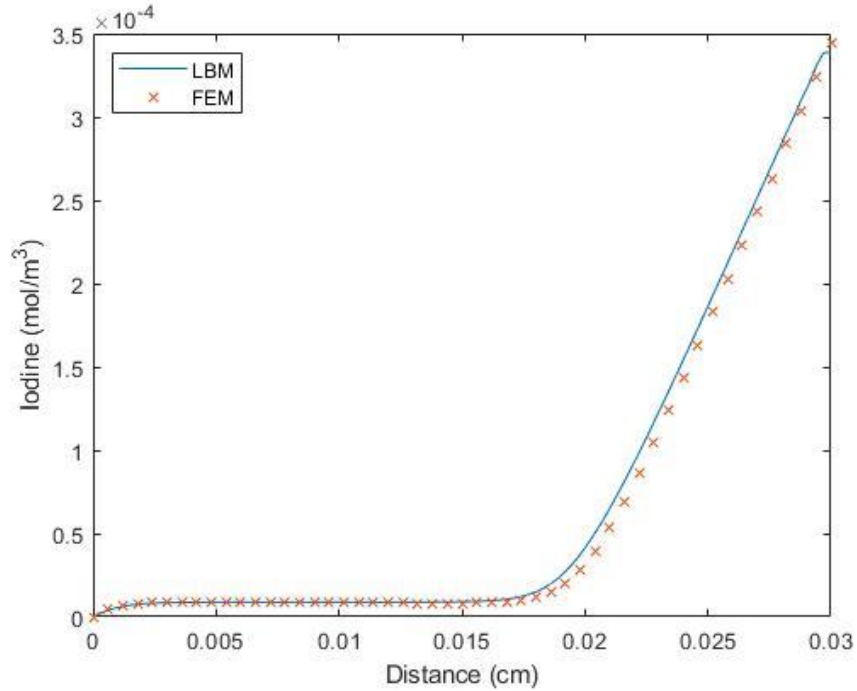


Figure 32: Iodine Concentration LBM vs FEM (scaled)

The solid phase potential is much lower than in the liquid phase as seen in Figures 33 and 34, respectively. Furthermore, the rapid decrease in the liquid phase potential, near the end of the anode and small gradient in the solid phase result in higher overpotential. Higher overpotentials correspond to higher current densities, increased reaction rates and facilitate iodide consumption and corresponding iodine production.

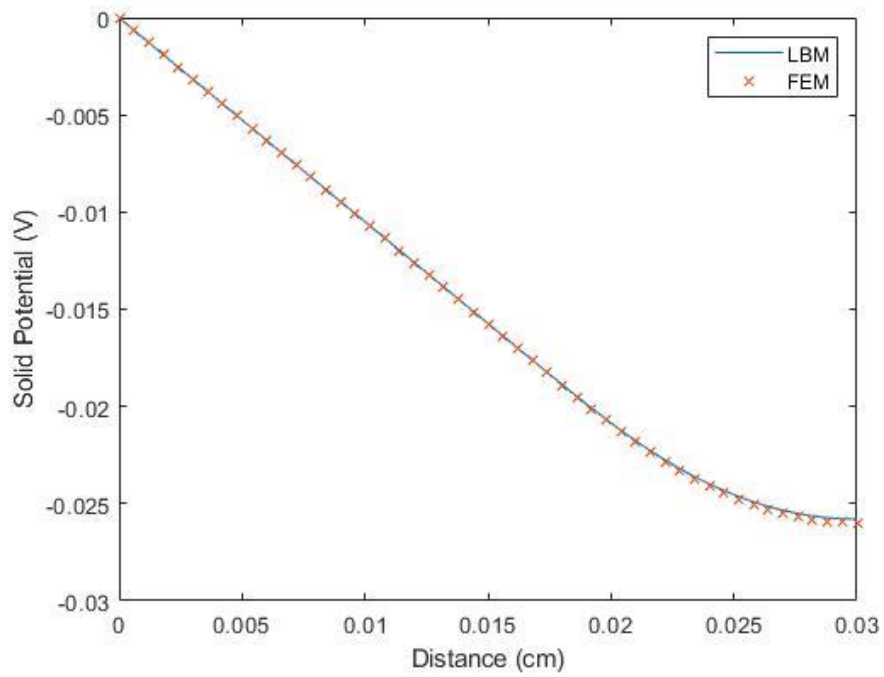


Figure 33: Solid Potential LBM vs FEM

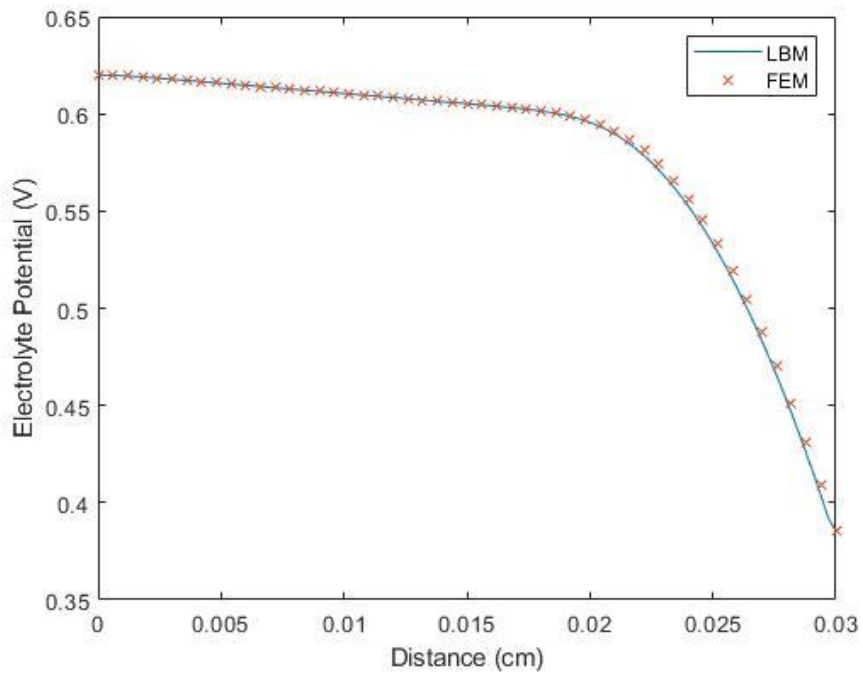


Figure 34: Electrolyte Potential LBM vs FEM

The solid and liquid current density are determined using Ohm's law via the resolved potentials given in Figures 33 and 34. As seen in Figure 35, symmetry is observed where current leaving the solid phase is picked up by the liquid phase.

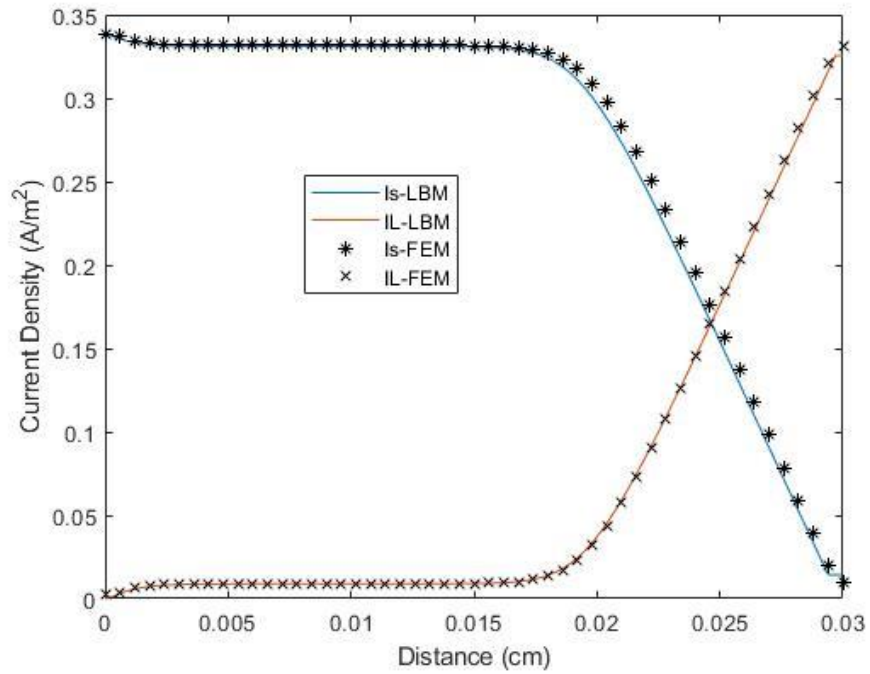


Figure 35: Pseudo Porous Anode Solid and Electrolyte Current Density LBM vs FEM

6.3 Single Cell Reactor

The single cell reactor, Figure 36, was simulated with $V_{cell} = 1.5$ (V), concentration dependent kinetics as shown in section 4.4, and constant equilibrium potential. The solid separator potential was treated as a potential drop between the anode and cathode boundaries, the same can be done for the liquid potential. In this work the liquid potential in the separator was solved for by varying the relaxation time due to different conductivity. Since the cathode and anode are of different length scales the potential force terms in the cathode were scaled via the scaling factor found to be,

$$s'' = \frac{L_{cathode}^2}{L_{anode}^2} \quad (6.1)$$

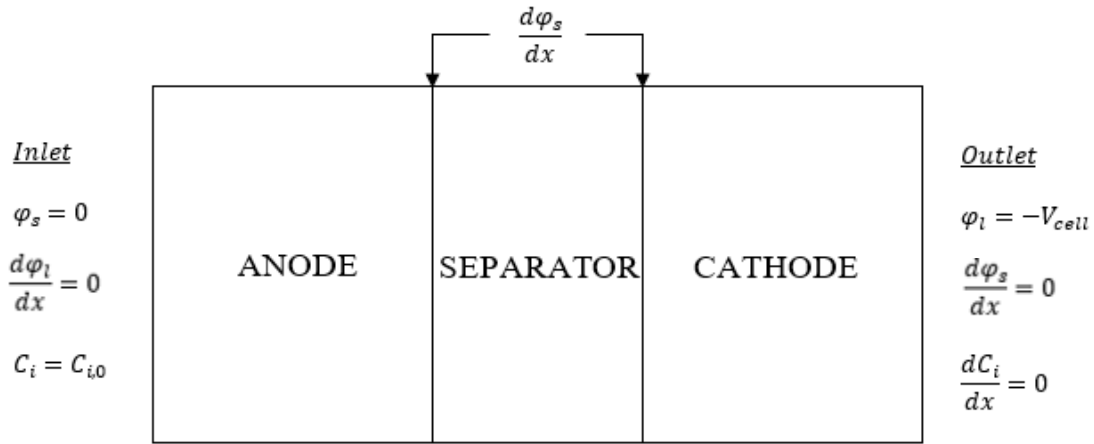


Figure 36: Schematic Representation of a Disinfection Cell with Flow-Through Porous Electrodes

The porous anode and cathode electrodes in the reactor were carbon felt with an assumed effective specific surface area of $5000 \text{ m}^2 \text{ m}^{-3}$ and porosity of 0.9. The separator was glass-wool with

assumed specific surface area of $500 \text{ m}^2 \text{ m}^{-3}$. The anode, cathode, and separator thickness were each respectively set as 3, 1.5 cm, and 0.5 cm based on the cell dimensions found in [23].

Note that the length scale used for the potential relaxation times is the anode length, if τ is to be based off the cathode length the inverse of equation (6.1) would be used for the potential force terms in the anode. The length scale for concentration is the full reactor domain meaning that the reaction rate scales are not required. Since the electrolyte (west) and solid (east) potentials are not initially known, the dimensionless potential can also be expressed as

$$\tilde{\varphi} = \frac{\varphi}{\Delta\varphi} \quad (6.2)$$

where $\Delta\varphi$ is continuously adjusted based on the changing boundary potentials after each iteration. Figures 37-40 show good agreement between the scaled LBM results and FEM. The concentration profiles of I^- and I_2 through the reactor are seen in figures 37 and 38, respectively. Iodide shows a decreasing trend in the anode due to oxidation to I_2 . The decrease corresponds to majority of the surface reactions occurring closer to the tail end of the anode, which has been alluded to in [23]. For electrochemical flow reactors employing spacers between the anode and cathode, the interelectrode distance is key in optimizing and describing the electrochemical reaction [113]. Reduced gaps have been observed to lower cell resistance, requiring reduced amounts of supporting electrolyte [114]. The iodide consumption closer to the outlet can yield improved cell performance with more efficient synthesis and charge transfer between the electrodes.

Iodine reduction is observed until the midpoint of the electrode followed by oxidation corresponding to iodide reduction. The electrode in this case is then seen to operate in both the

cathodic and the anodic modes. The increasing trend of iodine downstream is likely due to the lower reduction rate leading to a net positive effect for the iodine production as per the Butler-Volmer equation previously discussed. The low conductivity of the spacer hinders the Faradic current, arising from the surface potential between the solid and the electrolyte. As shown in Figures 37 and 38, both species concentrations remain constant throughout the spacer.

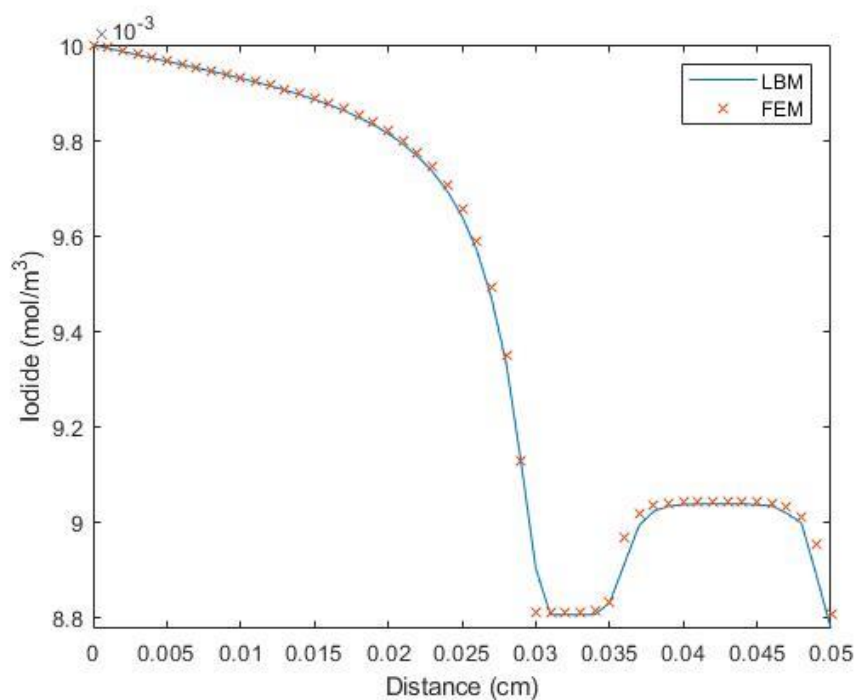


Figure 37: Single Cell Reactor Iodide Concentration LBM vs FEM

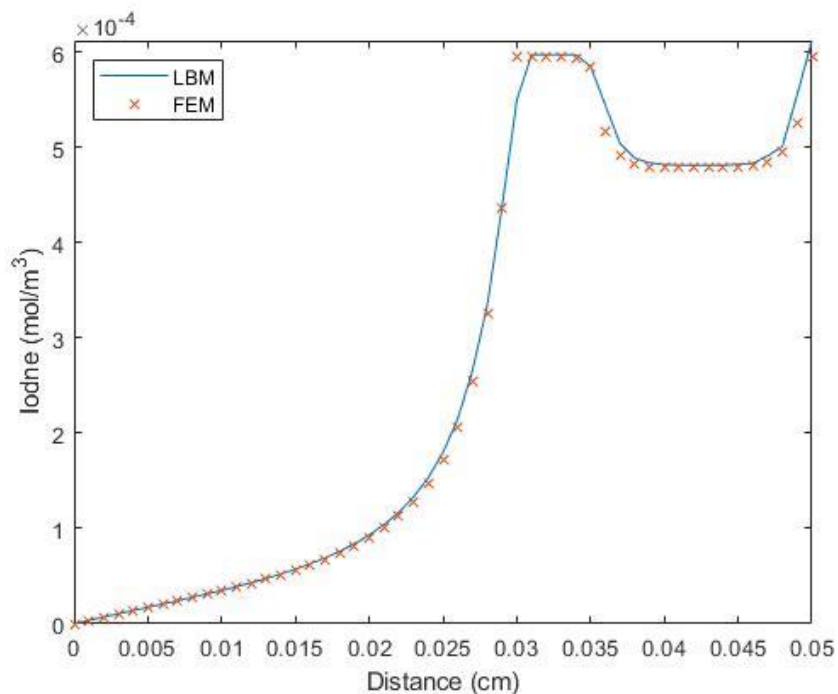


Figure 38: Single Cell Reactor Iodine Concentration LBM vs FEM

A cell potential of 1.5 Volts against the standard hydrogen electrode (SHE) is applied with the graphite and solution potential distributions shown in Figures 39 and 40, respectively. Reference electrodes are utilized in a three-electrode system found in electrochemical techniques such as cyclic voltammetry, used to determine redox response to potential sweep, along with the working and the counted electrodes. The working electrode is the one being observed while the counter electrode is inert and only serves to allow current flow. The redox potential is then measured against a reference electrode such as the SHE which has well known electrode potential. The solid phase potential gradient is almost zero at both the anode and cathode, however due to the low conductivity of the glass wool, a large potential drop is observed. Similar to Figure 35 found in the previous section, symmetry is observed between the potential profiles of the phases. The current leaving the solid phase must enter the liquid phase and vice versa.

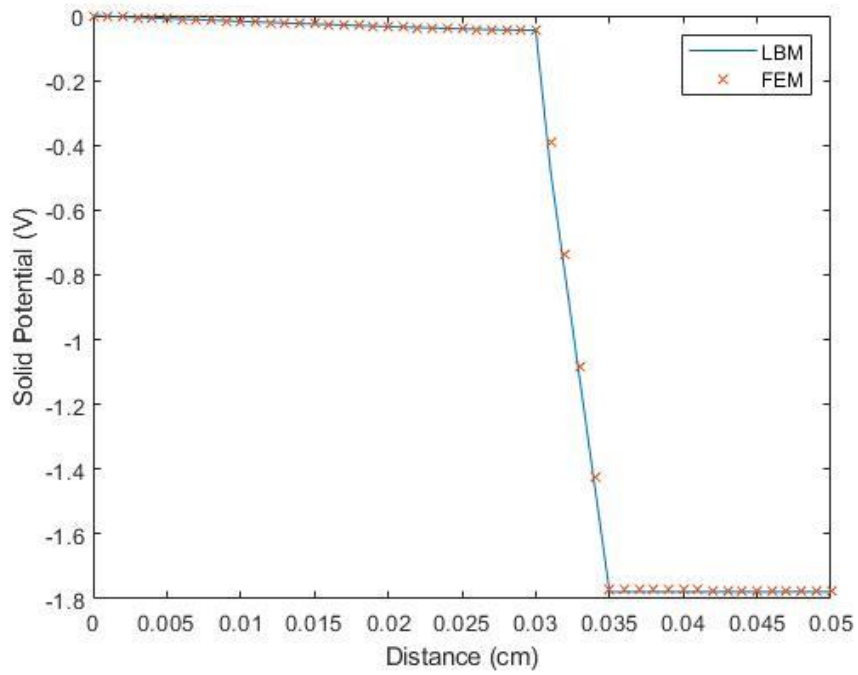


Figure 39: Single Cell Reactor Solid Potential

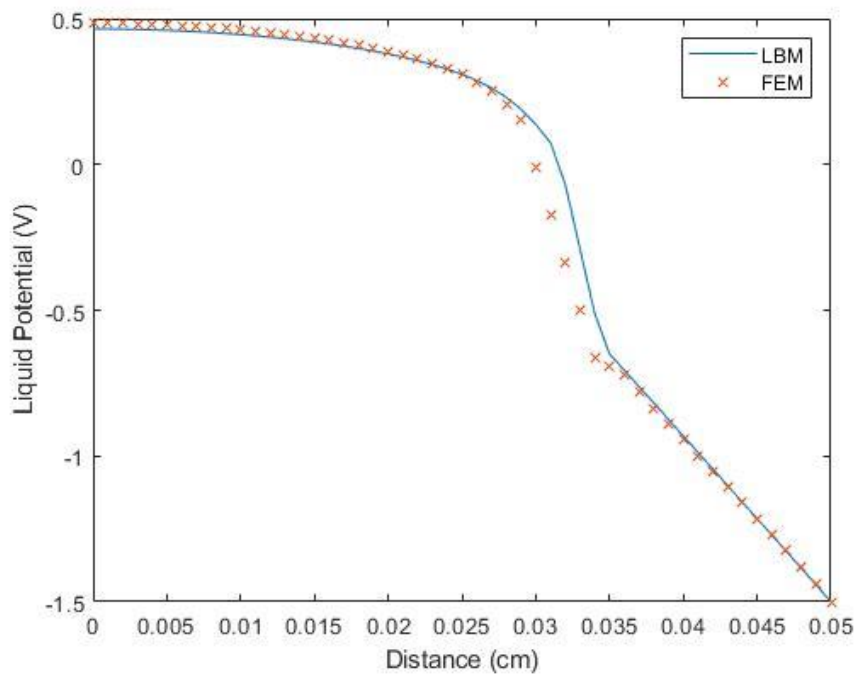


Figure 40: Single Cell Reactor Electrolyte Potential

6.4 Effect of Reynolds Number on Iodide/Iodine Concentration

Next, a porous zone is mimicked in a channel. The channel has a length height H and length $3H$ while the porous zone is located $H/2$ from the inlet and has a length and height of H . For velocity, all the walls have a no-slip BC while inlet has a velocity BC and zero-gradient at the outlet. Concentration has a constant BC at the inlet and is zero gradient-everywhere else, except for the active nodes within the porous zone as will be discussed in section 4.5. A dilute solution with $C_{I_0^-}$ enters the channel with Poiseuille flow profile and varying maximum velocity U_{max} , as seen in Figure 41.

The simulations were carried out based $Re = 5, 1, 0.5, 0.1$ and porosity $\lambda = 0.9$. LBM relaxation constants are given in Table 2, with $\tau_{I^-} = \tau_I = 0.56$ for all pore Reynolds values with the equivalent spherical diameter $d_p = 0.0012$ (m). The electrochemical parameters can be found in Table 1.

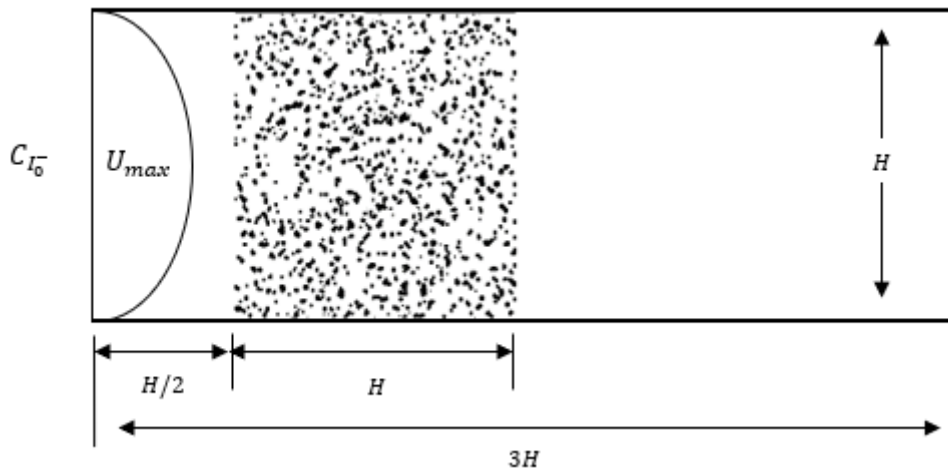
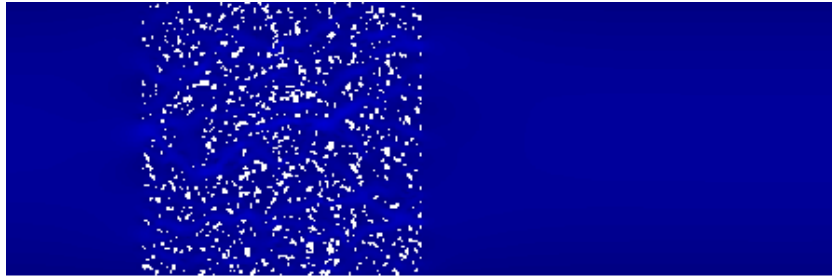


Figure 41: Physical Porous Structure in a Channel

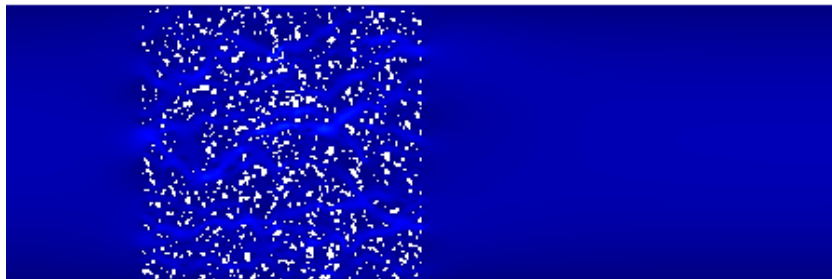
Table 2: Physical Porous Geometry LBM Simulation Parameters with Varying Reynolds Numbers

u_{max}	Re_p	τ_f
0.0025	0.1	0.80
0.005	0.5	0.62
0.01	1	0.62
0.025	5	0.56

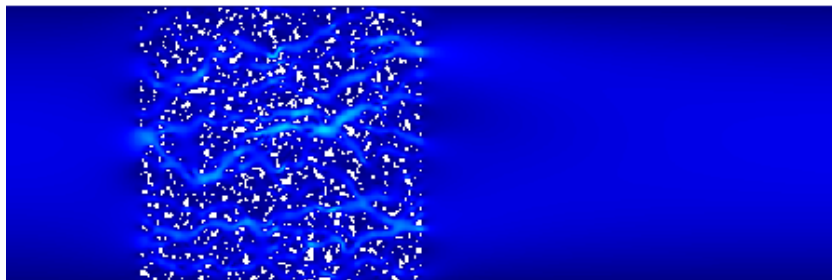
In order to study the effect of Re on concentration, the porous structure was identical for all cases. As illustrated in Figure 42, the flow path is seen to be consistent throughout the four cases. Furthermore, velocity distribution within the porous region is not uniform with some areas having higher velocities than others. Additionally, the velocity gradients within the regions are seen to differ with varying Re . The effect of Re on average velocity within the porous zone is shown in Figure 43. The average velocity, normalized by the respective maximum, is seen to decrease downstream with all Re values. The lowest outlet velocity seen with $Re=0.1$ and highest with $Re=5$, with a difference of 25%. The highest velocity gradient between the inlet and the outlet of the porous zone is seen with $Re=0.1$, wherewith the velocity decreased by 28%. With $Re=0.5$ the velocity profile is very similar, with 23% decrease.



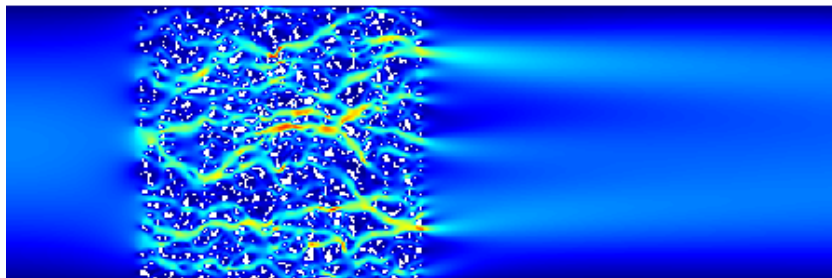
(a)



(b)



(c)



(d)

Figure 42: Velocity Contours with Re= (a) 0.1, (b) 0.5, (c) 1, (d) 5

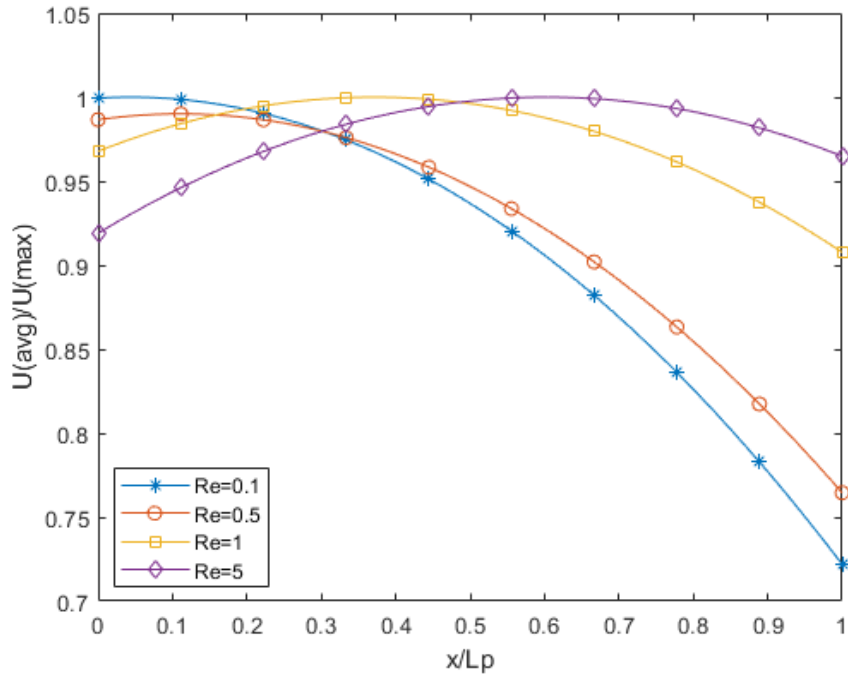
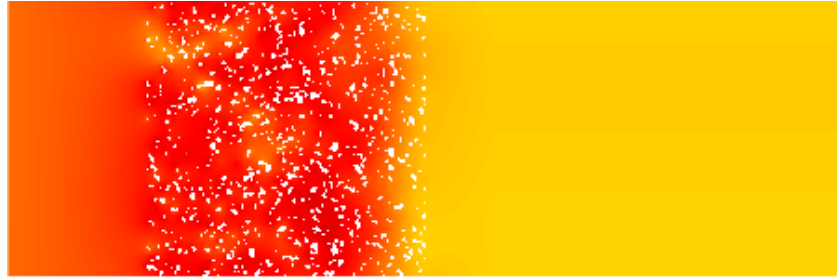


Figure 43 Average Velocity in the Porous Region with Varying Re

Further increase of $Re = 1$ resulted in only a 5% velocity decrease, while $Re=5$ resulted in a 5% increase.

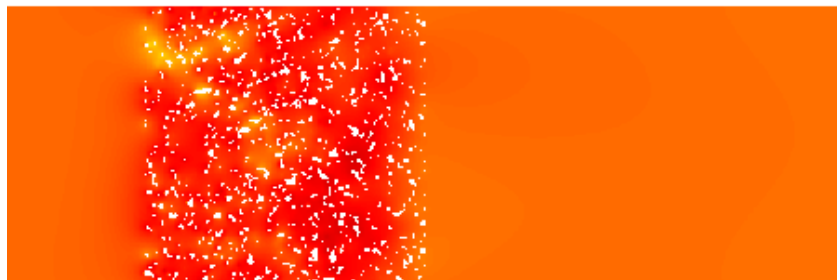
The effect of Re on iodide concentration is shown in Figure 44. Iodide concentration is seen to decrease downstream, near the outlet of porous zone, with $Re=0.1, 0.5$ and 1 . Since the potential distribution was the same for all cases, the concentration change can be related to velocity and consequently residence time. Comparing velocity and iodide concentration contours, Figures 42 and 44 respectively, it can be noted that the upstream region for $Re=5$ is seen to have higher concentration gradients as opposed to $Re=0.1$. This can be attributed to the flow path where less iodide is moving through those areas rather than due to consumption.



(a)



(b)



(c)



(d)

Figure 44: Iodide Concentration Contours with Re= (a) 0.1, (b) 0.5, (c) 1, (d) 5

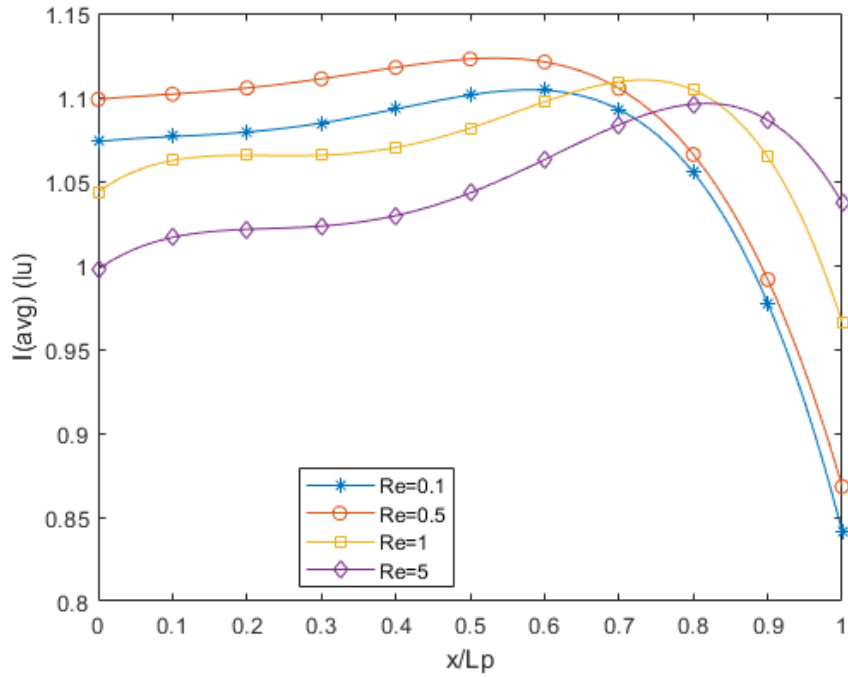
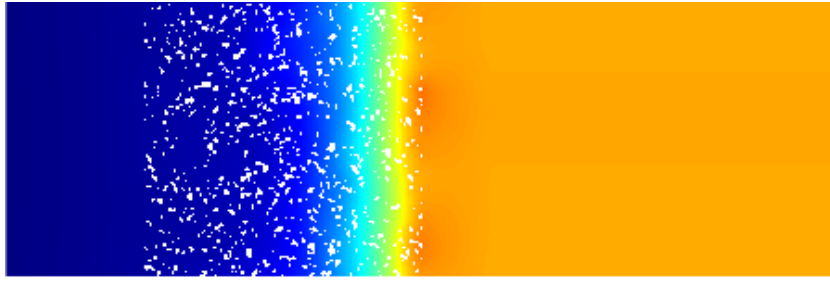


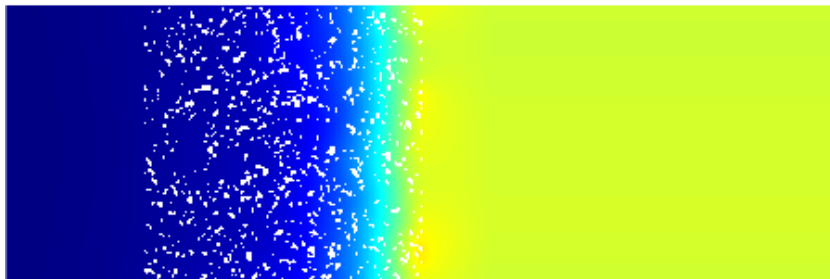
Figure 45: Average Iodide Concentration in the Porous Region with Varying Re

The iodide oxidation increases by 17% between $Re=5$ and 0.1, meanwhile a 10% increase is observed between 1 and 0.5 and only 4% between 0.5 and 0, as seen in Figure 45.

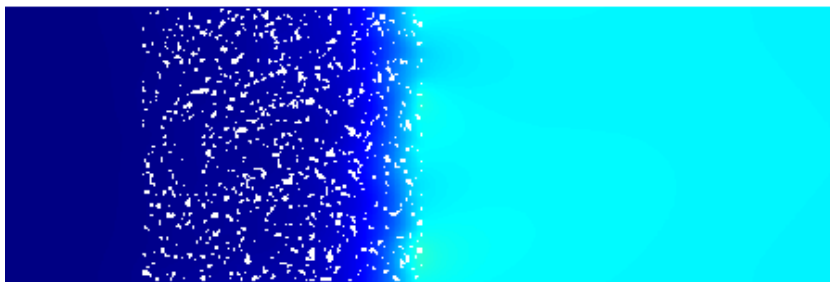
Similarly, most of the iodine is produced near the end of the porous zone as seen in Figures 46 and 47. The iodine production increases 300% with the decrease of Re from 5 to 0.1, meanwhile 55% between 1 and 0.5 followed by 18% between 0.5 and 0.1. Furthermore, little to no iodine is produced upstream with $Re=5$, which further indicates that the concentration gradients near the porous zone entrance, seen in Figure 44, are due to flow path and not the reaction. The results show that in addition to decreased residence times and mass transfer limitations due to higher velocity, less surface area is utilized with higher flows.



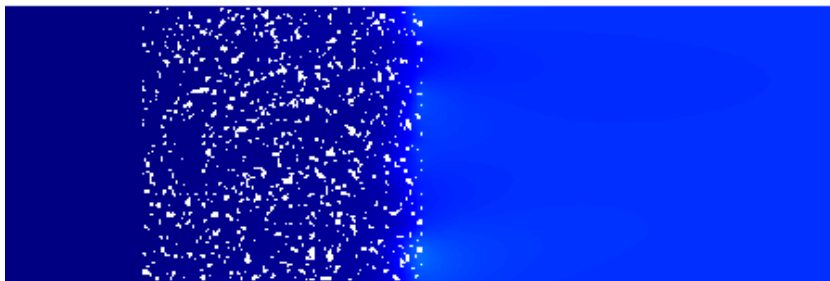
(a)



(b)



(c)



(d)

Figure 46: Iodine Concentration Contour with $Re = (a) 0.1, (b) 0.5, (c) 1, (d) 5$

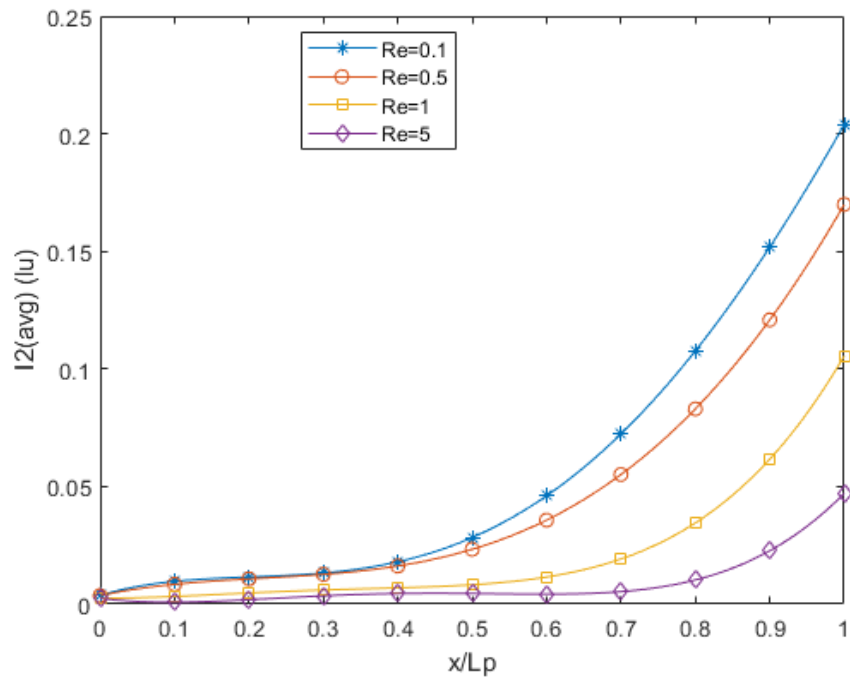
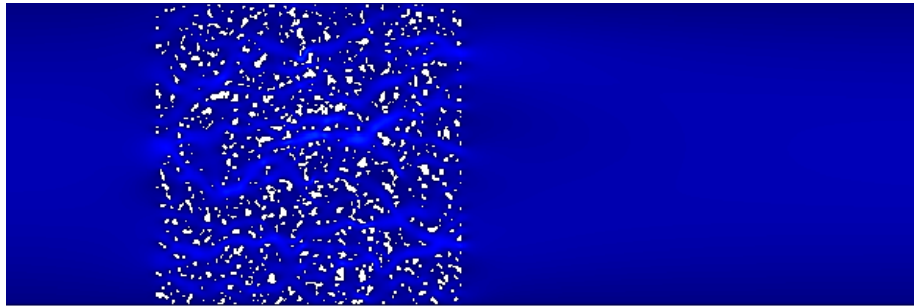


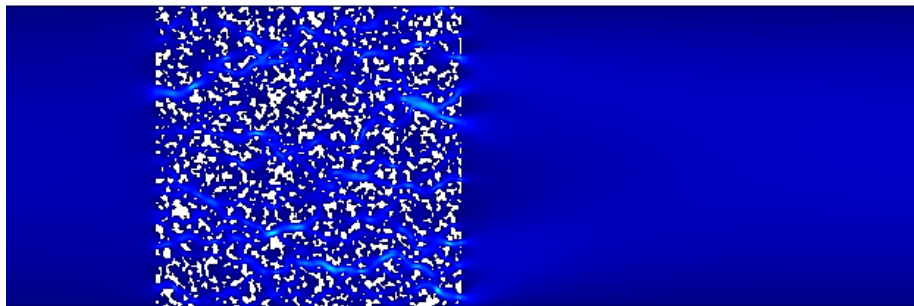
Figure 47: Average Iodine Concentration with Varying Re

6.5 Effect of Porosity on Iodide/Iodine Concentration

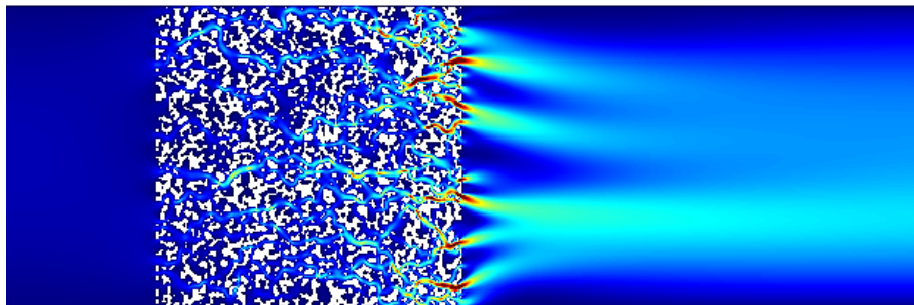
In this section the effects of porosity on oxidation of iodide to iodine were investigated based on $Re=1$. Porosity was varied with $\lambda=0.9, 0.8$ and 0.7 . The particle sphere diameter d_p was adjusted based on the ratio of porosities. Figure 48 shows the flow profile with varying porosity. The decrease in



(a)



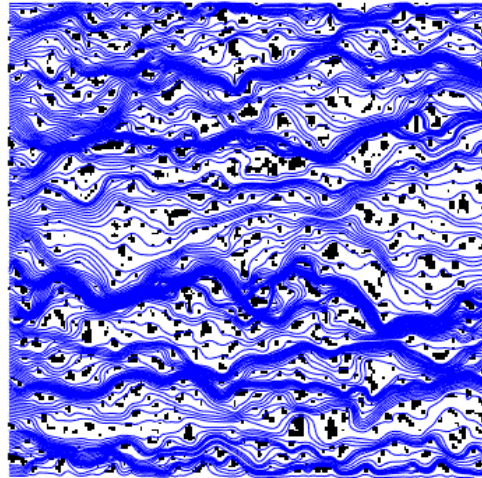
(b)



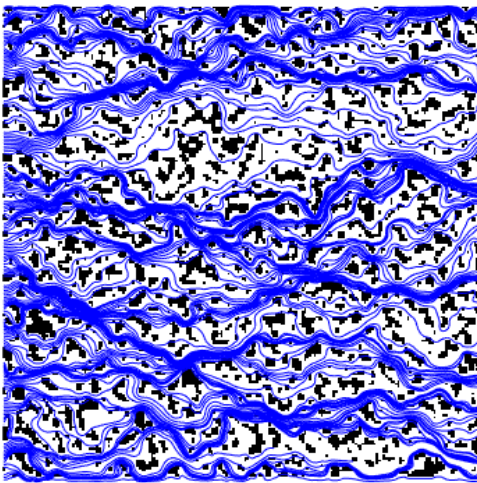
(c)

Figure 48: Velocity Contours with Velocity Contours with (a) $\lambda=0.9$, (b) $\lambda=0.8$, (c) $\lambda=0.7$

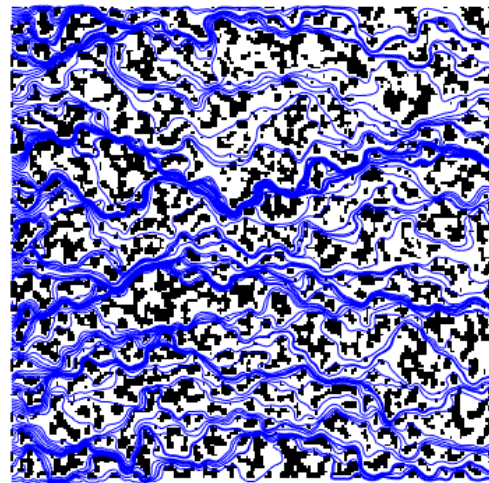
porosity corresponds to higher velocity gradients between the regions within the porous zone. The streamlines, shown in Figure 49, highlight the flow paths with different porosities. With the decrease in porosity the flow is more restricted, resulting in fewer pathways being utilized. As seen in Figure 49c, because of the flow restriction more stagnant regions, areas with little to no flow, are observed.



(a)



(b)



(c)

Figure 49: Flow Streamlines with (a) $\lambda=0.9$, (b) $\lambda=0.8$, (c) $\lambda=0.7$

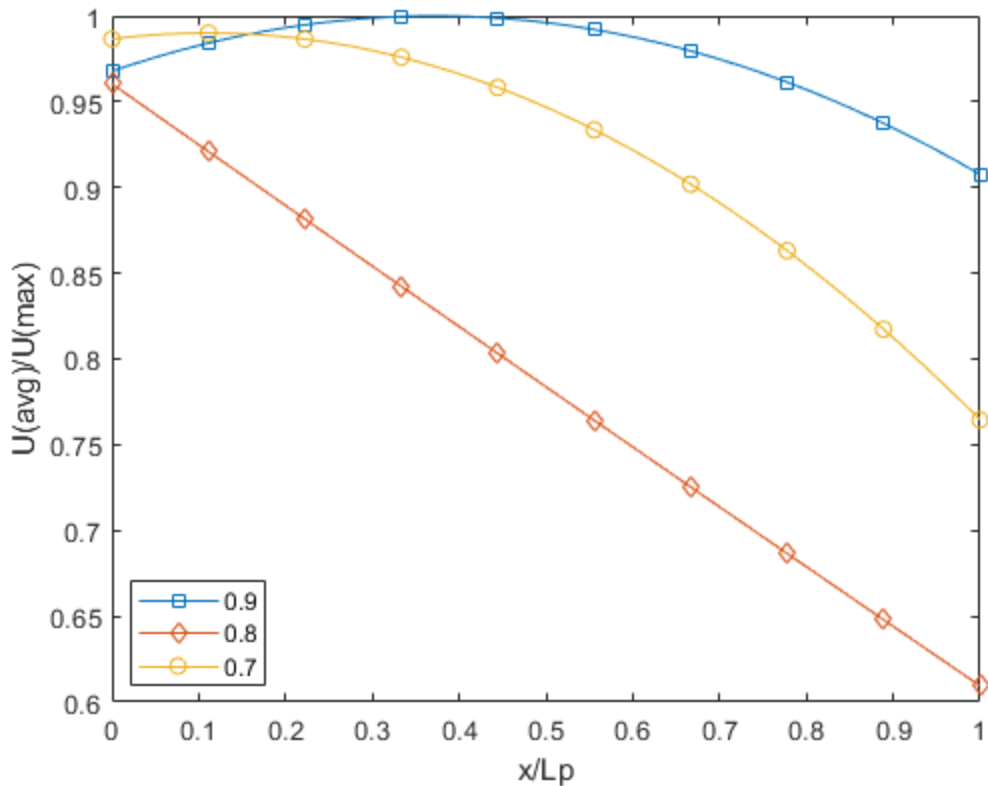


Figure 50: Average Velocity with Varying Porosity

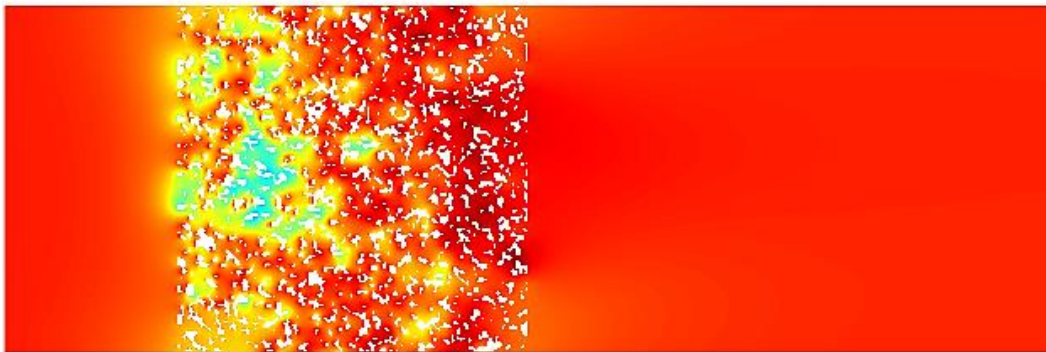
The largest average velocity change between the entrance and the exit of the porous zone is seen with $\lambda=0.8$ at a 36% decrease, Figure 50. With $\lambda=0.9$ and $\lambda=0.7$, the average velocity decreased 5% and 22%, respectively. The largest exit velocity difference of 33% is seen between $\lambda=0.9$ and $\lambda=0.8$, while 16% between $\lambda=0.9$ and $\lambda=0.7$. The linear decrease observed with $\lambda=0.8$ is likely due to a more symmetrical porous arrangement as opposed to the non-linear behaviour seen with $\lambda=0.9$ and $\lambda=0.7$.

The iodide concentration contours are given in Figure 51. Decreasing porosity is seen to result in decreased iodide concentration near the end of the porous zone and unlike with Re also upstream.

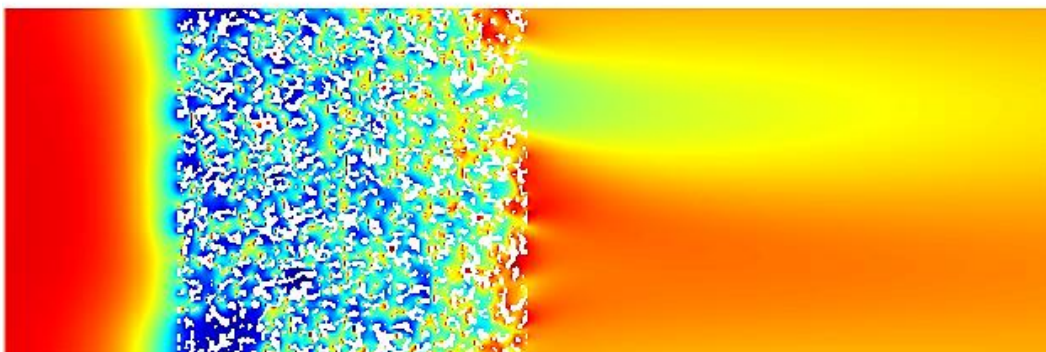
In this case, the decreased iodide concentration can be attributed to increased oxidation as iodine is produced, see Figures 53 and 54.



(a)



(b)



(c)

Figure 51: Iodide Concentration Contours with (a) $\lambda=0.9$, (b) $\lambda=0.8$, (c) $\lambda=0.7$

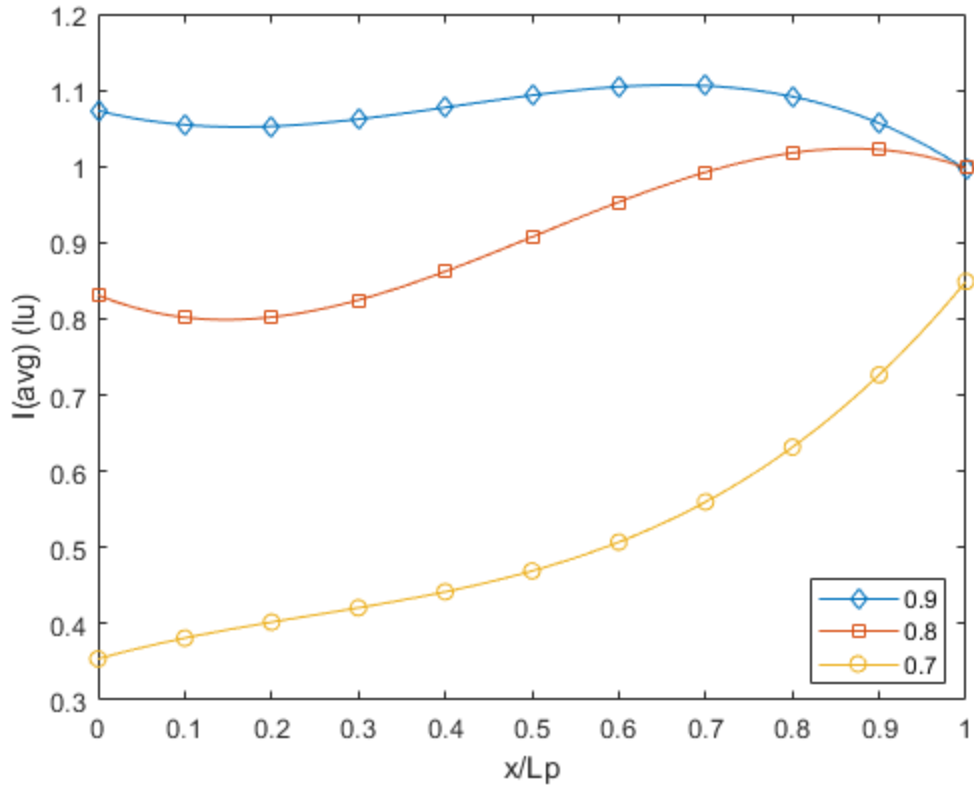
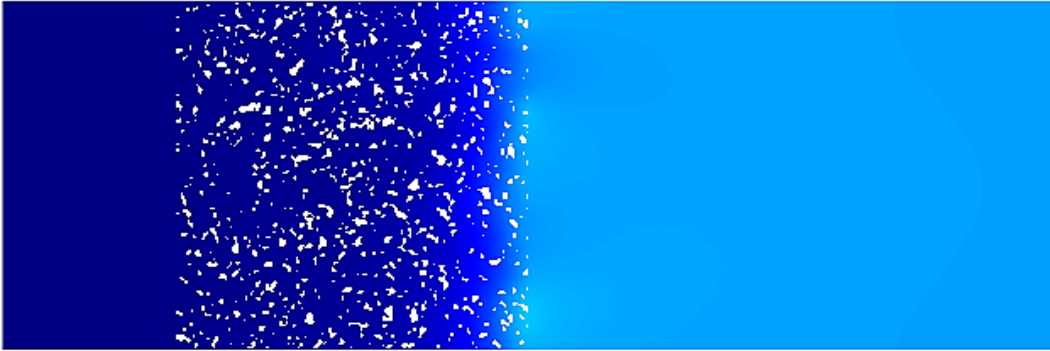
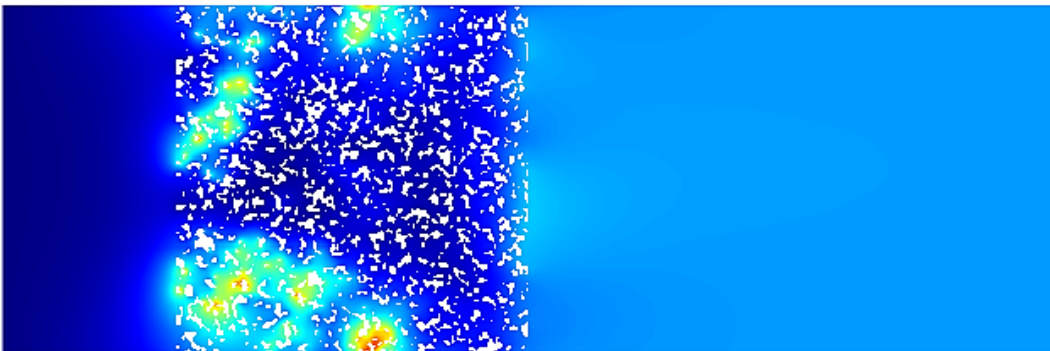


Figure 52: Average Iodide Concentration with Varying Porosity

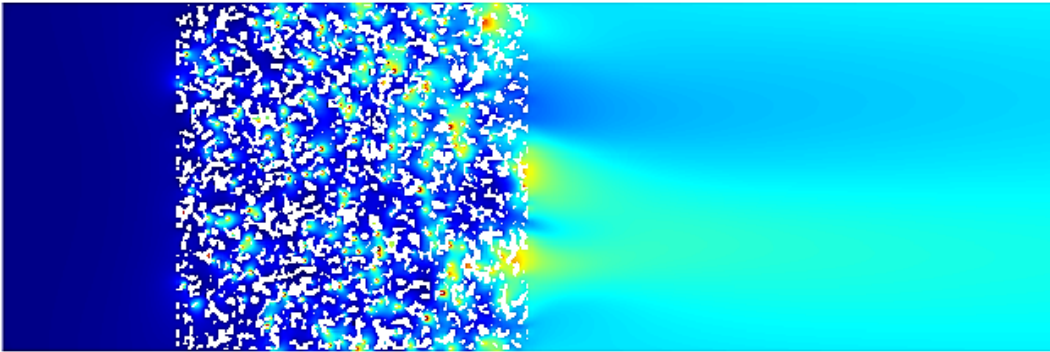
The average iodide concentration is illustrated in Figure 52, whereby decreasing porosity from $\lambda=0.9$ to 0.7 resulted in a 68% less iodide at the porous zone entrance. However, at the exit, the iodide concentration decreased only by 15%. The increasing trend in iodide concentration with $\lambda=0.7$ can be attributed to the fact that even though oxidation still occurs downstream, more iodide is present in the stagnant regions. Furthermore, it is likely that the mass transfer is limited and diffusion is slow in those regions.



(a)



(b)



(c)

Figure 53: Iodine Concentration Contours with (a) $\lambda=0.9$, (b) $\lambda=0.8$, (c) $\lambda=0.7$

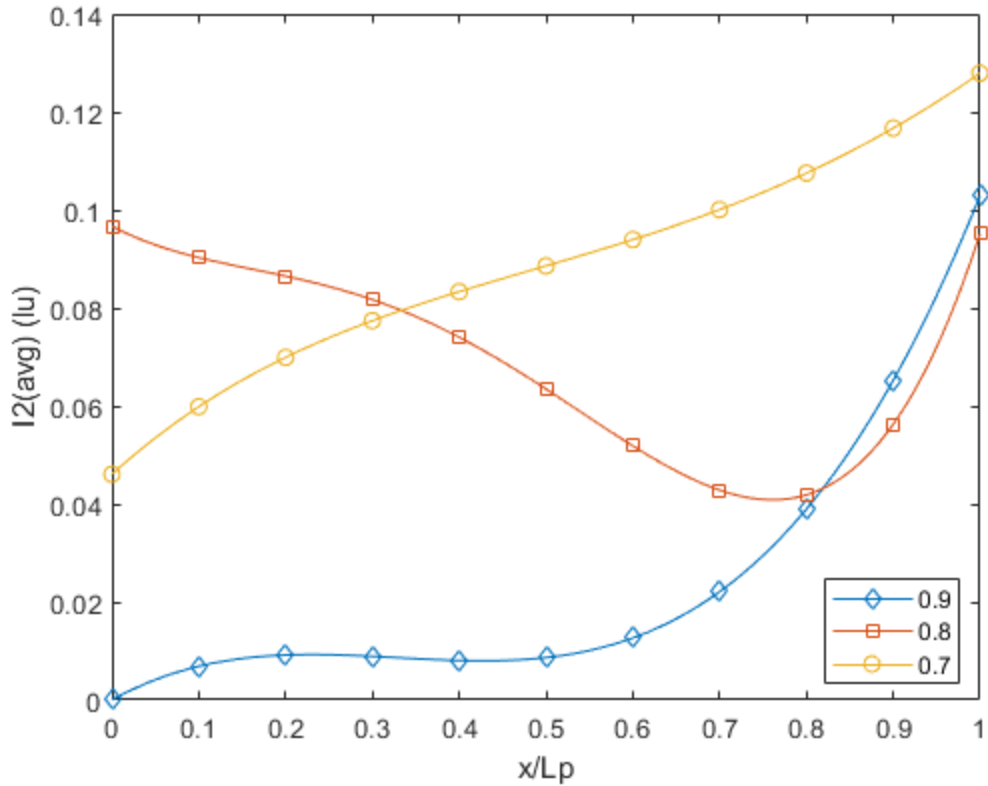


Figure 54: Average Iodine Concentration in the Porous Region with Varying Porosity

The iodine production increased by 30% with the decrease in porosity from $\lambda=0.9$ and $\lambda=0.7$ as seen in Figure 54, meanwhile a decrease of 5 % resulted in decreasing porosity from $\lambda=0.9$ to $\lambda=0.8$. This indicates that the surface kinetics can be enhanced by the porosity decrease, while hindered by the structure of the solid matrix.

6.6 Summary

The developed LBM algorithm was applied to the pseudo and physical flow-through porous electrodes in this chapter. The relationship between current, potential and the concentrations of the iodide/iodine couple was studied in the pseudo porous anode and a single cell reactor. The LBM results were compared with Finite Element Analysis. Additionally, a set of two-dimensional simulations, using the physical porous anode structure, were performed. The effects of varying Reynolds number and porosity on the iodide and iodine concentrations were studied.

Chapter 7

Conclusion and Future Work

7.1 Conclusion

This work has focused on the Pore-scale modelling of electrochemically active flow.. The primary goal was to develop and apply LBM model for simulating heterogeneous reactions involved in electrochemical reactors. The electrochemical fundamentals were introduced to provide enough background information and become familiar with the resurging topic of electrochemical methods. The Boltzmann equation was then described along with LBM implementation. A set of introductory examples and benchmarks were provided to highlight the advantages of deploying the chosen numerical method for the given problem. The chosen initial simulations for fully developed fluid flow, flow around an obstacle and species transport were selected as part of progression for model development.

The focus of this research was on developing a mathematic model, followed by dimensional analysis and scale conversion to simulate iodide/iodine redox surface reactions in a one-dimensional reactor consisting of a flow-through porous anode, spacer, and cathode. The cell configuration and its utilization in Electrochemical Advanced Oxidation Process for the purpose of water disinfection was elucidated. A new LBM algorithm was developed to simulate the unknown potential and concentration distributions simultaneously via addition of a reaction

source/sink to the distribution function. The pseudo-porous approach, incorporating both the continuum and LBM, was shown to be in excellent agreement with Finite Element Analysis.

The developed model was then augmented for the purpose of pore-scale modelling using physical porous geometry. The subsequent simulations mimicked a two-dimensional porous structure utilizing enhanced boundary conditions for the treatment of interfaces between a solid and an electrolyte. The porous matrix was randomly generated having a Gaussian distribution and segmented into active and inactive surfaces to model surface reactions. The solid and liquid potential distribution were imposed from the results obtained with the pseudo approach. Simulations were carried out based on varying Reynolds numbers with the same porosity and then varying porosity with the same Reynolds number. The results showed that decreasing Re from 5 to 0.1 resulted in a 300% iodine production increase, while decreasing porosity from 0.9 to 0.7 yielded only 15% increase. The effects of decreasing porosity on iodine production may, however, be hindered by the structure of the solid matrix. The results indicate that the flow regime has a far greater effect than porosity changes in the $0.1 \leq Re \leq 5$ and $0.7 \leq \lambda \leq 0.9$ ranges.

7.2 Future Work

The next steps in developing a more elaborate model are recommended to be:

- Involving more reactions such as oxidation of iodine to iodate and further iodate oxidization to periodate. Insight into radical formation for various treatment applications is critical. Validated numerical models can facilitate understanding into optimal reactor parameters.
- Perform an experiment with an electrochemical reactor to compare LBM results. Thus far the validation exists only in the numerical realm.
- Investigate the electrochemical cell in two dimensions. Rather than just the anode, incorporate a two-dimensional porous spacer and cathode as well.
- Due to the relative simplicity in LBM code implementation, three-dimensional flow-through electrodes can be studied. It would be interesting to see an actual porous structure, imaged either via destructive methods or using a scanning electron microscope, and the extension of the developed code for such problem.

References

- [1] D. Marmer, “Water Conservation Equals Energy Conservation*,” *Energy Eng. J. Assoc. Energy Eng.*, vol. 115, no. 5, pp. 48–63, 2018, doi: 10.1080/01998595.2018.12027708.
- [2] H. Chang, *Water and Climate Change*. 2019.
- [3] A. Guamán and H. Yumisaca, *Estimated use of water in the United States*. 2015.
- [4] OECD, *OECD Environmental Outlook to 2050*. 2012.
- [5] U. Nations, “The United Nations World Water Development Report 2021: Valuing Water.,” Paris, 2020.
- [6] D. M. Rockwood, “Water and energy,” *GeoJournal*, vol. 3, no. 5, pp. 461–470, 1979, doi: 10.1007/BF00455985.
- [7] WWAP, “Managing Water under Uncertainty and Risk (UNWWD Report 4, Vol 1),” 2012. [Online]. Available: <http://unesdoc.unesco.org/images/0021/002156/215644e.pdf>.
- [8] IEA, “Water Energy Nexus- Excerpt from the World Energy Outlook 2016,” *Iea*, p. 60, 2016, [Online]. Available: <https://www.iea.org/publications/freepublications/publication/WorldEnergyOutlook2016ExcerptWaterEnergyNexus.pdf>.
- [9] D. Mytton, “Data centre water consumption,” *npj Clean Water*, vol. 4, no. 1, 2021, doi: 10.1038/s41545-021-00101-w.
- [10] K. Pullerits *et al.*, “Impact of UV irradiation at full scale on bacterial communities in drinking water,” *npj Clean Water*, vol. 3, no. 1, pp. 1–10, 2020, doi: 10.1038/s41545-020-0057-7.

- [11] H. Canada, “Drinking Water Chlorination.” <https://www.canada.ca/en/health-canada/services/healthy-living/your-health/environment/drinking-water-chlorination.html>.
- [12] M. Sisti, G. F. Schiavano, M. De Santi, and G. Brandi, “Ultraviolet germicidal irradiation in tap water contaminated by *Aspergillus* spp,” *J. Prev. Med. Hyg.*, vol. 58, no. 4, pp. E315–E319, 2017, doi: 10.15167/2421-4248/jpmh2017.58.4.777.
- [13] P. E. Black, *Drinking Water and Health, Volume*, vol. 20, no. 6. 1984.
- [14] S. Hand and R. D. Cusick, “Electrochemical Disinfection in Water and Wastewater Treatment: Identifying Impacts of Water Quality and Operating Conditions on Performance,” *Environ. Sci. Technol.*, vol. 55, no. 6, pp. 3470–3482, Mar. 2021, doi: 10.1021/acs.est.0c06254.
- [15] I. Sirés, E. Brillas, M. A. Oturan, M. A. Rodrigo, and M. Panizza, “Electrochemical advanced oxidation processes: Today and tomorrow. A review,” *Environ. Sci. Pollut. Res.*, vol. 21, no. 14, pp. 8336–8367, 2014, doi: 10.1007/s11356-014-2783-1.
- [16] S. Hand and R. D. Cusick, “Electrochemical Disinfection in Water and Wastewater Treatment: Identifying Impacts of Water Quality and Operating Conditions on Performance,” *Environ. Sci. Technol.*, vol. 55, no. 6, pp. 3470–3482, 2021, doi: 10.1021/acs.est.0c06254.
- [17] K. Liu, C. Song, and A. Lei, “Recent advances in iodine mediated electrochemical oxidative cross-coupling,” *Org. Biomol. Chem.*, vol. 16, no. 14, pp. 2375–2387, 2018, doi: 10.1039/C8OB00063H.
- [18] N. E. Chadi, S. Merouani, O. Hamdaoui, M. Bouhelassa, and M. Ashokkumar, “Influence of mineral water constituents, organic matter and water matrices on the performance of the H₂O₂/IO₄⁻-advanced oxidation process,” *Environ. Sci. Water Res. Technol.*, vol. 5,

- no. 11, pp. 1985–1992, 2019, doi: 10.1039/C9EW00329K.
- [19] B. P. Chaplin, “Critical review of electrochemical advanced oxidation processes for water treatment applications,” *Environ. Sci. Process. Impacts*, vol. 16, no. 6, pp. 1182–1203, 2014, doi: 10.1039/c3em00679d.
- [20] F. C. Moreira, R. A. R. Boaventura, E. Brillas, and V. J. P. Vilar, “Electrochemical advanced oxidation processes: A review on their application to synthetic and real wastewaters,” *Appl. Catal. B Environ.*, vol. 202, pp. 217–261, 2017, doi: 10.1016/j.apcatb.2016.08.037.
- [21] D. Ghernaout, N. Elboughdiri, S. Ghareba, and A. Salih, “Electrochemical Advanced Oxidation Processes (EAOPs) for Disinfecting Water—Fresh Perspectives,” *OALib*, vol. 07, no. 04, pp. 1–12, 2020, doi: 10.4236/oalib.1106257.
- [22] R. P. H. Huijbregts, A. I. P. M. de Kroon, and B. de Kruijff, “On the accessibility of phosphatidylglycerol to periodate in *Escherichia coli*,” *Mol. Membr. Biol.*, vol. 14, no. 1, pp. 35–38, Jan. 1997, doi: 10.3109/09687689709048168.
- [23] A. Moustafa *et al.*, “Operando Studies of Iodine Species in an Advanced Oxidative Water Treatment Reactor,” *ACS ES&T Water*, vol. 1, no. 11, pp. 2293–2304, Nov. 2021, doi: 10.1021/acsestwater.1c00149.
- [24] T. Kaiho, Ed., *Iodine Chemistry and Applications*. Hoboken, NJ: John Wiley & Sons, Inc, 2014.
- [25] M. Okochi *et al.*, “Disinfection of Microorganisms by Use of Electrochemically Regenerated Periodate,” *Appl. Environ. Microbiol.*, vol. 71, no. 10, pp. 6410–6413, Oct. 2005, doi: 10.1128/AEM.71.10.6410-6413.2005.
- [26] X.-Y. Zhang *et al.*, “Continuous exposure to non-lethal doses of sodium iodate induces

- retinal pigment epithelial cell dysfunction,” *Sci. Rep.*, vol. 6, no. 1, p. 37279, Dec. 2016, doi: 10.1038/srep37279.
- [27] A. J. Sioda RE, Cook GM, Keating KB, Williams JM, “Flow-Through Porous Electrodes,” *Chem. Eng. (New York)*, vol. 90, pp. 57–67, 1983.
- [28] M. E. Suss *et al.*, “Capacitive desalination with flow-through electrodes,” *Energy Environ. Sci.*, vol. 5, no. 11, p. 9511, 2012, doi: 10.1039/c2ee21498a.
- [29] S. Bebelis *et al.*, “Highlights during the development of electrochemical engineering,” *Chem. Eng. Res. Des.*, vol. 91, no. 10, pp. 1998–2020, Oct. 2013, doi: 10.1016/j.cherd.2013.08.029.
- [30] J. S. Newman and C. W. Tobias, “Theoretical Analysis of Current Distribution in Porous Electrodes,” *J. Electrochem. Soc.*, vol. 109, no. 12, p. 1183, 1962, doi: 10.1149/1.2425269.
- [31] J. D. Milshtein, K. M. Tenny, J. L. Barton, J. Drake, R. M. Darling, and F. R. Brushett, “Quantifying Mass Transfer Rates in Redox Flow Batteries,” *J. Electrochem. Soc.*, vol. 164, no. 11, pp. E3265–E3275, 2017, doi: 10.1149/2.0201711jes.
- [32] Y. Volkman, “Optimization of the effectiveness of a three-dimensional electrode with respect to its ohmic variables,” *Electrochim. Acta*, vol. 24, no. 11, pp. 1145–1149, Nov. 1979, doi: 10.1016/0013-4686(79)87062-0.
- [33] K. Kinoshita and S. C. Leach, “Mass-Transfer Study of Carbon Felt, Flow-Through Electrode,” *J. Electrochem. Soc.*, vol. 129, no. 9, pp. 1993–1997, Sep. 1982, doi: 10.1149/1.2124338.
- [34] J. M. Bisang, K. Jüttner, and G. Kreysa, “Potential and current distribution in porous electrodes under charge-transfer kinetic control,” *Electrochim. Acta*, vol. 39, no. 8–9, pp.

- 1297–1302, Jun. 1994, doi: 10.1016/0013-4686(94)E0050-A.
- [35] M. M. Saleh, “Mathematical modeling of gas evolving flow-through porous electrodes,” *Electrochim. Acta*, vol. 45, no. 6, pp. 959–967, Dec. 1999, doi: 10.1016/S0013-4686(99)00296-0.
- [36] R. Carta, S. Palmas, A. M. Polcaro, and G. Tola, “Behaviour of a carbon felt flow by electrodes Part I: Mass transfer characteristics,” *J. Appl. Electrochem.*, vol. 21, no. 9, pp. 793–798, Sep. 1991, doi: 10.1007/BF01402816.
- [37] J. A. Trainham and J. Newman, “A Flow-Through Porous Electrode Model: Application to Metal-Ion Removal from Dilute Streams,” *J. Electrochem. Soc.*, vol. 124, no. 10, pp. 1528–1540, Oct. 1977, doi: 10.1149/1.2133106.
- [38] D. N. Bennion and J. Newman, “Electrochemical removal of copper ions from very dilute solutions,” *J. Appl. Electrochem.*, vol. 2, no. 2, pp. 113–122, May 1972, doi: 10.1007/BF00609127.
- [39] D. Pilone and G. H. Kelsall, “Model of Multiple Metal Electrodeposition in Porous Electrodes,” *J. Electrochem. Soc.*, vol. 153, no. 5, p. D85, 2006, doi: 10.1149/1.2178607.
- [40] R. C. Alkire, E. A. Grens, and C. W. Tobias, “A Theory for Porous Electrodes Undergoing Structural Change by Anodic Dissolution,” *J. Electrochem. Soc.*, vol. 116, no. 10, p. 1328, 1969, doi: 10.1149/1.2411505.
- [41] A. M. Zaky and B. P. Chaplin, “Porous Substoichiometric TiO₂ Anodes as Reactive Electrochemical Membranes for Water Treatment,” *Environ. Sci. Technol.*, vol. 47, no. 12, pp. 6554–6563, Jun. 2013, doi: 10.1021/es401287e.
- [42] K. S. G. C. Oliveira, R. M. Farinos, A. B. Veroli, and L. A. M. Ruotolo, “Electrochemical incineration of glyphosate wastewater using three-dimensional electrode,” *Environ.*

- Technol.*, vol. 42, no. 2, pp. 170–181, Jan. 2021, doi: 10.1080/09593330.2019.1625563.
- [43] B. N. Grgur, M. M. Gvozdenović, J. S. Stevanović, B. Z. Jugović, and L. T. Trišović, “Electrochemical oxidation of iodide in aqueous solution,” *Chem. Eng. J.*, vol. 124, no. 1–3, pp. 47–54, Nov. 2006, doi: 10.1016/j.cej.2006.08.028.
- [44] J. Newman and N. P. Balsara, *Electrochemical Systems*. Wiley, 2021.
- [45] A. Bard and L. Faulkner, *Electrochemical Methods: Fundamentals and Applications*, vol. 12. 2000.
- [46] V. Levich and S. Rice, “Physicochemical Hydrodynamics,” *Phys. Today*, vol. 16, p. 75, May 1963, doi: 10.1063/1.3050934.
- [47] R. Probstein, *Physicochemical Hydrodynamics*. 2003.
- [48] K. J. Vetter., “Electrochemical kinetics: theoretical and experimental aspects,” *Glycobiology*, vol. 2, no. 3, pp. 251–255, 1992, [Online]. Available: <https://academic.oup.com/glycob/article-lookup/doi/10.1093/glycob/2.3.251>.
- [49] J. M. Pingarrón *et al.*, “Terminology of electrochemical methods of analysis (IUPAC Recommendations 2019),” *Pure Appl. Chem.*, vol. 92, no. 4, pp. 641–694, 2020, doi: 10.1515/pac-2018-0109.
- [50] X. Jin, A. Ku, A. Verma, B. Ohara, K. Huang, and S. Singh, “The Performance of Syngas-Fueled SOFCs Predicted by a Reduced Order Model (ROM): Temperature and Fuel Composition Effects,” *J. Electrochem. Soc.*, vol. 165, no. 10, pp. F786–F798, 2018, doi: 10.1149/2.0511810jes.
- [51] E. J. F. Dickinson and A. J. Wain, “The Butler-Volmer equation in electrochemical theory: Origins, value, and practical application,” *J. Electroanal. Chem.*, vol. 872, p. 114145, 2020, doi: 10.1016/j.jelechem.2020.114145.

- [52] R. Guidelli *et al.*, “Defining the transfer coefficient in electrochemistry: An assessment (IUPAC Technical Report),” *Pure Appl. Chem.*, vol. 86, no. 2, pp. 245–258, 2014, doi: 10.1515/pac-2014-5026.
- [53] J. Price, “Lagrangian and eulerian representations of fluid flow: Kinematics and the equations of motion,” 2006.
- [54] S. Succi, *The Lattice Boltzmann Equation for Fluid Dynamics and Beyond*. Oxford Science, 2001.
- [55] M. C. Sukop and D. T. Thorne, *Lattice Boltzmann Modeling*. Berlin, Heidelberg: Springer Berlin Heidelberg, 2006.
- [56] T. Krüger, H. Kusumaatmaja, A. Kuzmin, O. Shardt, G. Silva, and E. M. Viggien, *The Lattice Boltzmann Method*. Cham: Springer International Publishing, 2017.
- [57] D. A. Wolf-Gladrow, *Lattice Gas Cellular Automata and Lattice Boltzmann Models*, vol. 1725. Berlin, Heidelberg: Springer Berlin Heidelberg, 2000.
- [58] A. A. Mohamad, *Lattice Boltzmann Method*. London: Springer London, 2011.
- [59] Y. Feng, M. Tayyab, and P. Boivin, “A Lattice-Boltzmann model for low-Mach reactive flows,” *Combust. Flame*, vol. 196, pp. 249–254, 2018, doi: 10.1016/j.combustflame.2018.06.027.
- [60] H. E. Van den Akker, “Lattice Boltzmann simulations for multi-scale chemical engineering,” *Curr. Opin. Chem. Eng.*, vol. 21, pp. 67–75, 2018, doi: 10.1016/j.coche.2018.03.003.
- [61] G. T. Zachariah, D. Panda, and V. K. Surasani, “Lattice Boltzmann simulations for invasion patterns during drying of capillary porous media,” *Chem. Eng. Sci.*, vol. 196, pp. 310–323, 2019, doi: 10.1016/j.ces.2018.11.003.

- [62] A. Xu, W. Shyy, and T. Zhao, “Lattice Boltzmann modeling of transport phenomena in fuel cells and flow batteries,” *Acta Mech. Sin. Xuebao*, vol. 33, no. 3, pp. 555–574, 2017, doi: 10.1007/s10409-017-0667-6.
- [63] H. Safari, M. H. Rahimian, and M. Krafczyk, “Extended lattice Boltzmann method for numerical simulation of thermal phase change in two-phase fluid flow,” *Phys. Rev. E - Stat. Nonlinear, Soft Matter Phys.*, vol. 88, no. 1, pp. 1–12, 2013, doi: 10.1103/PhysRevE.88.013304.
- [64] J. Horbach and D. Frenkel, “Lattice-Boltzmann method for the simulation of transport phenomena in charged colloids,” *Phys. Rev. E - Stat. Physics, Plasmas, Fluids, Relat. Interdiscip. Top.*, vol. 64, no. 6, p. 8, 2001, doi: 10.1103/PhysRevE.64.061507.
- [65] P. J. Dellar, “Bulk and shear viscosities in lattice Boltzmann equations,” *Phys. Rev. E - Stat. Physics, Plasmas, Fluids, Relat. Interdiscip. Top.*, vol. 64, no. 3, p. 11, 2001, doi: 10.1103/PhysRevE.64.031203.
- [66] S. Javed, A. Sohail, K. Maqbool, S. I. Butt, and Q. A. Chaudhry, “The Lattice Boltzmann method and computational analysis of bone dynamics-I,” *Complex Adapt. Syst. Model.*, vol. 5, no. 1, pp. 1–14, 2017, doi: 10.1186/s40294-017-0051-1.
- [67] C. Cercignani, *The Boltzmann Equation and Its Applications*, vol. 67. New York, NY: Springer New York, 1988.
- [68] X. B. Nie, X. Shan, and H. Chen, “Galilean invariance of lattice Boltzmann models,” *EPL (Europhysics Lett.)*, vol. 81, no. 3, p. 34005, Feb. 2008, doi: 10.1209/0295-5075/81/34005.
- [69] A. S. Joshi, K. N. Grew, A. A. Peracchio, and W. K. S. Chiu, “Lattice Boltzmann modeling of 2D gas transport in a solid oxide fuel cell anode,” *J. Power Sources*, vol. 164, no. 2, pp. 631–638, Feb. 2007, doi: 10.1016/j.jpowsour.2006.10.101.

- [70] J. Bear, *Dynamics of Fluids in Porous Media*. New York: American Elsevier Pub. Co, 1972.
- [71] M. A. Mujeebu, M. Z. Abdullah, M. Z. A. Bakar, A. A. Mohamad, R. M. N. Muhad, and M. K. Abdullah, “Combustion in porous media and its applications – A comprehensive survey,” *J. Environ. Manage.*, vol. 90, no. 8, pp. 2287–2312, Jun. 2009, doi: 10.1016/j.jenvman.2008.10.009.
- [72] J. Latt, “Hydrodynamic limit of lattice Boltzmann equations,” Geneve, 2007.
- [73] X. Nie and N. S. Martys, “Breakdown of Chapman-Enskog expansion and the anisotropic effect for lattice-Boltzmann models of porous flow,” *Phys. Fluids*, vol. 19, no. 1, pp. 8–12, 2007, doi: 10.1063/1.2432153.
- [74] A. Hu, L. Li, and R. Uddin, “Force method in a pseudo-potential lattice Boltzmann model,” vol. 294, pp. 78–89, 2015.
- [75] S. A. Bawazeer, S. S. Baakeem, and A. A. Mohamad, “A Critical Review of Forcing Schemes in Lattice Boltzmann Method: 1993–2019,” *Arch. Comput. Methods Eng.*, no. 0123456789, 2021, doi: 10.1007/s11831-021-09535-4.
- [76] D. Yu, R. Mei, L.-S. Luo, and W. Shyy, “Viscous flow computations with the method of lattice Boltzmann equation,” *Prog. Aerosp. Sci.*, vol. 39, no. 5, pp. 329–367, Jul. 2003, doi: 10.1016/S0376-0421(03)00003-4.
- [77] I. Ginzbourg and P. M. Adler, “Boundary flow condition analysis for the three-dimensional lattice Boltzmann model,” *J. Phys. II*, vol. 4, no. 2, pp. 191–214, Feb. 1994, doi: 10.1051/jp2:1994123.
- [78] H. Liu, J. G. Zhou, and R. Burrows, “Inlet and outlet boundary conditions for the Lattice-Boltzmann modelling of shallow water flows,” *Prog. Comput. Fluid Dyn. An Int. J.*, vol.

- 12, no. 1, p. 11, 2012, doi: 10.1504/PCFD.2012.044850.
- [79] J. D. Sterling and S. Chen, “Stability Analysis of Lattice Boltzmann Methods,” *J. Comput. Phys.*, vol. 123, no. 1, pp. 196–206, Jan. 1996, doi: 10.1006/jcph.1996.0016.
- [80] Q. Zou and X. He, “On pressure and velocity boundary conditions for the lattice Boltzmann BGK model,” *Phys. Fluids*, vol. 9, no. 6, pp. 1591–1598, Jun. 1997, doi: 10.1063/1.869307.
- [81] A. Mussa, P. Asinari, and L.-S. Luo, “Lattice Boltzmann simulations of 2D laminar flows past two tandem cylinders,” *J. Comput. Phys.*, vol. 228, no. 4, pp. 983–999, Mar. 2009, doi: 10.1016/j.jcp.2008.10.010.
- [82] S. Succi, “Applied Lattice Boltzmann Method for Transport Phenomena, Momentum, Heat and Mass Transfer. A. A. Mohamad Sure Printing, Calgary, AB April 2007,” *Can. J. Chem. Eng.*, vol. 85, no. 6, pp. 946–947, May 2008, doi: 10.1002/cjce.5450850617.
- [83] A. A. Alamyane and A. A. Mohamad, “Simulation of forced convection in a channel with extended surfaces by the lattice Boltzmann method,” *Comput. Math. with Appl.*, vol. 59, no. 7, pp. 2421–2430, Apr. 2010, doi: 10.1016/j.camwa.2009.08.070.
- [84] R. J. MILLINGTON and J. P. QUIRK, “Formation Factor and Permeability Equations,” *Nature*, vol. 202, no. 4928, pp. 143–145, Apr. 1964, doi: 10.1038/202143a0.
- [85] R. C. Alkire, D. M. Kolb, L. A. Kibler, and J. Lipkowski, Eds., *Electrocatalysis*, vol. 14. Wiley, 2013.
- [86] S. S. Baakeem, S. A. Bawazeer, and A. A. Mohamad, “A novel approach of unit conversion in the lattice boltzmann method,” *Appl. Sci.*, vol. 11, no. 14, 2021, doi: 10.3390/app11146386.
- [87] J. Latt, “Choice of units in lattice Boltzmann simulations,” 2008.

- [88] E. Chiavazzo, I. V Karlin, A. N. Gorban, and K. Boulouchos, “Combustion simulation via lattice Boltzmann and reduced chemical kinetics,” *J. Stat. Mech. Theory Exp.*, vol. 2009, no. 06, p. P06013, Jun. 2009, doi: 10.1088/1742-5468/2009/06/P06013.
- [89] S. H. Ashworth, *A student’s guide to dimensional analysis*, vol. 59, no. 4. Cambridge University Press, 2018.
- [90] O. R. Spies, “Dimensional analysis and theory of models,” *J. Franklin Inst.*, vol. 253, no. 1, p. 84, Jan. 1952, doi: 10.1016/0016-0032(52)90438-9.
- [91] P. . Bridgman, *Dimensional analysis*, 2nd ed. New Heaven: Yale University Press, 1931.
- [92] A. Ghassemi and A. Pak, “Pore scale study of permeability and tortuosity for flow through particulate media using Lattice Boltzmann method,” *Int. J. Numer. Anal. Methods Geomech.*, vol. 35, no. 8, pp. 886–901, Jun. 2011, doi: 10.1002/nag.932.
- [93] Q. Kang, P. C. Lichtner, and D. Zhang, “An improved lattice Boltzmann model for multicomponent reactive transport in porous media at the pore scale,” *Water Resour. Res.*, vol. 43, no. 12, pp. 1–12, Dec. 2007, doi: 10.1029/2006WR005551.
- [94] L. Hao and P. Cheng, “Pore-scale simulations on relative permeabilities of porous media by lattice Boltzmann method,” *Int. J. Heat Mass Transf.*, vol. 53, no. 9–10, pp. 1908–1913, Apr. 2010, doi: 10.1016/j.ijheatmasstransfer.2009.12.066.
- [95] E. Fattahi, C. Waluga, B. Wohlmuth, U. Rde, M. Manhart, and R. Helmig, “Lattice Boltzmann methods in porous media simulations: From laminar to turbulent flow,” *Comput. Fluids*, vol. 140, pp. 247–259, Nov. 2016, doi: 10.1016/j.compfluid.2016.10.007.
- [96] M. E. Kutay, A. H. Aydilek, and E. Masad, “Laboratory validation of lattice Boltzmann method for modeling pore-scale flow in granular materials,” *Comput. Geotech.*, vol. 33, no. 8, pp. 381–395, Dec. 2006, doi: 10.1016/j.compgeo.2006.08.002.

- [97] H. Yoon, Q. Kang, and A. J. Valocchi, “Lattice Boltzmann-Based Approaches for Pore-Scale Reactive Transport,” *Rev. Mineral. Geochemistry*, vol. 80, no. 1, pp. 393–431, 2015, doi: 10.2138/rmg.2015.80.12.
- [98] H. Li, H. J. H. Clercx, and F. Toschi, “LBM Investigations on a Chain Reaction in a Reactive Electro-Kinetic Flow in Porous Material,” *J. Electrochem. Soc.*, vol. 168, no. 8, p. 083502, Aug. 2021, doi: 10.1149/1945-7111/ac1b4a.
- [99] Q. Kang, D. Zhang, and S. Chen, “Unified lattice Boltzmann method for flow in multiscale porous media,” *Phys. Rev. E*, vol. 66, no. 5, p. 056307, Nov. 2002, doi: 10.1103/PhysRevE.66.056307.
- [100] P. R. Di Palma, C. Huber, and P. Viotti, “A new lattice Boltzmann model for interface reactions between immiscible fluids,” *Adv. Water Resour.*, vol. 82, pp. 139–149, Aug. 2015, doi: 10.1016/j.advwatres.2015.05.001.
- [101] X. He and N. Li, “Lattice Boltzmann simulation of electrochemical systems,” *Comput. Phys. Commun.*, vol. 129, no. 1–3, pp. 158–166, Jul. 2000, doi: 10.1016/S0010-4655(00)00103-X.
- [102] E. Holzbecher, “Numerical Solutions for the Lévêque Problem of Boundary Layer Mass or Heat Flux,” *Proc. COMSOL Conf.*, no. 2, pp. 1–6, 2008, [Online]. Available: <https://www.researchgate.net/publication/235635576>.
- [103] X. He and N. Li, “Lattice Boltzmann simulation of electrochemical systems,” vol. 129, pp. 158–166, 2000.
- [104] M. A. Lévêque, “Les lois de la transmission de chaleur par convection,” *Ann. des Mines*, no. 13, p. 284, 1928.
- [105] G. Laudadio, N. J. W. Straathof, M. D. Lanting, B. Knoops, V. Hessel, and T. Noël, “An

- environmentally benign and selective electrochemical oxidation of sulfides and thiols in a continuous-flow microreactor,” *Green Chem.*, vol. 19, no. 17, pp. 4061–4066, 2017, doi: 10.1039/C7GC01973D.
- [106] J. G. I. Hellström and T. S. Lundström, “Flow through Porous Media at Moderate Reynolds Number,” *Int. Sci. Colloq. - Model. Mater. Process.*, no. June 2006, pp. 129–134, 2006.
- [107] J. González-García, P. Bonete, E. Expósito, V. Montiel, A. Aldaz, and R. Torregrosa-Maciá, “Characterization of a carbon felt electrode: structural and physical properties,” *J. Mater. Chem.*, vol. 9, no. 2, pp. 419–426, 1999, doi: 10.1039/a805823g.
- [108] J. V. Macpherson and P. R. Unwin, “Determination of the Diffusion Coefficient of Hydrogen in Aqueous Solution Using Single and Double Potential Step Chronoamperometry at a Disk Ultramicroelectrode,” *Anal. Chem.*, vol. 69, no. 11, pp. 2063–2069, Jun. 1997, doi: 10.1021/ac961211i.
- [109] R. Mills and J. W. Kennedy, “The Self-diffusion Coefficients of Iodide, Potassium and Rubidium Ions in Aqueous Solutions 1,” *J. Am. Chem. Soc.*, vol. 75, no. 22, pp. 5696–5701, Nov. 1953, doi: 10.1021/ja01118a063.
- [110] A. Asenbaum *et al.*, “Influence of various commercial water treatment processes on the electric conductivity of several drinking waters,” *J. Mol. Liq.*, vol. 160, no. 3, pp. 144–149, May 2011, doi: 10.1016/j.molliq.2011.03.007.
- [111] A. Celzard, J. F. Marêché, G. Furdin, and S. Puricelli, “Electrical conductivity of anisotropic expanded graphite-based monoliths,” *J. Phys. D. Appl. Phys.*, vol. 33, no. 23, pp. 3094–3101, Dec. 2000, doi: 10.1088/0022-3727/33/23/313.
- [112] T. R. Yu and G. L. Ji, *Electrochemical Methods in Soil and Water Research*. Elsevier,

- 1993.
- [113] S. Maljuric, W. Jud, C. O. Kappe, and D. Cantillo, “Translating batch electrochemistry to single-pass continuous flow conditions: an organic chemist’s guide,” *J. Flow Chem.*, vol. 10, no. 1, pp. 181–190, Mar. 2020, doi: 10.1007/s41981-019-00050-z.
- [114] D. Pletcher, R. A. Green, and R. C. D. Brown, “Flow Electrolysis Cells for the Synthetic Organic Chemistry Laboratory,” *Chem. Rev.*, vol. 118, no. 9, pp. 4573–4591, May 2018, doi: 10.1021/acs.chemrev.7b00360.
- [1] D. Marmer, “Water Conservation Equals Energy Conservation*,” *Energy Eng. J. Assoc. Energy Eng.*, vol. 115, no. 5, pp. 48–63, 2018, doi: 10.1080/01998595.2018.12027708.
- [2] H. Chang, *Water and Climate Change*. 2019.
- [3] A. Guamán and H. Yumisaca, *Estimated use of water in the United States*. 2015.
- [4] OECD, *OECD Environmental Outlook to 2050*. 2012.
- [5] U. Nations, “The United Nations World Water Development Report 2021: Valuing Water.” Paris, 2020.
- [6] D. M. Rockwood, “Water and energy,” *GeoJournal*, vol. 3, no. 5, pp. 461–470, 1979, doi: 10.1007/BF00455985.
- [7] WWAP, “Managing Water under Uncertainty and Risk (UNWWD Report 4, Vol 1),” 2012. [Online]. Available: <http://unesdoc.unesco.org/images/0021/002156/215644e.pdf>.
- [8] IEA, “Water Energy Nexus- Excerpt from the World Energy Outlook 2016,” *Iea*, p. 60, 2016, [Online]. Available: <https://www.iea.org/publications/freepublications/publication/WorldEnergyOutlook2016ExcerptWaterEnergyNexus.pdf>.

- [9] D. Mytton, “Data centre water consumption,” *npj Clean Water*, vol. 4, no. 1, 2021, doi: 10.1038/s41545-021-00101-w.
- [10] K. Pullerits *et al.*, “Impact of UV irradiation at full scale on bacterial communities in drinking water,” *npj Clean Water*, vol. 3, no. 1, pp. 1–10, 2020, doi: 10.1038/s41545-020-0057-7.
- [11] H. Canada, “Drinking Water Chlorination.” <https://www.canada.ca/en/health-canada/services/healthy-living/your-health/environment/drinking-water-chlorination.html>.
- [12] M. Sisti, G. F. Schiavano, M. De Santi, and G. Brandi, “Ultraviolet germicidal irradiation in tap water contaminated by *Aspergillus* spp,” *J. Prev. Med. Hyg.*, vol. 58, no. 4, pp. E315–E319, 2017, doi: 10.15167/2421-4248/jpmh2017.58.4.777.
- [13] P. E. Black, *Drinking Water and Health, Volume*, vol. 20, no. 6. 1984.
- [14] S. Hand and R. D. Cusick, “Electrochemical Disinfection in Water and Wastewater Treatment: Identifying Impacts of Water Quality and Operating Conditions on Performance,” *Environ. Sci. Technol.*, vol. 55, no. 6, pp. 3470–3482, Mar. 2021, doi: 10.1021/acs.est.0c06254.
- [15] I. Sirés, E. Brillas, M. A. Oturan, M. A. Rodrigo, and M. Panizza, “Electrochemical advanced oxidation processes: Today and tomorrow. A review,” *Environ. Sci. Pollut. Res.*, vol. 21, no. 14, pp. 8336–8367, 2014, doi: 10.1007/s11356-014-2783-1.
- [16] S. Hand and R. D. Cusick, “Electrochemical Disinfection in Water and Wastewater Treatment: Identifying Impacts of Water Quality and Operating Conditions on Performance,” *Environ. Sci. Technol.*, vol. 55, no. 6, pp. 3470–3482, 2021, doi: 10.1021/acs.est.0c06254.
- [17] K. Liu, C. Song, and A. Lei, “Recent advances in iodine mediated electrochemical

- oxidative cross-coupling,” *Org. Biomol. Chem.*, vol. 16, no. 14, pp. 2375–2387, 2018, doi: 10.1039/C8OB00063H.
- [18] N. E. Chadi, S. Merouani, O. Hamdaoui, M. Bouhelassa, and M. Ashokkumar, “Influence of mineral water constituents, organic matter and water matrices on the performance of the H₂O₂/IO₄⁻ -advanced oxidation process,” *Environ. Sci. Water Res. Technol.*, vol. 5, no. 11, pp. 1985–1992, 2019, doi: 10.1039/C9EW00329K.
- [19] B. P. Chaplin, “Critical review of electrochemical advanced oxidation processes for water treatment applications,” *Environ. Sci. Process. Impacts*, vol. 16, no. 6, pp. 1182–1203, 2014, doi: 10.1039/c3em00679d.
- [20] F. C. Moreira, R. A. R. Boaventura, E. Brillas, and V. J. P. Vilar, “Electrochemical advanced oxidation processes: A review on their application to synthetic and real wastewaters,” *Appl. Catal. B Environ.*, vol. 202, pp. 217–261, 2017, doi: 10.1016/j.apcatb.2016.08.037.
- [21] D. Ghernaout, N. Elboughdiri, S. Ghareba, and A. Salih, “Electrochemical Advanced Oxidation Processes (EAOPs) for Disinfecting Water—Fresh Perspectives,” *OALib*, vol. 07, no. 04, pp. 1–12, 2020, doi: 10.4236/oalib.1106257.
- [22] R. P. H. Huijbregts, A. I. P. M. de Kroon, and B. de Kruijff, “On the accessibility of phosphatidylglycerol to periodate in *Escherichia coli*,” *Mol. Membr. Biol.*, vol. 14, no. 1, pp. 35–38, Jan. 1997, doi: 10.3109/09687689709048168.
- [23] A. Moustafa *et al.*, “Operando Studies of Iodine Species in an Advanced Oxidative Water Treatment Reactor,” *ACS ES&T Water*, vol. 1, no. 11, pp. 2293–2304, Nov. 2021, doi: 10.1021/acsestwater.1c00149.
- [24] T. Kaiho, Ed., *Iodine Chemistry and Applications*. Hoboken, NJ: John Wiley & Sons, Inc,

- 2014.
- [25] M. Okochi *et al.*, “Disinfection of Microorganisms by Use of Electrochemically Regenerated Periodate,” *Appl. Environ. Microbiol.*, vol. 71, no. 10, pp. 6410–6413, Oct. 2005, doi: 10.1128/AEM.71.10.6410-6413.2005.
- [26] X.-Y. Zhang *et al.*, “Continuous exposure to non-lethal doses of sodium iodate induces retinal pigment epithelial cell dysfunction,” *Sci. Rep.*, vol. 6, no. 1, p. 37279, Dec. 2016, doi: 10.1038/srep37279.
- [27] A. J. Sioda RE, Cook GM, Keating KB, Williams JM, “Flow-Through Porous Electrodes,” *Chem. Eng. (New York)*, vol. 90, pp. 57–67, 1983.
- [28] M. E. Suss *et al.*, “Capacitive desalination with flow-through electrodes,” *Energy Environ. Sci.*, vol. 5, no. 11, p. 9511, 2012, doi: 10.1039/c2ee21498a.
- [29] S. Bebelis *et al.*, “Highlights during the development of electrochemical engineering,” *Chem. Eng. Res. Des.*, vol. 91, no. 10, pp. 1998–2020, Oct. 2013, doi: 10.1016/j.cherd.2013.08.029.
- [30] J. S. Newman and C. W. Tobias, “Theoretical Analysis of Current Distribution in Porous Electrodes,” *J. Electrochem. Soc.*, vol. 109, no. 12, p. 1183, 1962, doi: 10.1149/1.2425269.
- [31] J. D. Milshtein, K. M. Tenny, J. L. Barton, J. Drake, R. M. Darling, and F. R. Brushett, “Quantifying Mass Transfer Rates in Redox Flow Batteries,” *J. Electrochem. Soc.*, vol. 164, no. 11, pp. E3265–E3275, 2017, doi: 10.1149/2.0201711jes.
- [32] Y. Volkman, “Optimization of the effectiveness of a three-dimensional electrode with respect to its ohmic variables,” *Electrochim. Acta*, vol. 24, no. 11, pp. 1145–1149, Nov. 1979, doi: 10.1016/0013-4686(79)87062-0.

- [33] K. Kinoshita and S. C. Leach, "Mass-Transfer Study of Carbon Felt, Flow-Through Electrode," *J. Electrochem. Soc.*, vol. 129, no. 9, pp. 1993–1997, Sep. 1982, doi: 10.1149/1.2124338.
- [34] J. M. Bisang, K. Jüttner, and G. Kreysa, "Potential and current distribution in porous electrodes under charge-transfer kinetic control," *Electrochim. Acta*, vol. 39, no. 8–9, pp. 1297–1302, Jun. 1994, doi: 10.1016/0013-4686(94)E0050-A.
- [35] M. M. Saleh, "Mathematical modeling of gas evolving flow-through porous electrodes," *Electrochim. Acta*, vol. 45, no. 6, pp. 959–967, Dec. 1999, doi: 10.1016/S0013-4686(99)00296-0.
- [36] R. Carta, S. Palmas, A. M. Polcaro, and G. Tola, "Behaviour of a carbon felt flow by electrodes Part I: Mass transfer characteristics," *J. Appl. Electrochem.*, vol. 21, no. 9, pp. 793–798, Sep. 1991, doi: 10.1007/BF01402816.
- [37] J. A. Trainham and J. Newman, "A Flow-Through Porous Electrode Model: Application to Metal-Ion Removal from Dilute Streams," *J. Electrochem. Soc.*, vol. 124, no. 10, pp. 1528–1540, Oct. 1977, doi: 10.1149/1.2133106.
- [38] D. N. Bennion and J. Newman, "Electrochemical removal of copper ions from very dilute solutions," *J. Appl. Electrochem.*, vol. 2, no. 2, pp. 113–122, May 1972, doi: 10.1007/BF00609127.
- [39] D. Pilone and G. H. Kelsall, "Model of Multiple Metal Electrodeposition in Porous Electrodes," *J. Electrochem. Soc.*, vol. 153, no. 5, p. D85, 2006, doi: 10.1149/1.2178607.
- [40] R. C. Alkire, E. A. Grens, and C. W. Tobias, "A Theory for Porous Electrodes Undergoing Structural Change by Anodic Dissolution," *J. Electrochem. Soc.*, vol. 116, no. 10, p. 1328, 1969, doi: 10.1149/1.2411505.

- [41] A. M. Zaky and B. P. Chaplin, “Porous Substoichiometric TiO₂ Anodes as Reactive Electrochemical Membranes for Water Treatment,” *Environ. Sci. Technol.*, vol. 47, no. 12, pp. 6554–6563, Jun. 2013, doi: 10.1021/es401287e.
- [42] K. S. G. C. Oliveira, R. M. Farinos, A. B. Veroli, and L. A. M. Ruotolo, “Electrochemical incineration of glyphosate wastewater using three-dimensional electrode,” *Environ. Technol.*, vol. 42, no. 2, pp. 170–181, Jan. 2021, doi: 10.1080/09593330.2019.1625563.
- [43] B. N. Grgur, M. M. Gvozdenović, J. S. Stevanović, B. Z. Jugović, and L. T. Trišović, “Electrochemical oxidation of iodide in aqueous solution,” *Chem. Eng. J.*, vol. 124, no. 1–3, pp. 47–54, Nov. 2006, doi: 10.1016/j.cej.2006.08.028.
- [44] J. Newman and N. P. Balsara, *Electrochemical Systems*. Wiley, 2021.
- [45] A. Bard and L. Faulkner, *Electrochemical Methods: Fundamentals and Applications*, vol. 12. 2000.
- [46] V. Levich and S. Rice, “Physicochemical Hydrodynamics,” *Phys. Today*, vol. 16, p. 75, May 1963, doi: 10.1063/1.3050934.
- [47] R. Probstein, *Physicochemical Hydrodynamics*. 2003.
- [48] K. J. Vetter., “Electrochemical kinetics: theoretical and experimental aspects,” *Glycobiology*, vol. 2, no. 3. pp. 251–255, 1992, [Online]. Available: <https://academic.oup.com/glycob/article-lookup/doi/10.1093/glycob/2.3.251>.
- [49] J. M. Pingarrón *et al.*, “Terminology of electrochemical methods of analysis (IUPAC Recommendations 2019),” *Pure Appl. Chem.*, vol. 92, no. 4, pp. 641–694, 2020, doi: 10.1515/pac-2018-0109.
- [50] X. Jin, A. Ku, A. Verma, B. Ohara, K. Huang, and S. Singh, “The Performance of Syngas-Fueled SOFCs Predicted by a Reduced Order Model (ROM): Temperature and Fuel

- Composition Effects,” *J. Electrochem. Soc.*, vol. 165, no. 10, pp. F786–F798, 2018, doi: 10.1149/2.0511810jes.
- [51] E. J. F. Dickinson and A. J. Wain, “The Butler-Volmer equation in electrochemical theory: Origins, value, and practical application,” *J. Electroanal. Chem.*, vol. 872, p. 114145, 2020, doi: 10.1016/j.jelechem.2020.114145.
- [52] R. Guidelli *et al.*, “Defining the transfer coefficient in electrochemistry: An assessment (IUPAC Technical Report),” *Pure Appl. Chem.*, vol. 86, no. 2, pp. 245–258, 2014, doi: 10.1515/pac-2014-5026.
- [53] J. Price, “Lagrangian and eulerian representations of fluid flow: Kinematics and the equations of motion,” 2006.
- [54] S. Succi, *The Lattice Boltzmann Equation for Fluid Dynamics and Beyond*. Oxford Science, 2001.
- [55] M. C. Sukop and D. T. Thorne, *Lattice Boltzmann Modeling*. Berlin, Heidelberg: Springer Berlin Heidelberg, 2006.
- [56] T. Krüger, H. Kusumaatmaja, A. Kuzmin, O. Shardt, G. Silva, and E. M. Viggien, *The Lattice Boltzmann Method*. Cham: Springer International Publishing, 2017.
- [57] D. A. Wolf-Gladrow, *Lattice Gas Cellular Automata and Lattice Boltzmann Models*, vol. 1725. Berlin, Heidelberg: Springer Berlin Heidelberg, 2000.
- [58] A. A. Mohamad, *Lattice Boltzmann Method*. London: Springer London, 2011.
- [59] Y. Feng, M. Tayyab, and P. Boivin, “A Lattice-Boltzmann model for low-Mach reactive flows,” *Combust. Flame*, vol. 196, pp. 249–254, 2018, doi: 10.1016/j.combustflame.2018.06.027.
- [60] H. E. Van den Akker, “Lattice Boltzmann simulations for multi-scale chemical

- engineering,” *Curr. Opin. Chem. Eng.*, vol. 21, pp. 67–75, 2018, doi: 10.1016/j.coche.2018.03.003.
- [61] G. T. Zachariah, D. Panda, and V. K. Surasani, “Lattice Boltzmann simulations for invasion patterns during drying of capillary porous media,” *Chem. Eng. Sci.*, vol. 196, pp. 310–323, 2019, doi: 10.1016/j.ces.2018.11.003.
- [62] A. Xu, W. Shyy, and T. Zhao, “Lattice Boltzmann modeling of transport phenomena in fuel cells and flow batteries,” *Acta Mech. Sin. Xuebao*, vol. 33, no. 3, pp. 555–574, 2017, doi: 10.1007/s10409-017-0667-6.
- [63] H. Safari, M. H. Rahimian, and M. Krafczyk, “Extended lattice Boltzmann method for numerical simulation of thermal phase change in two-phase fluid flow,” *Phys. Rev. E - Stat. Nonlinear, Soft Matter Phys.*, vol. 88, no. 1, pp. 1–12, 2013, doi: 10.1103/PhysRevE.88.013304.
- [64] J. Horbach and D. Frenkel, “Lattice-Boltzmann method for the simulation of transport phenomena in charged colloids,” *Phys. Rev. E - Stat. Physics, Plasmas, Fluids, Relat. Interdiscip. Top.*, vol. 64, no. 6, p. 8, 2001, doi: 10.1103/PhysRevE.64.061507.
- [65] P. J. Dellar, “Bulk and shear viscosities in lattice Boltzmann equations,” *Phys. Rev. E - Stat. Physics, Plasmas, Fluids, Relat. Interdiscip. Top.*, vol. 64, no. 3, p. 11, 2001, doi: 10.1103/PhysRevE.64.031203.
- [66] S. Javed, A. Sohail, K. Maqbool, S. I. Butt, and Q. A. Chaudhry, “The Lattice Boltzmann method and computational analysis of bone dynamics-I,” *Complex Adapt. Syst. Model.*, vol. 5, no. 1, pp. 1–14, 2017, doi: 10.1186/s40294-017-0051-1.
- [67] C. Cercignani, *The Boltzmann Equation and Its Applications*, vol. 67. New York, NY: Springer New York, 1988.

- [68] X. B. Nie, X. Shan, and H. Chen, “Galilean invariance of lattice Boltzmann models,” *EPL (Europhysics Lett.)*, vol. 81, no. 3, p. 34005, Feb. 2008, doi: 10.1209/0295-5075/81/34005.
- [69] A. S. Joshi, K. N. Grew, A. A. Peracchio, and W. K. S. Chiu, “Lattice Boltzmann modeling of 2D gas transport in a solid oxide fuel cell anode,” *J. Power Sources*, vol. 164, no. 2, pp. 631–638, Feb. 2007, doi: 10.1016/j.jpowsour.2006.10.101.
- [70] J. Bear, *Dynamics of Fluids in Porous Media*. New York: American Elsevier Pub. Co, 1972.
- [71] M. A. Mujeebu, M. Z. Abdullah, M. Z. A. Bakar, A. A. Mohamad, R. M. N. Muhad, and M. K. Abdullah, “Combustion in porous media and its applications – A comprehensive survey,” *J. Environ. Manage.*, vol. 90, no. 8, pp. 2287–2312, Jun. 2009, doi: 10.1016/j.jenvman.2008.10.009.
- [72] J. Latt, “Hydrodynamic limit of lattice Boltzmann equations,” Geneve, 2007.
- [73] X. Nie and N. S. Martys, “Breakdown of Chapman-Enskog expansion and the anisotropic effect for lattice-Boltzmann models of porous flow,” *Phys. Fluids*, vol. 19, no. 1, pp. 8–12, 2007, doi: 10.1063/1.2432153.
- [74] A. Hu, L. Li, and R. Uddin, “Force method in a pseudo-potential lattice Boltzmann model,” vol. 294, pp. 78–89, 2015.
- [75] S. A. Bawazeer, S. S. Baakeem, and A. A. Mohamad, “A Critical Review of Forcing Schemes in Lattice Boltzmann Method: 1993–2019,” *Arch. Comput. Methods Eng.*, no. 0123456789, 2021, doi: 10.1007/s11831-021-09535-4.
- [76] D. Yu, R. Mei, L.-S. Luo, and W. Shyy, “Viscous flow computations with the method of lattice Boltzmann equation,” *Prog. Aerosp. Sci.*, vol. 39, no. 5, pp. 329–367, Jul. 2003, doi: 10.1016/S0376-0421(03)00003-4.

- [77] I. Ginzbourg and P. M. Adler, “Boundary flow condition analysis for the three-dimensional lattice Boltzmann model,” *J. Phys. II*, vol. 4, no. 2, pp. 191–214, Feb. 1994, doi: 10.1051/jp2:1994123.
- [78] H. Liu, J. G. Zhou, and R. Burrows, “Inlet and outlet boundary conditions for the Lattice-Boltzmann modelling of shallow water flows,” *Prog. Comput. Fluid Dyn. An Int. J.*, vol. 12, no. 1, p. 11, 2012, doi: 10.1504/PCFD.2012.044850.
- [79] J. D. Sterling and S. Chen, “Stability Analysis of Lattice Boltzmann Methods,” *J. Comput. Phys.*, vol. 123, no. 1, pp. 196–206, Jan. 1996, doi: 10.1006/jcph.1996.0016.
- [80] Q. Zou and X. He, “On pressure and velocity boundary conditions for the lattice Boltzmann BGK model,” *Phys. Fluids*, vol. 9, no. 6, pp. 1591–1598, Jun. 1997, doi: 10.1063/1.869307.
- [81] A. Mussa, P. Asinari, and L.-S. Luo, “Lattice Boltzmann simulations of 2D laminar flows past two tandem cylinders,” *J. Comput. Phys.*, vol. 228, no. 4, pp. 983–999, Mar. 2009, doi: 10.1016/j.jcp.2008.10.010.
- [82] S. Succi, “Applied Lattice Boltzmann Method for Transport Phenomena, Momentum, Heat and Mass Transfer. A. A. Mohamad Sure Printing, Calgary, AB April 2007,” *Can. J. Chem. Eng.*, vol. 85, no. 6, pp. 946–947, May 2008, doi: 10.1002/cjce.5450850617.
- [83] A. A. Alamyane and A. A. Mohamad, “Simulation of forced convection in a channel with extended surfaces by the lattice Boltzmann method,” *Comput. Math. with Appl.*, vol. 59, no. 7, pp. 2421–2430, Apr. 2010, doi: 10.1016/j.camwa.2009.08.070.
- [84] R. J. MILLINGTON and J. P. QUIRK, “Formation Factor and Permeability Equations,” *Nature*, vol. 202, no. 4928, pp. 143–145, Apr. 1964, doi: 10.1038/202143a0.
- [85] R. C. Alkire, D. M. Kolb, L. A. Kibler, and J. Lipkowski, Eds., *Electrocatalysis*, vol. 14.

- Wiley, 2013.
- [86] S. S. Baakeem, S. A. Bawazeer, and A. A. Mohamad, “A novel approach of unit conversion in the lattice boltzmann method,” *Appl. Sci.*, vol. 11, no. 14, 2021, doi: 10.3390/app11146386.
- [87] J. Latt, “Choice of units in lattice Boltzmann simulations,” 2008.
- [88] E. Chiavazzo, I. V Karlin, A. N. Gorban, and K. Boulouchos, “Combustion simulation via lattice Boltzmann and reduced chemical kinetics,” *J. Stat. Mech. Theory Exp.*, vol. 2009, no. 06, p. P06013, Jun. 2009, doi: 10.1088/1742-5468/2009/06/P06013.
- [89] S. H. Ashworth, *A student’s guide to dimensional analysis*, vol. 59, no. 4. Cambridge University Press, 2018.
- [90] O. R. Spies, “Dimensional analysis and theory of models,” *J. Franklin Inst.*, vol. 253, no. 1, p. 84, Jan. 1952, doi: 10.1016/0016-0032(52)90438-9.
- [91] P. . Bridgman, *Dimensional analysis*, 2nd ed. New Heaven: Yale University Press, 1931.
- [92] A. Ghassemi and A. Pak, “Pore scale study of permeability and tortuosity for flow through particulate media using Lattice Boltzmann method,” *Int. J. Numer. Anal. Methods Geomech.*, vol. 35, no. 8, pp. 886–901, Jun. 2011, doi: 10.1002/nag.932.
- [93] Q. Kang, P. C. Lichtner, and D. Zhang, “An improved lattice Boltzmann model for multicomponent reactive transport in porous media at the pore scale,” *Water Resour. Res.*, vol. 43, no. 12, pp. 1–12, Dec. 2007, doi: 10.1029/2006WR005551.
- [94] L. Hao and P. Cheng, “Pore-scale simulations on relative permeabilities of porous media by lattice Boltzmann method,” *Int. J. Heat Mass Transf.*, vol. 53, no. 9–10, pp. 1908–1913, Apr. 2010, doi: 10.1016/j.ijheatmasstransfer.2009.12.066.
- [95] E. Fattahi, C. Waluga, B. Wohlmuth, U. Rde, M. Manhart, and R. Helmig, “Lattice

- Boltzmann methods in porous media simulations: From laminar to turbulent flow,” *Comput. Fluids*, vol. 140, pp. 247–259, Nov. 2016, doi: 10.1016/j.compfluid.2016.10.007.
- [96] M. E. Kutay, A. H. Aydilek, and E. Masad, “Laboratory validation of lattice Boltzmann method for modeling pore-scale flow in granular materials,” *Comput. Geotech.*, vol. 33, no. 8, pp. 381–395, Dec. 2006, doi: 10.1016/j.compgeo.2006.08.002.
- [97] H. Yoon, Q. Kang, and A. J. Valocchi, “Lattice Boltzmann-Based Approaches for Pore-Scale Reactive Transport,” *Rev. Mineral. Geochemistry*, vol. 80, no. 1, pp. 393–431, 2015, doi: 10.2138/rmg.2015.80.12.
- [98] H. Li, H. J. H. Clercx, and F. Toschi, “LBM Investigations on a Chain Reaction in a Reactive Electro-Kinetic Flow in Porous Material,” *J. Electrochem. Soc.*, vol. 168, no. 8, p. 083502, Aug. 2021, doi: 10.1149/1945-7111/ac1b4a.
- [99] Q. Kang, D. Zhang, and S. Chen, “Unified lattice Boltzmann method for flow in multiscale porous media,” *Phys. Rev. E*, vol. 66, no. 5, p. 056307, Nov. 2002, doi: 10.1103/PhysRevE.66.056307.
- [100] P. R. Di Palma, C. Huber, and P. Viotti, “A new lattice Boltzmann model for interface reactions between immiscible fluids,” *Adv. Water Resour.*, vol. 82, pp. 139–149, Aug. 2015, doi: 10.1016/j.advwatres.2015.05.001.
- [101] X. He and N. Li, “Lattice Boltzmann simulation of electrochemical systems,” *Comput. Phys. Commun.*, vol. 129, no. 1–3, pp. 158–166, Jul. 2000, doi: 10.1016/S0010-4655(00)00103-X.
- [102] E. Holzbecher, “Numerical Solutions for the Lévêque Problem of Boundary Layer Mass or Heat Flux,” *Proc. COMSOL Conf.*, no. 2, pp. 1–6, 2008, [Online]. Available: <https://www.researchgate.net/publication/235635576>.

- [103] X. He and N. Li, "Lattice Boltzmann simulation of electrochemical systems," vol. 129, pp. 158–166, 2000.
- [104] M. A. Lévêque, "Les lois de la transmission de chaleur par convection," *Ann. des Mines*, no. 13, p. 284, 1928.
- [105] G. Laudadio, N. J. W. Straathof, M. D. Lanting, B. Knoops, V. Hessel, and T. Noël, "An environmentally benign and selective electrochemical oxidation of sulfides and thiols in a continuous-flow microreactor," *Green Chem.*, vol. 19, no. 17, pp. 4061–4066, 2017, doi: 10.1039/C7GC01973D.
- [106] J. G. I. Hellström and T. S. Lundström, "Flow through Porous Media at Moderate Reynolds Number," *Int. Sci. Colloq. - Model. Mater. Process.*, no. June 2006, pp. 129–134, 2006.
- [107] J. González-García, P. Bonete, E. Expósito, V. Montiel, A. Aldaz, and R. Torregrosa-Maciá, "Characterization of a carbon felt electrode: structural and physical properties," *J. Mater. Chem.*, vol. 9, no. 2, pp. 419–426, 1999, doi: 10.1039/a805823g.
- [108] J. V. Macpherson and P. R. Unwin, "Determination of the Diffusion Coefficient of Hydrogen in Aqueous Solution Using Single and Double Potential Step Chronoamperometry at a Disk Ultramicroelectrode," *Anal. Chem.*, vol. 69, no. 11, pp. 2063–2069, Jun. 1997, doi: 10.1021/ac961211i.
- [109] R. Mills and J. W. Kennedy, "The Self-diffusion Coefficients of Iodide, Potassium and Rubidium Ions in Aqueous Solutions 1," *J. Am. Chem. Soc.*, vol. 75, no. 22, pp. 5696–5701, Nov. 1953, doi: 10.1021/ja01118a063.
- [110] A. Asenbaum *et al.*, "Influence of various commercial water treatment processes on the electric conductivity of several drinking waters," *J. Mol. Liq.*, vol. 160, no. 3, pp. 144–

- 149, May 2011, doi: 10.1016/j.molliq.2011.03.007.
- [111] A. Celzard, J. F. Marêché, G. Furdin, and S. Puricelli, “Electrical conductivity of anisotropic expanded graphite-based monoliths,” *J. Phys. D. Appl. Phys.*, vol. 33, no. 23, pp. 3094–3101, Dec. 2000, doi: 10.1088/0022-3727/33/23/313.
- [112] T. R. Yu and G. L. Ji, *Electrochemical Methods in Soil and Water Research*. Elsevier, 1993.
- [113] S. Maljuric, W. Jud, C. O. Kappe, and D. Cantillo, “Translating batch electrochemistry to single-pass continuous flow conditions: an organic chemist’s guide,” *J. Flow Chem.*, vol. 10, no. 1, pp. 181–190, Mar. 2020, doi: 10.1007/s41981-019-00050-z.
- [114] D. Pletcher, R. A. Green, and R. C. D. Brown, “Flow Electrolysis Cells for the Synthetic Organic Chemistry Laboratory,” *Chem. Rev.*, vol. 118, no. 9, pp. 4573–4591, May 2018, doi: 10.1021/acs.chemrev.7b00360.

Appendix A

$$\partial_t f + \mathbf{u} \cdot \partial_x f = \Gamma(f, f) \quad (\text{A.1})$$

$$\Gamma(f, f) = \int d^3 \mathbf{v}_1 \int d\Omega \sigma(\Omega) |\mathbf{v} - \mathbf{v}_1| (f(\mathbf{v}') f(\mathbf{v}_1') - f(\mathbf{v}) f(\mathbf{v}_1)) \quad (4)$$

$$\int \Gamma(f, f) \psi_k(\mathbf{v}) d^3 \mathbf{v} = 0 \quad (5.3)$$

$$\psi_k(\mathbf{v}) \quad (k = 0, 1, 2, 3, 4)$$

$$\psi_0 = 1, (\psi_1, \psi_2, \psi_3) = \mathbf{v} \quad (\text{A.4})$$

$$\psi_4 = \mathbf{v}^2$$

$$\phi(\mathbf{v}) = a + \mathbf{b} \cdot \mathbf{v} + c(\mathbf{v} \cdot \mathbf{v}) \quad (\text{A.5})$$

$$f(\mathbf{v}) = \exp(a + \mathbf{b} \cdot \mathbf{v} + c\mathbf{v}^2) \quad (\text{A.6})$$

$$H(t) = \int f(\mathbf{x}, \mathbf{v}, t) \ln f(\mathbf{x}, \mathbf{v}, t) d^3 \mathbf{v} d^3 \mathbf{x} \quad (\text{A.7})$$